KU Leuven
Biomedical Sciences Group
Faculty of Medicine
Department of Imaging and Pathology

KU LEUVEN

DOCTORAL SCHOOL
BIOMEDICAL SCIENCES

Novel imaging-derived morphological and functional biomarkers of lung disease in mouse models

Kaat DEKOSTER

Supervisor: Prof. Dr. Greetje Vande Velde
Co-supervisor: Prof. Dr. Jeroen Vanoirbeek

Jury members: Prof. Dr. Wim Janssens
                        Prof. Dr. Christine Breynaert
                        Prof. Dr. François Huaux
                        Dr. Juan-Antonio Cámara Serrano

Dissertation presented in partial fulfilment of the requirements for the degree of Doctor in Biomedical Sciences.

Leuven, 2022

Table of contents

List of abbreviations

μCT	Micro-computed tomography
AEC	Alveolar epithelial cell
ATII	Alveolar epithelial cell type 2
BALF	Bronchoalveolar lavage fluid
BLI	Bioluminescence imaging
CI	Confidence interval
CNR	Contrast-to-noise ration
CT	Computed tomography
CTD	Connective tissue disease
CTGF	Connective tissue growth factor
CXCL12	CXC Chemokine ligand 12
ECM	Extracellular matrix
EMT	Epithelial mesenchymal transition
FEV0.1	Forced expiratory volume in 0.1 second
FGF	Fibroblast growth factor
FI	Fluorescence imaging
FVC	Forced vital capacity
G	Tissue damping
Gy	Grays
H	Tissue elasticity
H&E	Haematoxyil and Eosin
HP	Hypersensitivity pneumonitis
HRCT	High resolution computed tomohraphy
HU	Hounsfield unit
IC	Inspiratory capacity
IL	Interleukin
ILD	Interstitial lung disease
IPF	Idiopathic pulmonary fibrosis
MIP-1α	Macrophage inflammatory protein 1α
MMP	Matrix metalloproteinase
MRI	Magnetic resonance imaging
NE	Neutrophil elastase
OH-proline	Hydroxyproline

PDGF	Platelet derived growth factor
PEF	Peak expiratory flow
PET	Positron emission tomography
PV	Pressure-volume
RA	Rheumatoid arthritis
RL	Radioluminescence
Rn	Airway resistance
ROS	Reactive oxygen species
SD	Standard deviation
SNR	Signal-to-noise ratio
SpD	Protein surfactant D
SPECT	Single photon emission computed tomography
SSc	Systemic sclerosis
SSC	Squamous cell carcinoma
TGF-β	Transforming growth factor β
TIMP	Tissue inhibitor of metalloproteinases
TLD	Thermoluminescent detector
UIP	Usual interstitial pneumonia
UTE	Ultrashort echo time
VEGF	Vascular endothelial growth factor
VOI	Volume of interest

Chapter 1

General introduction

Section 3.1.4 and 3.2.1 partly based on

1. Pulmonary fibrosis

1.1. The lungs, an essential organ

Breathing is a crucial process for all humans. We inhale and exhale air through our lungs, the primary organ of the respiratory system. The respiratory tract includes from top to bottom: the trachea that receives air from the mouth and nose, branches of bronchi and bronchioles that further conduct the air, the alveolar ducts and at last alveolar sacs containing the alveoli, where the main function of the lungs occurs: gas exchange [1] (Figure 1). During this process, oxygen diffuses from the alveoli into the blood stream and carbon dioxide diffuses from the blood into the alveoli to leave the lungs via exhalation. The blood further transports the oxygen to the rest of the body, which is essential for cells in the human body to produce energy.
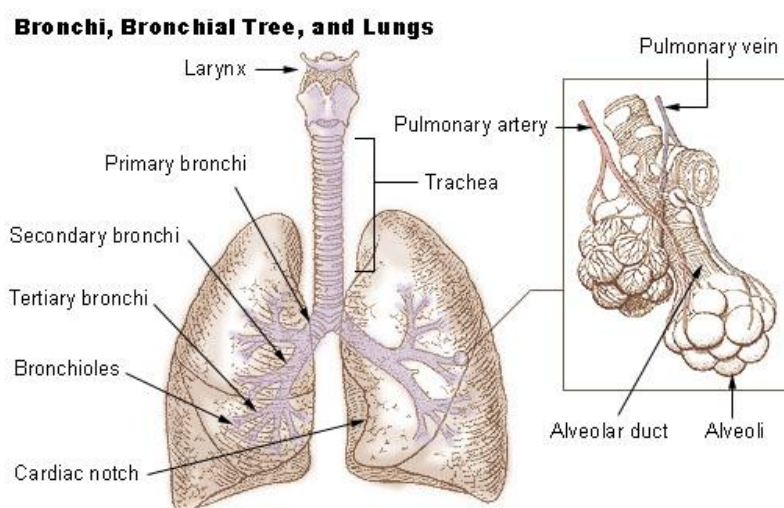
Figure 1: overview of the respiratory tract [2].

When a lung disease affects the lungs, this often results in breathing problems preventing the body from receiving enough vital oxygen. Interstitial lung diseases (ILDs) is an umbrella term for a large group of restrictive lung diseases where progressive and irreversible destruction of the lung architecture results in disrupted gas exchange, respiratory failure and eventually leading to increased morbidity and mortality [3,4]. Since often symptoms are very unspecific to the disease, diagnosis occurs in very advanced stages of the disease [5]. Despite many potentially anti-fibrotic compounds used in preclinical studies, there is still no effective curative treatment available. As such, ILDs remain a life-threatening condition in need of further research and therapeutic discoveries [6,7]. In the following section, we introduce ILDs and further expand on pulmonary fibrosis.

1.2. Classification of ILD and pulmonary fibrosis

ILDs are a heterogeneous group of lung disorders characterized by the presence of cellular proliferation, cellular infiltration and/or fibrosis of the lung parenchyma, not associated with infection or neoplasia [4]. Pulmonary fibrosis in particular is the replacement of healthy tissue by an excessive deposition of extracellular matrix, an altered alveolar architecture and often a predominant phenotype of ILDs. The frequently progressive and irreversible destruction of the lung architecture results in a decreased lung compliance, disrupted gas exchange and respiratory failure. In the end, to prevent early mortality, patients are in need of an organ transplantation [3,4]. Respiratory symptoms of ILDs and pulmonary fibrosis include unexplained shortness of breath during exercise (exertional dyspnea), chronic dry cough and shortness of breath.

Diagnosis of ILD is based on a combination of clinical history, pulmonary function testing, serological testing, bronchoalveolar lavage (BAL) analysis, histopathology and high-resolution computed tomography (HRCT), where HRCT is an important aspect of this diagnosis and often used for the disease follow-up [8].

ILDs express varying levels of chronic inflammation and pulmonary fibrosis and can be further classified depending on the clinical, radiological and histopathological features [9]. An overview of the different (forms of) ILD is shown in Table 1.

Table 1: classification of interstitial lung diseases [9]

Known causes	Drugs
	Connective tissue diseases
	Environmental exposures
	Genetics
Idiopathic interstitial pneumonias	Idiopathic pulmonary fibrosis
	Non-specific interstitial pneumonia
	Respiratory bronchiolitis interstitial lung disease
	Acute interstitial pneumonia
	Desquamative interstitial pneumonia
	Cryptogenic organising pneumonia
	Lymphocytic interstitial pneumonia
Granulomatous diseases	Sarcoidosis
	Fungal infection
	Mycobacterial infection
	Diseases associated with environmental exposures (e.g. chronic beryllium disease, hypersensitivity pneumonitis)
Other forms	Pulmonary alveolar proteinosis
	Langerhans' cell histiocytosis
	Eosinophilic pneumonia
	Lymphangioleiomyomatosis
	Pulmonary capillaritis

ILDs can manifest primarily either as an inflammatory disease with little or no fibrosis, as a fibrotic disease with no inflammatory features or as a combination of both (Figure 2) [10]. Pulmonary fibrosis is often a common feature of ILD and can have different aetiologies. Commonly, subacute and chronic forms of ILDs are treated by physicians specialized in general medicine. Different forms of ILD include idiopathic pulmonary fibrosis, connective-tissue disease related ILD, hypersensitivity pneumonitis, occupation related-ILD and medication-induced ILD, which are briefly discussed in the following section.
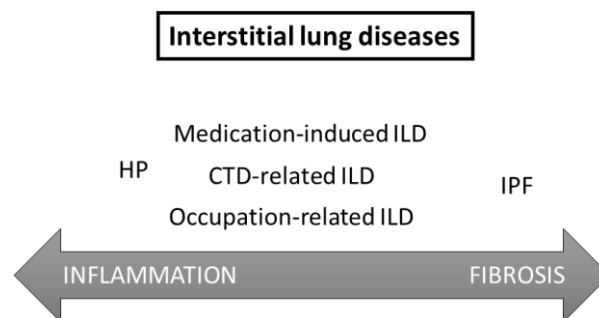
Figure 2: overview of ILD and pulmonary fibrosis.
Depending on the type, a varying degree of inflammation and pulmonary fibrosis can be present. This overview includes five most common forms of ILD: IPF (idiopathic pulmonary fibrosis), HP (hypersensitivity pneumonitis), occupation-related ILD, medication-induced ILD and CTD-related ILD (connective tissue disease related ILD).

1.2.1. Idiopathic pulmonary fibrosis

Idiopathic pulmonary fibrosis (IPF) is a chronic, progressive form of ILD with unknown aetiology and poor survival rate. IPF is one of the most common forms of ILDs with an incidence of 3 to 9 cases per 100.000 person/year and therefore considered as one of the most important ILDs [11]. It mostly occurs in middle to older aged men (60-70 years). Patients have a median survival time of 2-4 years after diagnosis [12-14]. Cigarette smoking, environmental exposure (e.g. metal dusts, wood dusts, farming, stone cutting, exposure to livestock,…), microbial agents and gastroesophageal reflux are considered important risk factors for the development of IPF [12].

Diagnosis of IPF is based on physical examination, pulmonary function testing, serological testing, clinical history and a usual interstitial pneumonia (UIP) pattern found on high-resolution chest CT and histopathology [8]. More specifically, the diagnosis of IPF is based on the exclusion of every other cause, since the UIP pattern is often observed in ILDs associated with occupation and environmental exposure, CTD and drug toxicity [3,5]. This deterministic approach following exclusion criteria is particularly difficult since patients often have an extended history of medication intake and environmental exposures. Currently, two drugs show to improve quality of life and life expectancy for

IPF: Nintedanib and Pirfenidone. Both drugs were able to stop the decline in forced vital capacity (FVC) by approximately 50% in placebo-controlled trials [15,16].

1.2.2. Connective tissue disease-related ILD

Connective tissue diseases (CTDs) are systemic autoimmune diseases with unique and distinguishing features. CTDs include rheumatoid arthritis (RA); systemic lupus erythematosus; systemic sclerosis (scleroderma) (Ssc); primary Sjögren's syndrome; polymyositis, dermatomyositis and antisynthetase syndrome; mixed CTD; and undifferentiated CTD [9]. They are characterized by an underlying mechanism caused by circulating autoantibodies and various forms of autoimmune related organ damage, frequently the lungs [17,18]. Respiratory complications are often associated with CTDs and every compartment of the lungs is at risk resulting in significant morbidity and mortality [9]. ILD is associated with all CTDs, though more present in rheumatoid arthritis, systemic sclerosis and polymyositis/dermatomyositis (Table 2).

Table 2: Common pulmonary manifestations of CTDs [9]

	ILD	Airways	Pleural	Vascular	DAH
Systemic sclerosis	+++	-	-	+++	-
Rheumatoid arthritis	++	++	++	+	-
Primary Sjögren's syndrome	++	++	+	+	-
Mixed CTD	++	+	+	++	-
Polymyositis/dermatomyositis	+++	-	-	+	-
Systemic lupus erythematosus	+	+	+++	+	++

(- = no prevalence; + = low prevalence; ++ = medium prevalence; +++ = high prevalence; DAH = diffuse alveolar haemorrhage; CTD = connective tissue disease; ILD = interstitial lung disease)

Systemic sclerosis has a yearly incidence of 10-50 cases per 1 million people and up to 30-40% of patients will develop ILD. ILD is the leading cause of morbidity and mortality in SSc and SSc-ILD has a 10-year mortality of up to 40% [19]. RA-ILD has a yearly incidence rate of 4.1 per 1000 RA patients and patients have a median survival rate of 3.5 years after diagnosis [20]. Risk factors associated with developing ILD in RA include age, male sex, high RA disease activity and occupational exposure to e.g. silica [21].

The histological and radiographic representation of ILD associated with CTD often mimics the patterns seen in idiopathic interstitial pneumonia, e.g. nonspecific interstitial pneumonia, usual interstitial pneumonia, organizing pneumonia, diffuse alveolar damage and lymphocytic interstitial pneumonia [17]. Depending on the type of CTD-related ILD, corticosteroids and immunosuppressive therapeutics are used for management, although not all patients need therapy [9].

1.2.3. Hypersensitivity pneumonitis

Hypersensitivity pneumonitis (HP) is the third most common diagnosis of ILD. HP is caused by an immunological reaction on inhalation of environmental antigens, e.g. avian proteins, moulds or

farming. It is an allergic alveolitis and diagnosis is of high importance since elimination of exposure to the antigen can give substantial benefit to the patient [10]. Management of HP thus includes removal of the antigen and the use of corticosteroids [22]. The histopathological image of HP is a chronic inflammation located around the small airways and poorly formed granulomas are present [23].

1.2.4. ILD induced by occupational exposure

Occupational exposure to coal, silica, asbestos, beryllium, cobalt, tungsten, aluminium, and other chemicals have all been associated with ILDs over the past few decades [10]. The two most common forms of occupation-related ILD are silicosis (after silica exposure e.g. with mining and sandblasting) and asbestosis (after asbestos exposure) [24]. More commonly known, is the relationship between asbestosis and lung cancer. In general, it is believed that the presence of asbestosis is linked with increasing chances on lung cancer associated with asbestos exposure [25]. As in HP, recognition and identification of occupation-related ILD is based on a detailed occupational history of the patient and imaging of the lungs.

Prevention is the most important aspect of management of occupation-related morbidity by eliminating or minimizing the exposure to the above-mentioned substitutes [10]. Unfortunately, in case of chronic exposure, fibrotic lung disease can manifest and there are only limited available therapeutic options, e.g. corticosteroids that have limited efficacy for chronic beryllium disease.

1.2.5. Medication-induced ILD

Different drugs have also been identified over the past years that have ILD and pulmonary fibrosis as a secondary unwanted side effect. Examples are cardiovascular medications (e.g., amiodarone), antimicrobials (e.g., nitrofurantoin), biologics (e.g., tumor necrosis factor-inhibitors), neurologic medications (e.g., bromocriptine), herbal medications, and numerous anti-neoplastic medications (bleomycin) [10]. Moreover, as a secondary effect to anti-neoplastic therapy, radiation of the chest can also induce pulmonary fibrosis. Some patients might benefit from corticosteroids therapy.

1.3. Pathogenesis of pulmonary fibrosis

1.3.1. Fibrotic process

Pulmonary fibrosis is the replacement of healthy tissue by an excessive deposition of extracellular matrix and an altered alveolar architecture. Both short and long-term repeated injury of the lung can result in lung fibrosis. This fibrosis can be temporarily present and partly reversible or can manifest as chronic, progressive fibrosis ultimately resulting in increased mortality and death. In general, it is believed that repeated injury of the lungs together with a genetic predisposition can result in pulmonary fibrosis [26]. In certain ILDs, persistent lung injury due to drug toxicity or radiation, inhaled

agents such as asbestos and silica can induce lung fibrosis. Different factors are believed to play a role in the induction of pulmonary fibrosis: genetic predisposition, exposure to environmental particles, drug intake, gastro-oesophageal reflux, viruses or a combination of different initiating factors.
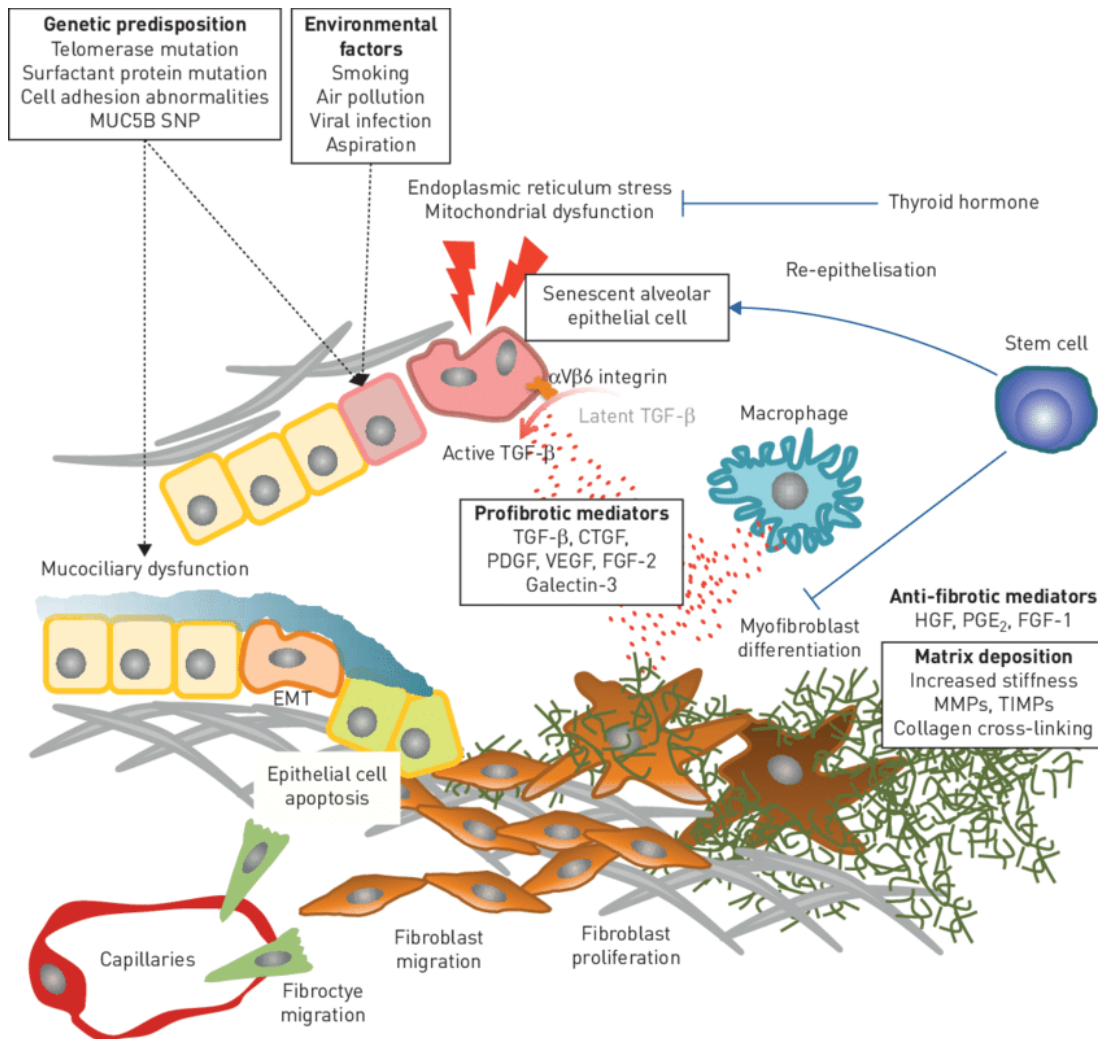
Figure 3: possible pathobiology of idiopathic pulmonary fibrosis.
Both genetic predisposition and recurrent epithelial cell injury are believed to play a role in the onset of pulmonary fibrosis. They lead to epithelial as well as endothelial damage, vascular leakage, epithelial mesenchymal transition and fibrin clot formation resulting in the release of profibrogenic mediators. In the next stage, the abnormal repair process induces fibrocytes/fibroblast migration and infiltration and ultimately differentiation in profibrotic macrophages/myofibroblast. This leads to abnormal re-epithelialisation and formation of extracellular matrix (ECM). At last, pulmonary fibrosis is characterized by an excessive deposition of extracellular matrix components leading to a disrupted lung architecture and respiratory failure. SNP=single nucleotide polymorphism, TGF=transforming growth factor, HGT=hepatocyte growth factor, PGE2=prostaglandin E2, FGF-1=fibroblast growth factor-1, FGF-2=fibroblast growth factor-2, CTGF=connective tissue growth factor, PDGF=platelet-derived growth factor, VEGF=vascular endothelial growth factor, MMP=matrix metalloproteinases, TIMP=tissue inhibitors of metalloproteinase, EMT=epithelial mesenchymal transition (figure and legend adapted from Yanagihara *et al.* (2019))[27]

Repeated lung injury is believed to cause epithelial and endothelial damage, leading to vascular leakage and triggering a repair process resulting in fibrin clot formation [26]. Dysfunctional and damaged alveolar epithelial cells (AECs) promote migration of monocytes, fibrocytes and fibroblasts [27]. These AECs secrete several components (e.g. transforming growth factor (TGF)-β, connective tissue growth

factor (CTGF), platelet-derived growth factor (PDGF), endothelin-1, vascular endothelial growth factor (VEGF), fibroblast growth factor (FGF) and CXC chemokine ligand 12 (CXCL12)). This leads to the differentiation of monocytes, fibrocytes and fibroblasts into a fibrogenic cell type, the myofibroblast, which is responsible for the formation of extracellular matrix (ECM). Thus, an abnormal/dysfunctional repair process results in (myo)fibroblast infiltration and activation, abnormal re-epithelialisation and accumulation of excessive ECM eventually destroying the lung architecture [28]. The hallmarks of this scarring disease include accumulation of myofibroblasts, fibroblasts and extracellular matrix components (Figure 3). The complex interplay of cells and processes depends on the type of ILD and remains highly questioned and debated [29]. In the following paragraphs, a possible cellular mechanism specifically dedicated to IPF will be further explained (Figure 4).
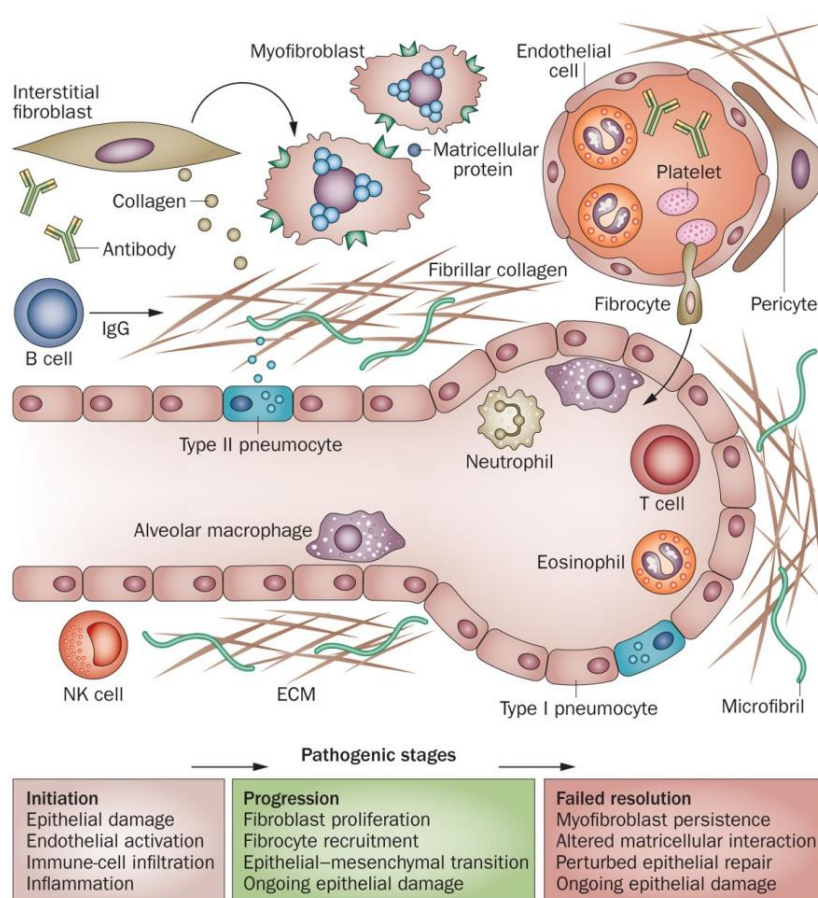
Figure 4: cellular pathogenesis of pulmonary fibrosis.
Epithelial, endothelial and interstitial compartments, together with components of the innate and adaptive immune system, interact with the ECM and with each other to produce collagen-rich ECM. Damage of the epithelial cells initiates a repair pathway including the recruitment of fibroblasts and myofibroblasts. ECM=extracellular matrix (figure and legend adapted from Wells *et al.* (2014))[30]

1.3.1.1. Alveolar epithelial cells

Alveolar epithelial type 2 cells (ATII cells) are the predominant epithelial progenitor cells. In healthy individuals, they play an important role in the lung homeostasis by secretion of different mediators

and ultimately the regeneration of the epithelium [31]. Different hypotheses exist on the role of ATII cells in pulmonary fibrosis [29]. One hypothesis states that AECs can transdifferentiate into (myo)fibroblasts by epithelial to mesenchymal transition (EMT). During this process, epithelial cells lose their specific characteristic markers (E-cadherin and zona occludens-1) and obtain specific mesenchymal markers (fibroblast-specific protein-1 and α-smooth muscle actin) [32]. Another hypothesis postulates that injured and apoptotic ATII cells are unable to control mesenchymal cells resulting in excessive proliferation and ECM production. The last hypothesis states that injured/dysfunctional AECs produce stromal cell-derived factor 1 (CXCL12) which attracts circulating fibrocytes to the site of injury resulting in increased amount of fibroblasts [29]. Nevertheless, it is believed that AECs play an important role in the initiation of the disease by producing profibrotic mediators and by inducing migration and differentiation of profibrotic cells.

1.3.1.2. Myofibroblasts

Injury of the epithelium is an important hallmark in the initiation and development of pulmonary fibrosis. Damaged alveolar epithelial cells (AEC) initiate a repair process that is dysregulated and ineffective. This leads to fibrosis by inducing a differentiation process by which resident interstitial fibroblast transdifferentiate into myofibroblast [26,33]. The myofibroblast is one of the key players in pulmonary fibrosis. They are characterized by *de novo* expression of α-smooth muscle actin and excessively produce ECM [34]. Three possible origins have been suggested for myofibroblasts although the exact relative contribution of all pathways remains unclear in IPF and pulmonary fibrosis [26]. First, resident fibroblasts can differentiate into myofibroblast after repetitive stimulation with pro-fibrotic mediators. Second, epithelial cells can transdifferentiate by the EMT in (myo)fibroblasts and finally circulating fibrocytes can be attracted to the lungs to differentiate into myofibroblasts [32,35]. During endoMT (endothelial to mesenchymal transition), endothelial cells lose specific markers (vascular endothelial cadherin) and require mesenchymal markers (e.g. α-SMA, vimentin and type 1 collagen). This cellular transdifferentiation process can be induced by TGF-β and is possibly an important source of myofibroblasts linked with pulmonary, cardiac and kidney fibrotic diseases [36]. In murine models, this process has been linked with pulmonary fibrosis; it has not been fully elucidated whether this also happens during pulmonary fibrosis in humans [29,37-39].

1.3.1.3. Fibroblasts

Fibroblasts are tissue mesenchymal cells and maintain a normal and healthy ECM by expressing matrix metalloproteinases (MMPs) and tissue inhibitors of metalloproteinases (TIMPs). Injury of the AECs activates the migration of fibroblasts to the site of injury and induces the differentiation of fibroblasts

to myofibroblasts [29]. Myofibroblasts overproduce ECM components such as collagen. Together with a reduced removal of ECM, this results in pulmonary fibrosis [27].

1.3.1.4. Fibrocytes

Fibrocytes are circulating mesenchymal precursor cells of fibroblasts that express the stem cell marker CD34 and leukocyte common antigen CD45. Fibrocytes include only a small fraction of circulating leukocytes in humans. Studies have already found that inhibition of recruitment of these cells to the site of injury, and inhibition of differentiation into fibroblasts could limit the development of pulmonary fibrosis [40]. Apart from the effect of collagen production and differentiation into (myo)fibroblasts, fibrocytes might also promote pulmonary fibrosis through the modification of the microenvironment. They produce a certain number of chemokines ((e.g. IL-8 and macrophage inflammatory protein (MIP)-1α) and growth factors (e.g. macrophage colony-stimulating factor (M-CSF), TGF-β, FGF, PDGF and VEGF) that are implicated with pulmonary fibrosis.

1.3.2. Inflammatory process

The innate and adaptive immune system both contribute to the development of pulmonary fibrosis [28]. However, treatment that influences the inflammatory process (e.g. corticosteroids) often failed or even worsened the disease progression, raising several questions regarding the role of inflammation in pulmonary fibrosis [41]. To this day, it is not clear yet, up until which level inflammatory processes are a driver of pulmonary fibrosis development, although for a few (key) players we will here briefly discuss their role in inflammation in IPF.

1.3.2.1. Neutrophils

Neutrophils are the first cells to migrate to a place of injury upon tissue damage. They are attracted by several chemokines, with the most important one IL-8 [41]. In IPF patients, IL-8 is increased in sputum and BALF pointing to neutrophil activation and attraction [42]. Neutrophils phagocytose, have cytotoxic mechanisms and release pro-inflammatory cytokines and reactive oxygen species (ROS) [43]. Moreover, the production of neutrophil elastase has both pro- and anti-fibrotic properties. Neutrophil elastase can break down collagen-IV and elastin (anti-fibrotic) and on the other hand, neutrophil elastase promotes fibroblast proliferation, myofibroblast differentiation and TGF-β activation (profibrotic) [44].

1.3.2.2. Macrophages

Macrophages are key players in tissue repair and immunity responses. Depending on environmental changes, a macrophage can interchange between an M1 and M2 phenotype. M1 macrophages are pro-inflammatory and produce TNF-α, IL-6, IL-1. M2 macrophages have both anti-inflammatory and profibrotic properties and are involved in wound healing [41]. They secrete several cytokines such as TGF-

β, PDGFα, IGF1 and VEGF. Moreover, the M2 macrophage can contribute to the formation of ECM [45]. As expected, M2 macrophages are present in fibrotic lungs and particularly VEGF concentration in serum inversely correlates with the clinical parameters in IPF (monthly change in percent predicted vital capacity) [46,47]. Additionally, in IPF patients, elevated concentrations of CCL18 in BALF (most likely produced by macrophages) were a predictor of acute exacerbations [48].

1.3.3. Concluding remarks

Numerous cell types contribute to the pathogenesis of pulmonary fibrosis and not all mechanisms are clear yet. A brief overview was given of several key players in IPF. Other interesting factors that play a role in pulmonary fibrosis are endothelial cells, monocytes, mast cells, T cells and B cells. Moreover, substantial cytokines and chemokines are involved in the process. To conclude, pulmonary fibrosis is a complex disease that results from the interaction between epithelial cells, endothelial cells, fibroblasts and immune cells [28]. Up until today, it is not fully clear yet what is cause and consequence, which cells are essential for repair or accelerate the fibrotic process, making it difficult to identify proper therapeutic targets, possibly explaining the several failed clinical trials for IPF and other pulmonary fibrosis diseases [49]. Despite these numerous failed trials, there are currently two drugs available for IPF patients: Nintedanib and Pirfenidone[14,15]. Nintedanib (BIBF 1120) is a tyrosine kinase inhibitor and targets the fibroblast growth factor receptor (FGFR) 1, 2 and 3, platelet derived growth factor receptor (PDGFR) α and β and vascular endothelial growth factor receptor (VEGFR) 1, 2 and 3 [50,51]. The exact cellular mechanism by which Pirfenidone alters the fibrosis process is still not fully understood [52]. Other new potential therapeutic approaches are being explored [15,16,49].

2. Animal models of pulmonary fibrosis

Animal models are an indispensable tool for (pulmonary) research. To understand the pathophysiology of pulmonary fibrosis, its treatment options and the process of lung injury, inflammation and fibrosis, a variety of models are designed. In murine models, several agents can induce pulmonary fibrosis-like features resembling those seen in patients through different routes of administration. In the following section, we will give an overview of the most important animal models that resemble pulmonary fibrosis in mice with both their advantages and disadvantages (Table 3).

Table 3: Main advantages and disadvantages of pulmonary fibrosis rodent models (adapted from Moore *et al.* 2008) [53]

	Advantages	Disadvantages
Bleomycin	- Well-characterized - Clinical relevance - Different administration routes - Fibrosis develops after 14-28 days	- Claimed to be self-limited - Mortality bias
Silica	- Persistent fibrotic stimulus - Nodules resemble with those seen in humans exposed to occupational dust and particulates	Fibrosis development after several weeks
Asbestos	Clinical relevance	- Uneven distribution of fibrosis after intratracheal instillation - Very specific for one compound
Radiation	- Clinical relevance - Well characterized susceptibility differences among mouse strains	- Up to 30 weeks for fibrosis to develop - High housing costs
Transgenic	- Study of one particular molecule of a pathway possible - Inducible promotors are available allowing induction of fibrosis in adult animal	Lack of multi-genetic environment of fibrosis

2.1. Bleomycin

The bleomycin-induced pulmonary fibrosis model is the most frequently used and established model to study pulmonary fibrosis and therapy options [53]. Bleomycin is a chemotherapeutic antibiotic and initially used for treatment of carcinomas and lymphomas in a clinical setting. Pulmonary fibrosis is an unwanted side-effect of the antibiotic which led to the development and use of this animal model to study the fibrotic process [54]. Bleomycin induces direct damage of the AECs by induction of free radicals, double stranded DNA breaks and oxidative stress. This results in necrosis, apoptosis and activation of an acute inflammatory phase ultimately leading to fibrosis [55].

This well-established model is used in numerous types of animals including rats, mice, hamsters, guinea pigs and dogs and can be induced by different administration routes that have been evaluated such as intratracheal administration, intraperitoneal, subcutaneous or intravenous injection and inhalational [54]. There are two commonly used forms: the single-dose model and the repetitive model. For the single-dose model, fibrosis develops in a relative short time period (2-4 weeks after intratracheal instillation). The disease course after bleomycin administration can be divided in an early acute lung injury phase (days 0-7), fibroproliferation phase (days 3-14) and fibrotic phase (days 14-28) [6]. The advantage of this model are its histological similarities with IPF regarding intra-alveolar buds, mural incorporation of collagen and obliteration of the alveolar space although a full UIP pattern is not observed [55]. Another advantage is its ease of induction. Importantly, the model suffers from serious limitations: a high mortality rate, high variability, rapid development of fibrosis, prone to survival bias and it is claimed to be self-limiting in time. This is contradictory to the human pathology, which is slow, progressive and irreversible [54-56]. Furthermore, the short timespan over which fibrosis develops and peaks limits the use of this model towards therapeutic testing. The repetitive model, in which bleomycin is administered repeatedly via endotracheal intubation or systemic intraperitoneal and intravenous injections, mimics more the clinical situation of repeated injury and results in more robust fibrosis present in the lungs [57]. When administering 0.04U of bleomycin every two weeks endotracheal with eight doses in total, fibrosis remains present up until 20-30 weeks after the final dose administration. When administering systemically 20 mg/kg twice weekly for 8 weeks, fibrosis appears after 4 weeks and remains present up until 12 weeks. Advantages of the repetitive model are the attenuated neutrophilic inflammation at the later stage, the presence of fibroblastic foci (although often rare) and persistent fibrosis [58].

2.2. Silica

Silica instillation in the lungs leads to fibrotic nodules that resemble those seen in patients exposed to environmental triggers such as mineral dust and particulate aerosols [57]. Therefore, this model is often used to study the effects of these occupational exposures. When crystalline silica particles enter the lungs, they trigger alveolar macrophages, epithelial cells and fibroblasts resulting in the release of several inflammatory mediators (e.g. cytokines and reactive oxygen species (ROS)) [59]. Apart from this inflammatory response, inhalation of silica particles results in necrosis, tissue damage and fibrosis in the lungs [60-62]. Toxicity results from (1) direct cytotoxicity to AECs, (2) activation of alveolar macrophages and AECs leading to secretion of inflammatory cytokines and chemokines and (3) stimulation of secretion of pro-fibrotic mediators from alveolar macrophages and AECs (Figure 5) [61].
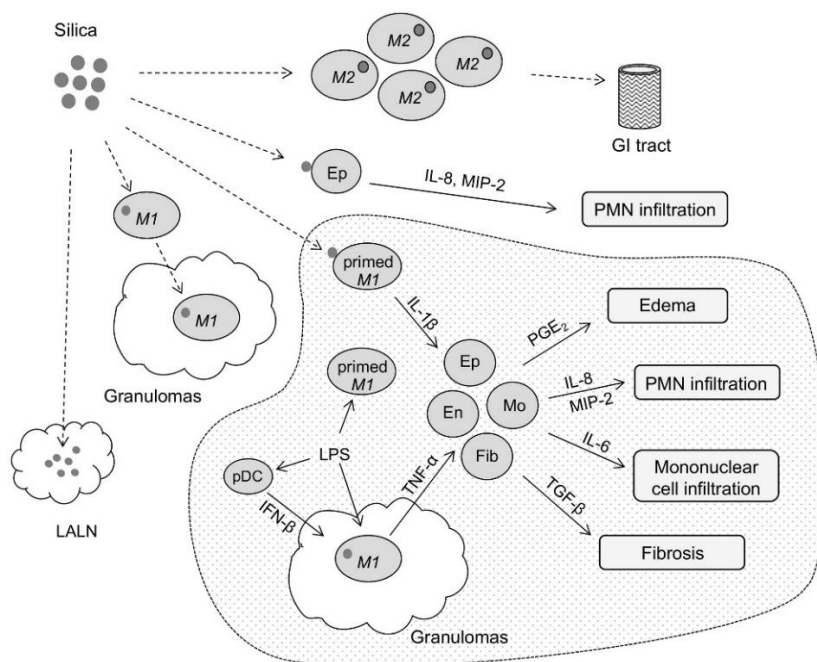
Figure 5: hypothetical mechanisms for silica-induced lung inflammation and fibrosis.

Silica particles that enter the lungs are primarily taken up by M2 macrophages without production of inflammatory cytokines and transferred to the GI. When exposure is prolonged, the lung silica burden reaches a ''particle overload'' level, at which M2 macrophages cannot maintain the amount of particles. Free silica particles are taken up by M1 macrophages that can secrete various inflammatory cytokines. Silica-loaded M1 macrophages initiate granuloma formation further engulfing silica particles. The alveolar epithelial cells (Ep) can be stimulated to produce chemokines by silica particles. Simultaneously, free silica particles translocate to lung-associated lymph nodes (LALN) where they induce hyperplasia. ''Particle overload'' may facilitate silica-induced granuloma formation and transfer of silica particles from the deep lung to LALN. Cytotoxicity of silica can decline the ability of M2 macrophages to clear foreign matter, resulting in increased level of bioactive lipopolysaccharide (LPS) in the lung. When LPS concentration in the lung reaches a certain level (dotted area), LPS primes M1 macrophages to accumulate proIL-1β and NALP3 inflammasome. Silica particles activate NALP3 inflammasome, which results in the activation of caspase-1 (IL-1β converting enzyme), and accordingly mature IL-1β is produced. At the same time, LPS may stimulate M1 macrophages and plasmocytoid dendritic cells (pDC) to produce TNF-α and IFN-β, respectively. IFN-β may enhance the production of TNF-α in M1 macrophages. The elevated levels of IL-1β and TNF-α produce progressive lung inflammation and fibrosis (figure and legend adapted from Kawasaki *et al.* (2015) [61]).
M1: classically activated/inflammatory macrophages, M2: alternatively activated macrophages, pDC: plasmacytoid DC, Ep: alveolar epithelial cells, En: endothelial cells, Fib: fibroblasts, Mo: monocytes, LALN: lung-associated lymph nodes, PMN: polymorpho-nuclear neutrophils and GI tract: gastrointestinal tract.

Silica can be administered to the lungs of mice via aerosolization, oropharyngeal aspiration or intratracheal instillation [57,63]. The silica particles are not easily cleared from the lungs leading to persistent fibrotic lesions [64]. This is one of the main advantages of the model and gives an opportunity to evaluate potential therapeutics. Additionally, the low cost and limited technical skills to set up this model are another asset. Disadvantages are the lack of reproducibility of the fibrotic pattern and the UIP pattern observed in IPF patients is not present in this model [57,65].

2.3. Asbestos

Pulmonary fibrosis can be induced by a single intratracheal instillation of asbestos fibres. This animal model has led to insights in the pathogenic mechanisms for both IPF as well as asbestosis. Asbestos

fibres induce oxidative stress, alveolar epithelial cell apoptosis, overproduction of pro-fibrotic cytokines and M2 macrophage activation, which ultimately leads to myofibroblast differentiation and activation, triggering ECM production [66-69].

Two different administration routes have been used: intratracheal instillation and inhalation. When intratracheal instillation is used, the distribution of fibrotic lesions is often uneven and more central rather than subpleural [57]. This has limited reproducibility concerning clinical histopathological findings. Inhalation of asbestos particles partly eliminates this problem. Disadvantages of the inhalation method are the prolonged time needed to develop fibrosis (up to one month) and the requirement of a special inhalation chamber. Fibrosis that develops in the asbestos model is persistent and can be progressive [67]. Moreover, it is very specific to one occupational exposure. This makes it less useful for general pre-clinical research in the field of fibrosis.

2.4. Radiation

Radiation-induced fibrosis is a clinically relevant model to study the side effects in the field of radiotherapy. One single radiation dose of 12-15 Gy to a whole mouse body (male LAF1 mice) leads to pulmonary fibrosis after 20 weeks [70]. When only the thorax is irradiated, which is more often used than whole body irradiation, it can take up to 24 weeks before fibrosis develops [53]. Ionizing radiation influences biological tissue in several ways: first, the x-rays interact with water molecules resulting in reactive oxygen species and free radicals. Second, the x-rays disrupt the chemical bonds of several biomolecules (nucleic acids, proteins, lipids etc.) [71,72]. The radiation damages pulmonary epithelial and endothelial cells, which results in an inflammatory response. It is believed that induction of fibrosis can be attributed to DNA damage and the release of TGF-β.

The main disadvantage of this model is the long time before fibrosis develops, which implicates high housing costs. Advantages of this model are the clinical relevance, the low mortality rate and the well-characterized susceptibility in inbred mouse strains [53].

2.5. Transgenic

Transgenic mouse models, in which a certain cytokine or enzyme is overexpressed, have led to major insights in the pathophysiology and the bio-molecular process of pulmonary fibrosis. Gene transfer with adenoviral or lentiviral vectors and transgenic approaches are both methods that have been used to overexpress pro-fibrotic cytokines (e.g. TGF-β, IL-13, TNF-α) leading to a fibrosis-like phenotype [53]. Models overexpressing a certain cytokine are useful to study the downstream signalling pathways and effects of this certain molecule. Moreover, since these models spontaneously develop over time, some have been suggested as better models compared to models, which depend on an external stimulus to

induce pulmonary fibrosis [6]. One major disadvantage of transgenic animal models is the fact that one gene is artificially overexpressed to induce pulmonary fibrosis, which neglects the multi-genetic environment of pulmonary fibrosis in patients where not one particular molecule in the body is overexpressed [57].

2.6. Is there an "ideal" pulmonary fibrosis animal model?

An animal model needs to be reproducible and uniform, easy to induce, cheap and easily available. Numerous pulmonary fibrosis animal models are available but identifying the model, which represents the human situation, is a difficult task. All animal models have the inherent limitation that they never truly mimic the clinical situation and fully recapitulate all aspects of the disease [57]. Important aspects of IPF and pulmonary fibrosis in general are the progressive and irreversible character and predisposition for older males. These aspects are difficult to mimic in a preclinical setting. Moreover, histologically no animal model fully displays the UIP pattern as found in IPF patients. This can be possibly explained by the anatomical differences of the lungs in mice versus man and the distinctive pathobiological mechanisms in the human disease [6,53]. Additionally, IPF is a disease of unknown aetiology whereas all animal models have a very specific trigger to induce pulmonary fibrosis. It is important to take into account the limitations when choosing an animal model for a certain study. Each study should evaluate separately which animal model fits best.

3. Preclinical evaluation of pulmonary fibrosis

In the clinic, diagnosis of pulmonary fibrosis is often based on HRCT, while in a preclinical setting researchers often use endpoint measurements (biochemical assessment of collagen content, gene expression, histological assessment of fibrotic distribution and lung function) to accurately evaluate the severity of lung disease and drug efficacy. These measurements provide detailed physiological, molecular and cellular information and have already led to great insight in the pathological processes of pulmonary fibrosis. However, they only provide information of a certain aspect of the disease and at certain timepoints. Additionally, we can use *in vivo* imaging approaches to provide a full picture of the entire disease process in every single animal. In the following section, an overview of endpoint measurements as well as imaging modalities used for pulmonary fibrosis research is given.

3.1. Invasive techniques to evaluate lung fibrosis in mouse models

3.1.1. Biochemical assessment of collagen

The hydroxyproline (OH-proline) assay is the most used biochemical technique to measure the collagen content in a lung sample. OH-proline is a non-proteinogenic amino acid that is almost only present in collagen and correlates with the level of collagen present and the severity of fibrosis (1 µg of OH-proline corresponds to 6.94 µg collagen) [73]. Apart from the OH-proline assay, Sirius red staining can be used for a colorimetric estimate of the amount of fibrosis in tissue homogenate. However, this often overestimates the amount of fibrosis present in the sample and underestimates the differences between diseased and control groups [74]. This assay only uses a small part of the original sample and due to the staining protocol, small variations are often overestimated due to the calculations. Lastly, a Sircol collagen assay kit can determine collagen, although this only measures the "newly formed" acid and pepsin-soluble collagen. It does not measure the insoluble collagen, which is integrated in "mature" scar tissue [6].

Often, distribution of fibrosis is not homogenously over both lungs. In this case, it is advised to use all lung lobes to perform biochemical assessment of collagen [6,75]. This implies that there is a counterbalance between excluding the chance for sampling errors versus the opportunity to measure different readouts. Taken together the advantages and disadvantages, the American Thoracic Society workshop of 2017 recommends the OH-proline assay as a primary endpoint for preclinical evaluation of therapeutics [6].

3.1.2. Histopathological assessment of fibrotic distribution

Different stainings can be used to histologically evaluate fibrotic lesions with microscopy (Figure 6); Masson's trichome and Sirius red staining. A Masson's trichome staining is used to assess fibrosis. The

fibrotic severity can be semi quantified on stained slices by the Ashcroft scoring system [76]. Random sections are examined and a grade of fibrosis is given (0 for normal lung and 8 for total fibrous obliteration of field). A Sirius red stain binds to the collagen fibres allowing visualisation of collagen as birefringent structures under polarized light. Moreover, brightfield microscopy can be used to semiquantify fibrosis by morphometric visual scoring systems [6,77]. The morphological scoring systems e.g. Ashcroft scoring is often subjected to inherent bias and interobserver variations. Therefore, it is recommended to always combine histology with biochemical assessment of collagen [6].
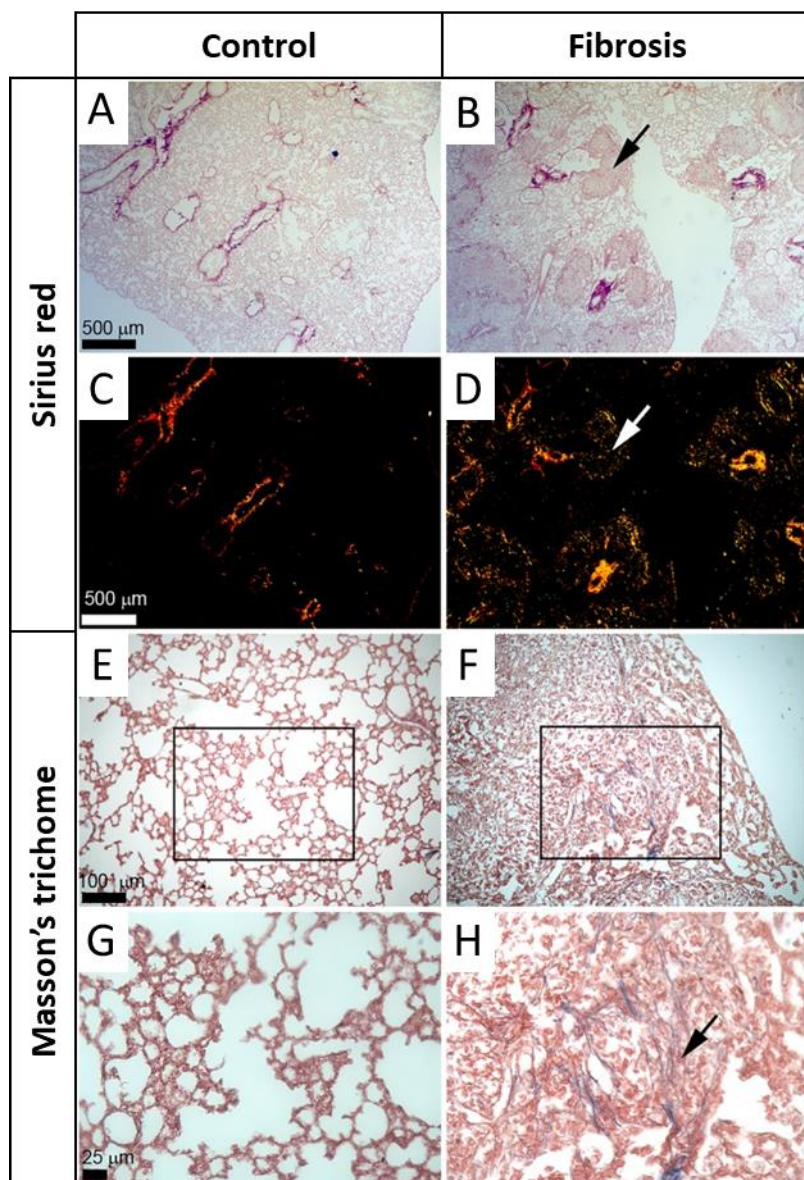
Figure 6: histological evaluation of fibrotic distribution with different staining.
Representative staining of lung from saline- (left panels) or silica-instilled animals (right panels) at eight weeks post-instillation. Picrosirius red staining is shown in panels A-D, (A) Representative lung architecture in saline-instilled animals. (B) Fibrotic nodules (representative nodule indicated by arrow) are evident in the lungs of silica-instilled animals. Representative Picrosirius Red staining under polarized light shows thick (red) and thin (green/yellow) collagen fibrils in lungs of saline-instilled control animals (C) and silica-instilled animals (D). Representative fibrotic nodule indicated by a white arrow (D). Masson's Trichrome staining is shown in panels E-H. Lung architecture in a representative saline-instilled (E) or silica-instilled (F) animal. High magnification images (boxes in (E) and (F) indicate inset) of Masson's Trichrome stain indicate presence of collagen fibrils (representative fibril indicated by arrow) in silica-instilled animal (H) versus saline-instilled lungs (G) (figure and legend adapted from McDonald *et al.* (2017) [78]).

Due to the bias implicated in the scoring system, the American Thoracic Society workshop of 2017 recommends to focus on morphological and molecular characteristics of fibrosis. However, they suggest that histology should always be accompanied by the use of a biochemical assessment of collagen content in the lungs [6].

3.1.3. Lung function measurements

Non-invasive and invasive lung function measurements are available with both their benefits as well as limitations. Unrestrained whole-body plethysmography, where the animal is conscious, is a non-invasive method to monitor spontaneous airway mechanics. The parameters resulting from these measurements include, tidal volumes, peak flows, frequency of breathing, time of inspiration and expiration, etc [79,80]. Until now, these parameters show little to no differences between fibrotic and control lungs, therefore, this technique is not useful [81].

Two invasive methods are commercially available: Buxco (Buxco Research Systems, Wilmington, NC) and flexiVent (SCIREQ, Montreal, PQ, Canada) and deliver a broader range of parameters. Both methods are mostly performed on anesthetized and tracheotomised animals and are therefore terminal [79]. Although, there have been efforts to perform the measurements repeatedly, but this was only partially successful [82]. These techniques determine clinically relevant parameters e.g. vital capacity, resistance and compliance [83,84]. Vanoirbeek *et al.* and others used the flexiVent system to evaluate lung mechanics in a bleomycin-induced lung fibrosis mouse model and found differences in tissue damping and tissue elasticity [81,85]. Quasi static pressure-volume (PV) curves are also used, and it is suggested that it is more sensitive than forced oscillation values for detecting inflammation and fibrosis [85]. Lung function measurements have already been used to successfully evaluate anti-fibrotic therapeutics *in vivo* mostly in the bleomycin model [86,87]. The American Thoracic Society workshop of 2017 does not recommend the use of lung function measurements as a routine part of preclinical evaluation of drugs and animal models for pulmonary fibrosis, although it acknowledges it has added values if used together with biochemical assessments of fibrosis [6].

3.1.4. Additional remarks on endpoint measurements

Ex vivo analysis on tissue samples can provide the most accurate and detailed cellular and molecular analysis of the disease. They (histology, PCR, ELISA etc.) are however intrinsically not suitable to follow the kinetics of disease and host response processes that are, by definition, dynamic in space and time. Moreover, *ex vivo* analysis require multiple animals to be sacrificed at several time points during the study, carrying the ethical burden of overconsumption of animals to overcome the statistical issues inherent to high inter-animal variation that would otherwise reduce the power of experiments. Two-dimensional sampling is also too limited for processes that are not evenly distributed throughout an entire organ such as the pulmonary lobes in lung fibrosis [75]. Imaging modalities have the potential to overcome several of these challenges.

3.2. Non-invasive visualisation of lung fibrosis

Imaging modalities such as µCT, MRI, PET and optical imaging are non-invasive and can provide a detailed three-dimensional image of the animal and the different organs (e.g. the lung) under investigation [88,89]. It is possible to perform repetitive imaging allowing the follow-up of every individual animal throughout the entire disease process. The three R principle of animal ethics further underscores the importance of non-invasive imaging techniques in preclinical research; the number of animals needed can be highly reduced [90]. Despite these advantages, imaging modalities are not routinely implemented in preclinical lung (fibrosis) research. Reasons given for this are high costs, requirement of expertise and the challenge of imaging the lungs [6].

3.2.1. Micro-computed tomography

Due to its high air-tissue contrast, micro-computed tomography (µCT) is an excellent technique to study and quantify lung disease burden such as pulmonary fibrosis, lung metastasis and lung infection [75,91-94]. Figure 7 gives an example of a control versus a fibrotic mouse lung.
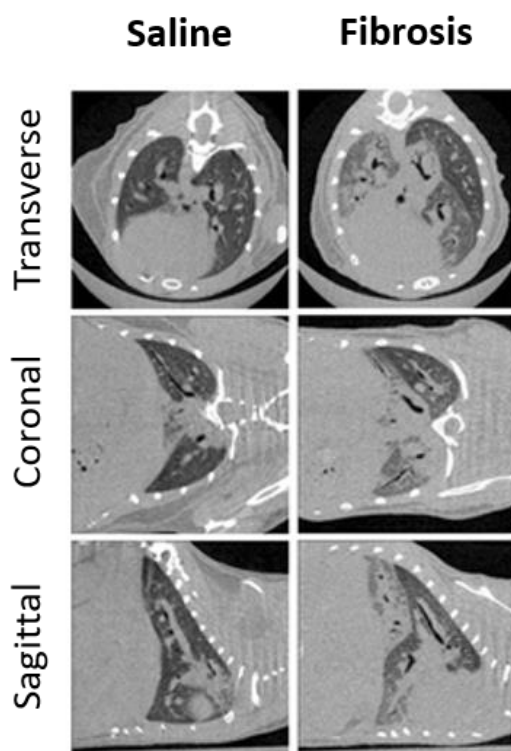
Figure 7: µCT scan of a control versus fibrotic mouse lung. Transversal, coronal and sagittal µCT images are given of a control (saline) and fibrotic mouse (21 days after bleomycin instillation) (figure adapted from Ruscitti *et al.* (2017) [95]).

µCT is a volumetric imaging modality that uses ionizing radiation or x-rays to create cross-sectional images [96]. The x-ray source rotates around the object/animal and produces x-rays (photons), which are aimed at the object (Figure 8). The object attenuates or absorbs a certain amount of the x-rays and at the end; the photons that reach the detector are measured. This procedure is repeated at various angles around the object.
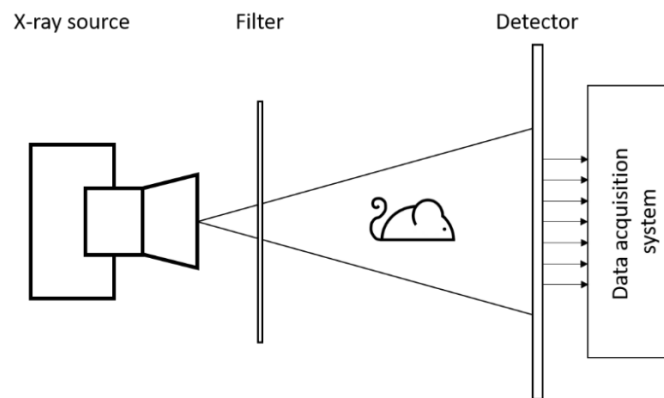
Figure 8: schematic representation of a CT scanner.

The x-ray projection data needs to be reconstructed to create cross-sectional data. Each cross-sectional slice consists of 3D pixels (voxels) all representing a part of the object or tissue and every voxel is assigned a CT number reflecting how much that particular part attenuated the x-ray beams [97]. This CT number is often represented in Hounsfield Units (HU) [98].

Table 5: HU values for different tissues [98].

Tissue/substance	Hounsfield Unit
Air	-1000
Fat	-100
Water	0
Muscle/soft tissue	+40
Bone	+1000

The technique µCT can be used for *ex vivo* and *in vivo* imaging. With *ex vivo* imaging, one can obtain a 3D image of the entire lung with isotropic micrometre resolution [8]. In this thesis, we will focus on *in vivo* imaging, where living animals are used. This implies that the animal is breathing and radiation doses delivered to the animal need to be taken into account. µCT has already proven to have important benefits for longitudinal evaluation of disease in preclinical animal models [75,91,99-102].

µCT enables the quantification of several morphological and anatomical lung biomarkers that describe disease progression and host response ideal for longitudinal follow-up of lung diseases [8,103]. These biomarkers are extracted from a volume of interest covering the lungs thereby avoiding large blood vessels and the heart. Based on a full stacked histogram, a chosen threshold separates the voxels corresponding with radiodense areas from the radiolucent lung voxels, representing respectively the non-aerated lung volume and the aerated lung volume. Moreover, also the total lung volume (sum of non-aerated and aerated lung volume, or all the voxels within the lungs) and mean densities within these lung volumes can be derived. Hereby, we can differentiate between pathologies presenting as

hyperdense areas (infiltrations, consolidation or atelectasis) versus pathologies causing radiolucency on CT such as hyperinflation, air trapping, or emphysema. The non-aerated lung volume is the biomarker that directly quantifies lung disease burden such as lung metastasis, infection, fibrosis and inflammation in animal models [100,103-109].

Previous studies have already implemented μCT as a modality to evaluate pulmonary fibrosis mouse models and used different μCT-derived readouts. Cavanaugh *et al* correlated the *in vivo* μCT-derived percentage of lung damage with histology in a bleomycin induced mouse model [110]. They determined this lung damage by subtracting the lung volume at sacrifice from the baseline volume. Ruscitti *et al.* concluded that μCT was in good agreement with histological readouts (Ashcroft score, percentage of collagen content and percentage of alveolar air area) [95]. They derived the distal airway radius (the average airway lumen radius per zone) and an FRI fibrosis parameter (a combination of blood vessels and fibrosis based on tresholding segmentation) from the μCT scans. Rodt *et al.* used an observer rating scale to evaluate the quality and amount of lung consolidation and quantified the aerated lung areas as a surrogate marker for fibrosis [111]. Together with other studies, these results show the efficacy of μCT for preclinical lung fibrosis research [75,89,112].

μCT is not able to differentiate inflammation from fibrosis based on thresholding, which would be a great added value to this technique. Although, currently there are no techniques available for animals that can do this. Inflammation and fibrosis result both in an increase of tissue density and therefore the hyperdense voxels can represent both inflammatory and fibrotic processes. To further separate inflammation from fibrosis, which is an important aspect of pulmonary fibrosis research, additional imaging techniques such (e.g. MRI, PET and optical imaging) or *ex vivo* readouts (e.g. histology, OH-proline assay, …) are needed [88].

Both high resolution and sensitivity are needed to create an ideal image and there is always a trade-off between both aspects. Resolution is the minimal distance two point-objects have to be separated to be resolvable in the image. Since often higher scanning times are required for higher resolution, there is a trade-off between resolution and the radiation dose given to the animal. Therefore, for *in vivo* imaging, it can be possible to reach up to a resolution of 15 μm in rats without adverse effects seen after weekly scanning for eight weeks [113,114]. Image quality also depends on respiratory motion and heartbeat artefacts, which are present since we are imaging living animals. To avoid these movement artefacts, different gating approaches have been developed to create high-resolution scans. A first gating approach is prospective gating where images are acquired during the appropriate breathing cycle [115,116]. This approach synchronises the scan with a certain breathing phase, either by restricting acquisition only to the stable expiration phase or by using breath hold manoeuvres. The

latter one is not without risk in small rodent animals [117-119]. A second gating option is retrospective gating, with two alternatives available; time-based and image-based retrospective gating. With this approach, a large number of images are taken during acquisition to then afterwards sort these images in the right breathing phase [120,121], thus oversampling is needed.

A major concern when using µCT is the repeated exposure of the living animal to x-rays. In the field of radiotherapy, the adverse effects of radiation have been extensively investigated. The doses used in these studies (4-20 Gy) are much higher compared to the doses delivered by a µCT scan. Little is known regarding the effects of repeated exposure to low-dose radiation [122-125]. To describe the radiation dose delivered by µCT, one can use the measure 'absorbed dose' which is the energy absorbed per unit of mass, expressed in grays (Gy) [126]. The ionizing radiation in µCT acts on biological tissue through two main effects: 1/ the x-rays interact with water molecules resulting in reactive oxygen species and free radicals and 2/ x-rays may disrupt the chemical bonds of several biomolecules (nucleic acids, proteins, lipids etc.) [71,72]. For example, when x-rays interact with genetic material, they can create DNA base modifications, base damage or double-stranded DNA breaks. To assess the biological effects of radiation, not only the cumulative dose of radiation is important, but also the factors that determine this, such as dose-rate, scan frequency and type of exposed tissue. Depending on the intrinsic repair capacity, tissues exposed to the relatively low radiation dose of µCT are able to repair the damage. It has already been established that repeated µCT does not affect the lungs and general health of healthy animals considering radiation toxicity [127]. Nevertheless, any remaining concerns related to potential radiotoxicity of the cumulative radiation dose to diseased animals need to be ruled out before we can safely implement µCT for longitudinal studies [8].

Based on the current evidence, the American Thoracic Society workshop of 2017 does not recommend µCT for preclinical assessment of therapeutics [6]. However, it acknowledges its potential advantages and states that further investigation is needed.

3.2.2. Magnetic resonance imaging

In contrast to µCT, magnetic resonance imaging (MRI) uses electromagnetic radiation to detect the orientation of protons in the presence of a strong magnetic field [96]. It visualises anatomical changes in the lungs. While µCT does not have the ability to distinguish inflammation from lung remodelling processes, MRI has the potential to do this due to its ability to create soft tissue contrast, which is very relevant for lung disease evaluation and pulmonary fibrosis in particularly. Although researchers are still struggling to exploit this potential fully [128-131].

Implementation of MRI for lung imaging can be quite challenging firstly because lungs consist mostly of air and have thus a low proton density resulting in a low inherent signal. Secondly, the inherent air-tissue contrast creates large magnetic susceptibility gradients causing imaging artefacts and high signal decay in standard MR pulse sequences [88,128]. Ultrashort echo time (UTE)-MRI can overcome this problem as shown by Egger *et al.* who have detected small foci of inflammatory and/or fibrotic lesions in a bleomycin-induced pulmonary fibrosis model (Figure 9) [132]. Another study by Vande Velde *et al.* used three different MRI protocols (RARE, UTE and FLASH MRI sequences) in a bleomycin model and concluded that all protocols were able to visualise and quantify the disease progression in a bleomycin model. The UTE-MRI was specifically useful for detecting early-disease changes [128]. Different MRI probes have been used to visualise the collagen deposition and fibrogenesis process in pulmonary fibrosis animal models. Two examples of biological targets are fibrin (gadolinium-based, fibrin-specific probe EP-2104R)[133] and oxidized collagen (allysine-binding gadolinium chelate Gd-oxyamine)[134], although these probes are still not a solution for the distinction of inflammation versus fibrosis.
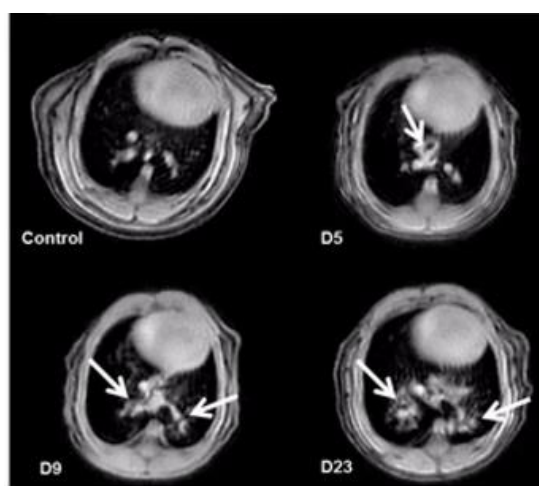
Figure 9: MRI scan of a control versus fibrotic mouse lung (UTE-MRI).
Transversal MRI images of a fibrotic mouse at baseline (control, before bleomycin instillation) and at day 5, 9 and 23 after bleomycin instillation. White arrows indicate lung injury induced by bleomycin (figure adapted from Egger *et al.* (2013) [132]).

A major advantage of MRI is the absence of radiotoxicity. It also has a relatively high spatial resolution and can image deep into the tissue [135]. Disadvantages are, in general, a longer time is needed for image acquisition compared to μCT implying that the animal is under anaesthesia for a long time, equipment is far more expensive than for other imaging modalities and at last, MRI suffers from movement artefacts that can be resolved in a similar way as with μCT [88,96].

Although additional technological developments are needed before MRI can be routinely implemented in a preclinical lung workflow, MRI has the potential to detect the switch from inflammatory to fibrotic processes, which would greatly improve research of pulmonary fibrosis pathology and therapeutic efficacy.

3.2.3. Positron emission tomography and single photon emission computed tomography

μCT and MRI are two methods that use the intrinsic contrast of the lungs to create a three-dimensional image. Another non-invasive imaging option is labelling a specific disease process with targeted contrast agents. Both positron emission tomography (PET) and single photon emission computed tomography (SPECT) are radionuclide imaging techniques that use radioisotope-labelled small-molecule compounds, also known as radioactive tracers, to detect metabolic and molecular processes [88]. Both techniques have been explored for pulmonary fibrosis research by targeting important factors in the fibrotic disease process such as collagen (Figure 10) [121].
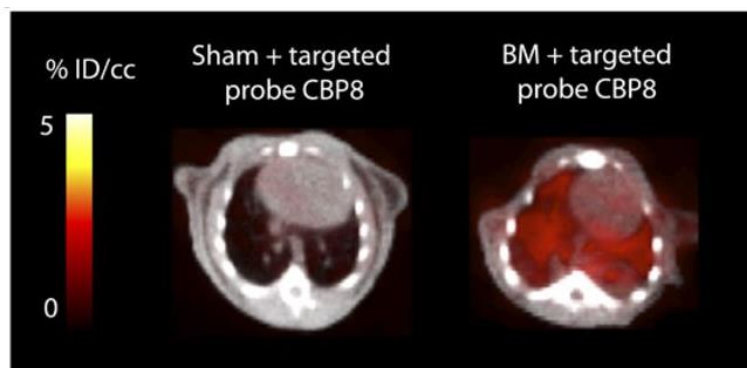
Figure 10: PET/CT scan of a control versus fibrotic mouse lung (with ^{68}Ga-CBP8, a type 1 collagen-targeted PET probe). Representative fused PET-CT images show specific accumulation of 68Ga-CBP8 in fibrotic (BM + targeted probe CBP8) but not in control (Sham + targeted probe CBP8) lungs. Grayscale image shows CT image, and colour scale image shows PET image from integrated data 50 to 80 min after probe injection (figure and legend adapted from Désogère *et al.* (2017) [136]).

One very important hallmark of pulmonary fibrosis is the increased ECM proteins, primarily collagen. Collagen consists of a high amount of the amino acid proline. Therefore, researchers have developed PET protocols to image the uptake of radiolabelled proline analogues for abnormal collagen synthesis [137]. Both ^{18}F-proline (Cis-4-18F-fluoro-L-prolin) and ^{11}C-proline have been evaluated as tracers for pulmonary fibrosis. The silica-challenged regions showed higher ^{18}F-proline uptake in rabbits and this correlated with histopathological findings [138]. This was confirmed by another study using the ^{18}F-proline tracer [139]. A more recent study used a peptide-based probe (^{68}Ga-CBP8) that targets collagen type 1 [136]. They demonstrated the uptake of this tracer in the lungs that correlated with the amount of lung fibrosis in a bleomycin-induced mouse model. Withana *et al.* have used cysteine cathepsin protease probes to monitor the contribution of macrophages to fibrotic disease progression in a bleomycin-induced pulmonary fibrosis mouse model (Figure 10) [140].

PET and SPECT are often not routinely implemented in a preclinical imaging workflow due to some major limitations. They are not very sensitive to small signal changes and there is a potential harmful radiation dose effect when repeated imaging is applied. For PET, apart from the scanner, additional expensive equipment is needed such as a cyclotron and radiochemistry lab to create the isotopes and

to produce the radiolabelled tracers. Moreover, there is an important radiation exposure of people that work with these tracers [88,121].

3.2.4. Optical imaging

Whole body optical imaging is one of the easiest and cheapest *in vivo* imaging approaches. Different techniques exist: bioluminescence imaging (BLI),fluorescence imaging (FI) [121] and Cerenkov luminescence imaging (CLI) [141]. BLI is based on the detection of photons that a biochemical reaction produces, catalysed by luciferase upon administration of a substrate e.g. luciferin (a commonly used example) [142]. This requires genetic engineering of a luciferase cassette in the target cells. Moreover, the lungs in general are quite challenging for optical imaging due to the structure of the airways and alveoli, resulting in overlapping air-liquid interfaces, which causes significant light scattering [143]. Fluorescence imaging uses excitation light to induce fluorescence that comes from a fluorescent reporter protein or dye. Specific fluorescent dyes can visualise certain processes from immune responses implicated with pulmonary fibrosis e.g. cysteine cathepsin targeted imaging probes to monitor macrophages involved in the response after bleomycin instillation in mice [140]. Stellari *et al.* have successfully used a reporter gene construct, containing the luciferase open reading frame under the matrix metalloproteinase-1 (MMP) promoter control region, to monitor pulmonary fibrosis establishment in a bleomycin mouse model (Figure 11) [144]. They used a carrier to deliver the construct to lung tissue to produce transiently transgenize the mice. After intraperitoneal injection of luciferin, the activation of the MMP-1 pathway was observed. However, they did not properly compare inflammation versus fibrosis by optical imaging.
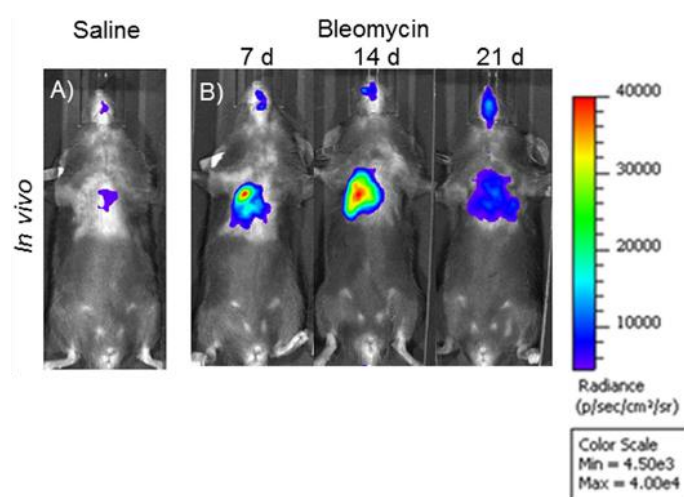
Figure 11: BLI image of a control (saline) versus fibrotic mouse lung.

In vivo representative images of pbMMP-1-Luc transiently transgenized mice treated with saline or bleomycin at 7, 14, and 21 days after bleomycin instillation. Mice were monitored before the treatment to obtain the baseline and posttreatment by *in vivo* image analysis drawing a region of interest over the chest and using an IVIS imaging system (Perkin Elmer Inc., Boston, MA, USA). Light emitted was acquired from specific regions by Living Image® software (Perkin Elmer Inc., Boston, MA, USA) as photon per second per square centimeter and normalized as folds of induction respect to the saline-treated control. (Figure and legend adapted from Stellari *et al.* (2017) [144])

One of the major advantages of these techniques are their theoretical potential to distinguish inflammation from fibrosis. Disadvantages are the low spatial resolution and limited imaging depth.

3.2.5. Which imaging technique to use for pulmonary fibrosis?

From the discussion of the different techniques with their major advantages and disadvantages and summarized in Table 4, it is clear that a single ideal imaging modality does not exist. Every method has its strengths and limitations, which may be overcome by combining different techniques complemented with *ex vivo* methods to estimate the burden of inflammation and fibrosis.

Table 4: overview of the main advantages and disadvantages of non-invasive imaging techniques.

	Advantages	Disadvantages
µCT	• High spatial resolution • High air-tissue contrast • Widely available • Relatively cheap • Structural information • Fast acquisition (minutes)	• Poor soft-tissue contrast • Radiation toxicity (ionizing radiation) • Respiratory and cardiac gating needed • Expertise needed
MRI	• Soft-tissue contrast (potential for distinguishing lung inflammation versus fibrosis) • Good spatial resolution • No radiation toxicity • Structural information	• Expensive • Expertise needed • Challenging scanning protocols • Slow acquisition (minutes to hours) • Respiratory and cardiac gating needed
PET	• Metabolic information/molecular mechanisms • Potential for distinguishing lung inflammation versus fibrosis (with molecular tracers) • Fast acquisition (minutes)	• Poor spatial resolution • Radiation toxicity (ionizing radiation) • Cyclotron on site needed • Optimal tracers needed • Respiratory and cardiac gating needed • Expensive • Expertise needed
Optical imaging	• Easy • Cheap • Fast acquisition • High sensitivity • Potential for distinguishing lung inflammation versus fibrosis (with probes and dyes)	• Poor spatial resolution • Limited imaging depth due to light scattering • 2D technique • No anatomical information

Chapter 2

Rationale and Aims

1. Rationale

Pulmonary fibrosis is a lung disease resulting in scarring of the lung tissue giving patients dyspnoea, dry cough, decline in lung function, worsening quality of life and leading to increased morbidity and mortality. Despite that many compounds have been identified as potentially anti-fibrotic in preclinical studies, there is still no effective curative treatment available due to often failure in clinical trials. As such, pulmonary fibrosis remains a life-threatening condition.

Several challenges may explain the problem to translate preclinical results into potential therapeutics. First, animal models are indispensable for fibrosis and therapy research, but have the inherent limitation that they never truly mimic the human situation. Secondly, most often only prophylactic testing of the drug is performed on these models because of their limited and/or variable fibrotic phase. However, therapeutic drug testing, i.e. when fibrosis is already present, is more representative for the real-life situation and therefore more relevant to evaluate the anti-fibrotic properties. Lastly, in spite of technological advancements, typically only endpoint measurements (e.g. biochemical assessment of collagen content, gene expression, histology and lung function) are used to evaluate the severity of lung disease and drug efficacy. These measurements are unable to give temporal and spatial information on the pathology of the entire lung, often come with high variability and only provide a snapshot of a certain stage of the disease. Moreover, they differ substantially from the readouts used in clinical studies (e.g. computed tomography, lung functional readouts such as forced vital capacity (FVC), forced expiratory volume in 0.1 second (FEV0.1) and Tiffeneau index,…), stressing the need for more clinically relevant readouts in the preclinical screening of new therapeutics, all with the goal to improve translatability of study results from the bench to the bedside .

Ideally, such preclinical readouts provide quantitative data on if, when and how much fibrosis and/or inflammation is present at the time of start of drug administration, essential to evaluate interventions in a truly therapeutic regime. We would also benefit from a mouse model with a stable fibrotic phase over a certain period of time, in which the effect of therapeutic interventions can be examined. Therefore, in this thesis, we optimized a silica-induced pulmonary fibrosis mouse model on which we evaluated the anti-fibrotic properties of a commercial therapeutic and searched for more clinically relevant morphological and functional biomarkers using *in vivo* µCT cross-validated with lung function and standard readouts.

2. Aims

The general aim of this thesis is to improve state-of-the-art approaches that will contribute to better translatability of knowledge about fibrosis, its relation with inflammation and potential treatment strategies. In order to reach this general objective, we explored different specific aims:

Chapter 3

Implement safe, repeated low-dose µCT in preclinical evaluation of lung disease models

The biological effects of ionizing radiation from repeated µCT remain largely unexplored. To deploy the full capacity of high-resolution µCT in the preclinical respiratory research workflow, it is essential to determine and rule out the effects of repeated low-dose radiation on the disease process and host response. Therefore, we investigated the dose and dose effect in healthy animals and different models involving rapidly dividing cells often sensitive to radiation.

Chapter 4

Evaluate whole lung dynamics and characterize a silicosis mouse model of lung fibrosis

At present, the most used and best-characterized animal model for lung fibrosis research and therapy evaluation is the bleomycin model. This model suffers from serious limitations: a high mortality rate, high variability and it is prone to survival bias. The short timespan over which fibrosis develops, lacks a steady-state phase, whichex limits the possibility to do therapeutic drug testing. Moreover, it does not reflect the fact that fibrosis in human patients never spontaneously resolves. The silica-induced mouse model has the potential to overcome these limitations and is able to develop a stable fibrotic state. We established and characterized a silica-induced pulmonary fibrosis mouse model, using µCT-derived anatomical readouts, lung function measurements and *ex vivo* endpoint measurements.

Chapter 5

Evaluate µCT as a modality to assess treatment efficacy in a silicosis mouse model

We assessed a commercial therapeutic (Nintedanib) by *in vivo* µCT and *ex vivo* gold standard readouts in the silica mouse model. With this approach, we assessed the anti-inflammatory and anti-fibrotic potential of Nintedanib.

Chapter 6

Explore novel functional µCT-derived biomarkers

Our 4D µCT protocol covers all four breathing cycles, allowing extraction of both morphological as well as functional biomarkers reflecting/including vital lung capacity and tidal lung volume. As this would enable non-invasive evaluation of lung function, we extracted and validated lung function parameters from longitudinal µCT data of free-breathing animals with different pathologies.

Chapter 3

Radiosafe micro-computed tomography for longitudinal evaluation of murine disease models

Nathalie Berghen*, Kaat Dekoster*, Eyra Marien, Jérémie Dabin, Amy Hillen, Jens Wouters, Jasmine Deferme, Thibault Vosselman, Eline Tiest, Marleen Lox, Jeroen Vanoirbeek, Ellen De Langhe, Ria Bogaerts, Marc Hoylaerts, Rik Lories, Greetje Vande Velde

* both authors share first authorship

Abstract

Implementation of *in vivo* high-resolution micro-computed tomography (μCT), a powerful tool for longitudinal analysis of murine lung disease models, is hampered by the lack of data on cumulative low-dose radiation effects on the investigated disease models. We aimed to measure radiation doses and effects of repeated μCT scans, to establish cumulative radiation levels and scan protocols without relevant toxicity. Lung metastasis, inflammation and fibrosis models and healthy mice were weekly scanned over one-month with μCT using high-resolution respiratory-gated 4D and expiration-weighted 3D protocols, comparing 5-times weekly scanned animals with controls. Radiation dose was measured by ionization chamber, optical fiberradioluminescence probe and thermoluminescent detectors in a mouse phantom. Dose effects were evaluated by *in vivo* μCT and bioluminescence imaging read-outs, gold standard endpoint evaluation and blood cell counts. Weekly exposure to 4D μCT, dose of 540-699 mGy/scan, did not alter lung metastatic load nor affected healthy mice. We found a disease-independent decrease in circulating blood platelets and lymphocytes after repeated 4D μCT. This effect was eliminated by optimizing a 3D protocol, reducing dose to 180-233 mGy/scan while maintaining equally high-quality images. We established μCT safety limits and protocols for weekly repeated whole-body acquisitions with proven safety for the overall health status, lung, disease process and host responses under investigation, including the radiosensitive blood cell compartment.

Introduction

In vivo micro-computed tomography (μCT), an excellent technique to longitudinally evaluate disease progression in small animal models, allows non-invasive visualization of different pathogenic lung processes, (e.g. emphysema, fibrosis, lung infection and metastasis) [75,89,100,102,145-148]. To study disease progression and therapeutic effects in real-time in individual animals, consecutive scanning is essential and enables a manifold reduction in experimental animals, which is of both ethical and economical importance. Yet, the biological effects of ionizing radiation from repeated μCT scanning remain a concern, as these are largely unexplored.

Adverse radiation effects have been extensively studied for the field of radiotherapy. However, these doses (ranging from 4 to 20 Gy) and dose-rates are an order of magnitude higher than doses delivered with repetitive μCT of animal models (less than 800 mGy for a single μCT-acquisition) [122,123,125,127,149]. In healthy animals, weekly or biweekly repeated respiratory-gated μCT scans for 5 to 12 weeks were well tolerated by the animals, had no radiotoxic effects on the lungs and no interference with μCT lung read-outs [127,150]. However, radiosafety was never investigated in disease models involving rapidly dividing cells that may be differently sensitive to x-ray exposure of a μCT scan.

To exploit high-resolution μCT to its full potential and implement it in the preclinical respiratory research workflow, it is essential to investigate potential effects of repeated low-dose radiation on disease processes and host response. This is particularly relevant for radiosensitive organs such as the lungs and/or when the disease process involves rapidly dividing cells, as in many models of cancer, metastasis, inflammation and tissue remodelling [149,151]. Currently, preclinical μCT applications focused mainly on acquiring high-resolution and -quality images while little attention was given to the delivered doses and their potential radiotoxic effects. Standard operating procedures to measure and evaluate dose and dose-effects in a preclinical setting and systematic measurements better characterizing the biological radiation effects are urgently needed. Therefore, this study assessed the effects of low-dose radiation of longitudinal whole-body μCT protocols on metastasis inflammation and fibrosis as well as host responses in murine models of lung disease. We aimed to establish high-quality generic μCT protocols that ensure safe repeated high-resolution μCT evaluation not interfering with animal health, the radiosensitive blood cell compartment and host response or the disease processes under investigation.

Materials and methods

Animals

Mice were kept in individually ventilated cages or filter top cages with free access to food and water in a conventional animal facility. The syngeneic mouse model of lung metastasis was induced by tail vein injection of cells from the squamous cell carcinoma (SCC) lung cancer cell line KLN205 (10^5 cells in 200 µl PBS) in 8-week-old female DBA/2 mice (Envigo, Venray, The Netherlands) under transient isoflurane (2% in oxygen) gas anaesthesia [100]. For the bleomycin-induced lung inflammation and fibrosis model, 8-week-old male C57Bl/6 mice (Janvier, Le Genest, France) were anesthetised with a mixture of ketamin (Nimatek 10 mg/ml, Europet, Gemert-Bakel, The Netherlands) and xylazine (2% Xyl-M 1 mg/ml, VMD, Arendonk, Belgium). Via tracheotomy (intratracheal instillation), 50 µL of Bleomycin (0.04 U or 0.05 U, Sanofi-Aventis, Diegem, Belgium) or vehicle phosphate buffered saline (PBS, Lonza, Basel, Switzerland) for sham controls was instilled [75,89]. Mouse body weights were recorded at baseline and at least once weekly until sacrifice. For experiments conducted with healthy animals, 8-week-old female DBA/2 or male C57Bl/6 mice (Janvier, Le Genest, France) were used. An overview of the number of animals per experimental group can be found in the experimental set-up (Figure 1). European, national and institutional guidelines for animal welfare and experimental conduct were followed (The KU Leuven Ethical Committee for animal research approved all experiments: p039/2014, p037/2017 and p227/2013).

Bioluminescence imaging

For BLI and quantification of lung metastasis burden, an IVIS Spectrum system (CaliperLS; Perkin-Elmer, Hopkinton, MA, USA) was used with software provided by the manufacturer (Living Image version 4.4.17504). D-luciferin (in PBS, 126 mg/kg) was injected intraperitoneally, acquisition of consecutive frames was started immediately thereafter until maximum signal intensity was reached, measured as photon flux per second through a region of interest (2.9 cm x 1.8 cm) covering the lungs. Image acquisition numbers and times varied between 10 and 15 frames of 30-60s each, depending on optimal acquisition settings as a function of signal intensity intrinsic to lung metastasis grade.

Micro-computed tomography

Mice were anesthetized by isoflurane (1.5-2% in oxygen, Piramal Healthycare, Morpeth, Northumberlang, United Kingdom) and scanned in supine position using *in vivo* µCT (Skyscan1278, Bruker micro-CT, Kontich, Belgium) with following parameters: 50 kVp X-ray source voltage, 918 µA current, 1 mm aluminium X-ray filter, 55 ms exposure time per projection, acquiring projections with 0.9° increments over a total 220° angle, 10 cm field of view covering the whole body producing reconstructed data sets with 50 µm isotropic voxel size either with ('4D protocol') or without

retrospective respiratory gating ('3D protocol'). For the 4D protocol (imaging dynamic processes over time), images were acquired in list mode, with nine projections per view, logged simultaneously with the breathing cycle of the mouse and retrospectively time-based sorted, resulting in four reconstructed 3D data sets corresponding to four different breathing cycle phases (4D) (end-inspiratory, end-expiratory and two intermediate phases). 3D datasets were acquired without respiratory gating using similar settings as above, acquiring and averaging three projections per view.

Software provided by the manufacturer (TSort, NRecon, DataViewer, and CTan) was used to retrospectively gate, reconstruct, visualize, and process μCT data [152]. For Hounsfield unit (HU) calibration, a phantom of an air-filled 1.5 mL tube inside a water-filled 50 mL tube was scanned. Based on full stack histograms of a volume-of-interest (VOI) containing only water or air, the main grayscale index of water (93) set at 0 HU and grayscale index of air (0) at -1000 HU. Quantification of mean lung density (in HU), non-aerated lung volume, aerated lung volume, and total lung volume was carried out for a VOI covering the lung, comprising of regions of interest that were manually delineated on the coronal μCT images, thereby avoiding heart and main blood vessels. The threshold to distinguish aerated from non-aerated lung tissue volume, manually set at -287.5 HU, was kept constant for all data sets.

Dosimetry

The radiation dose of an *in vivo* μCT scan was experimentally assessed with (1) an ionization chamber (IC), (2) an optical fiber radioluminescence (RL) probe and (3) thermoluminescent detectors (TLDs) in a mouse phantom. A Farmer-type ionization chamber FC65-G (IBA, Schwarzenbruck, Germany) was positioned in air at the centre of the gantry, only supported by a piece of tape placed on the top of the examination bed. Ten MCP-N thermoluminescent detectors (TLD) (LiF:Mg, Cu, P material, Institute of Nuclear Physics, Krakow, Poland), were inserted in as many dedicated cavities in the centre of a cylindrical polymethyl methacrylate phantom (100 mm long, 20 mm diameter). The phantom was positioned at the centre of the gantry on the examination bed. Reported dose is the average over the 10 positions. The optical fiber radioluminescence (RL) probe was inserted in the centre of a dedicated cylindrical polymethyl methacrylate phantom (100 mm long, 20 mm diameter); position of the phantom in the gantry was identical to the position of the TLD phantom. The ionization chamber was calibrated free in air in a RQR3* reference field [153] at the second-standard calibration laboratory of the Belgian Nuclear Research Centre (Mol, Belgium). The TLDs and the RL probe were calibrated in air against the ionization chamber using the LD3 beam quality.

µCT image quality

Contrast-to-noise ratio (CNR) and signal-to-noise ratio (SNR) are based on the average pixel value of the heart and calculated according to the following equations:

$$CNR = \frac{|S_{heart} - S_{bg}|}{\sigma_{bg}}$$

$$SNR = \frac{S_{heart}}{\sigma_{bg}}$$

S = signal; bg = background

Blood cell counts

Blood obtained by cardiac puncture at sacrifice, mixed with sodium citrate 3.8%, was analysed using a Cell-dyn 3700 (Abbott, Illinois, USA). Supplementary tables S1-S5 show all analysed parameters.

Histopathology

Formalin-fixed and paraffin-embedded lung sections were stained with haematoxylin-eosin. Pulmonary fibrosis was scored using the semi-quantitative Ashcroft score [76]. Collagen content was assessed by hydroxyproline quantification on the right lung lobes (experiment 2), as previously described [154].

Statistical analysis

All measurements are reported as individual value, mean and 95% confidence intervals (CI). Data were analysed using GraphPad Prism 7.0a (Graphpad Software Inc, San Diego, CA). Based on prior work and the nature of the biological data a normal distribution was assumed. Residuals and QQ graphs were used for visual assessment of the distribution. Where of interest, groups were compared by t-test or one-way ANOVA with Bonferroni corrected multiple comparisons. Resulting differences between the means are reported with 95% confidence intervals and exact p-values.
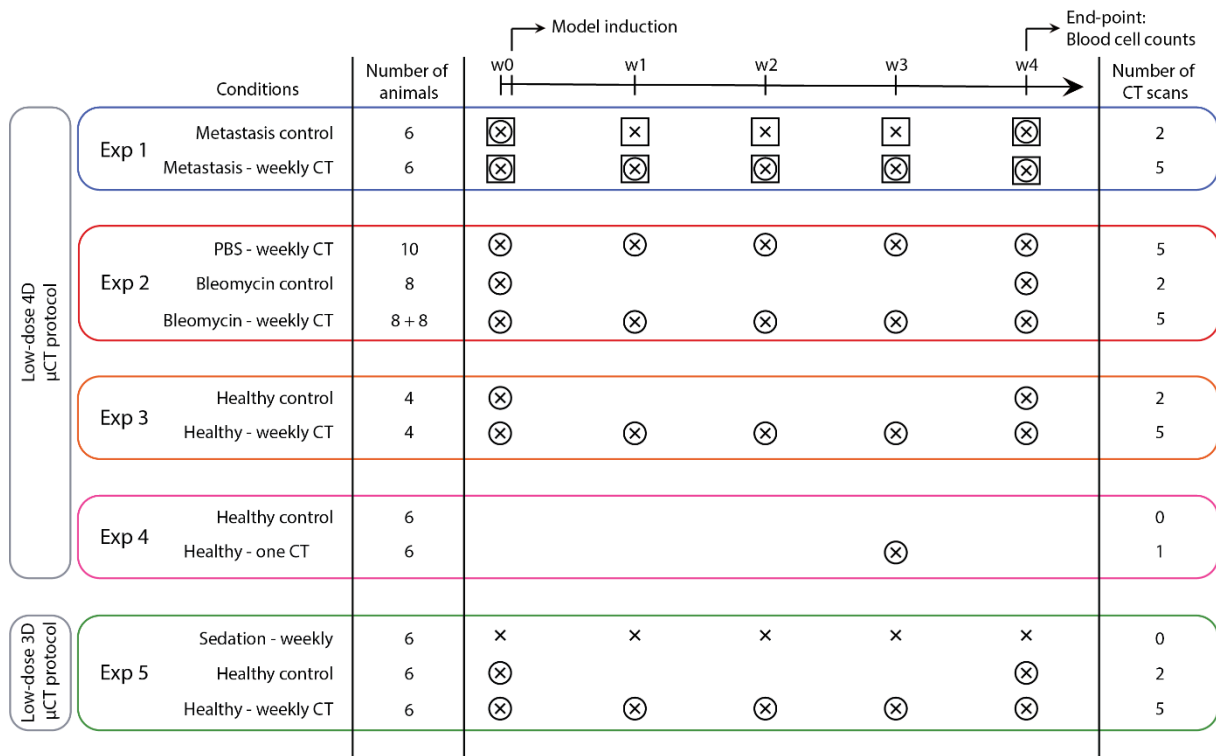
Figure 1: experimental set-up.
This scheme summarizes isoflurane sedation, number and timing of BLI and µCT scans, model induction and number of animals in each experimental group. **Experiment 1** compares mice with lung metastasis (DBA/2 strain) that underwent µCT-scans at baseline and weekly after metastasis induction for 4 weeks, with a metastasis group that was scanned with µCT only at baseline and endpoint. The lung metastasis burden in both groups was monitored with weekly BLI scans. **Experiment 2** compares bleomycin- (8 mice with 0.04U and 8 mice with 0.05U bleomycin) and sham-instilled mice (5 + 5 mice) of the C57Bl/6 strain that were weekly µCT-scanned with a bleomycin control group (8 mice) that was only scanned at baseline and endpoint. **Experiment 3** focuses on the effect of weekly µCT scans without the presence of disease. Analogous to experiment 1, healthy DBA/2 mice received either only a µCT scan at the beginning and at the end of the experiment or weekly scans for the entire experiment duration. In **experiment 4,** mice (C57Bl/6 strain) scanned once are compared for delayed effects after one week with mice receiving zero scans. **Experiment 5** investigates the potential effect of the low-dose 3D µCT protocol after 5 weekly µCT scans compared to one scan at the beginning and one at the end. A third control group was included that was sedated with isoflurane and handled as all other mice but did not receive any µCT scans. (x = isoflurane, ○ = µCT scan, □ = BLI scan)

Results

Repetitive 4D µCT in a lung metastasis model

We investigated the potential effects of whole-body x-ray exposure from repeated µCT on lung metastasis disease in a syngeneic model of rapidly dividing cells. One group with induced lung metastasis was scanned at baseline and weekly for 4 weeks, the second group was scanned at baseline and endpoint only (Figure 1). 4D µCT-scanning with retrospective respiratory-gating allowed acquisition of high-quality images and functional data corresponding with inspiration and expiration. No differences due to repeated µCT were found in body weight, tumour load measured by BLI, nor in µCT read-outs for metastatic burden and host response (Figure 2 A-C). Next, we assessed the effects on the radiosensitive blood cell compartment, analysing the circulating blood cells (supplementary table S1, Figure 2D). Weekly scanned mice showed a decreased platelet count (mean -251.2 * 10^3 cells/µL; 95% CI: -327.4 to -175.0) and absolute white blood cell number (mean -0.4262 * 103 cells/µL; 95% CI: -0.7740 to -0.0783), attributed to a decrease in absolute number of circulating lymphocytes (mean -0.2892 * 103 cells/µL; 95% CI: -0.4435 to -0.1349). Furthermore, eosinophils were decreased (mean -0.0125 * 103 cells/µL; 95% CI: -0.0185 to -0.0065), whereas number of neutrophils and red blood cells remained unaffected. In conclusion, repetitive 4D µCT-scanning influenced circulating blood cells in a lung metastasis model without clinical effects or change in disease outcomes.

Experiment 1: lung metastasis
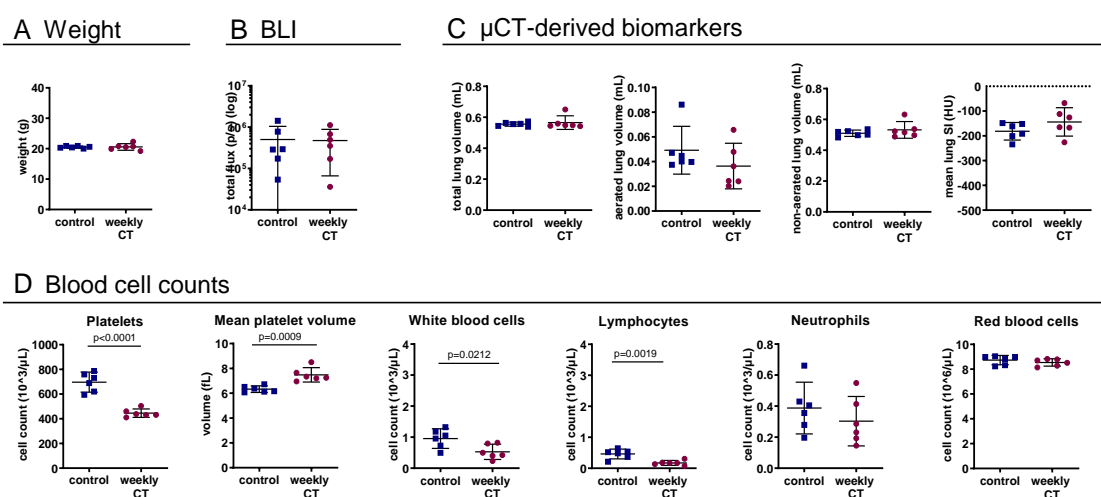
Figure 2: weekly low-dose 4D µCT does not influence the general health and disease outcomes but induces a sub-clinical decrease in white blood cell and platelet counts in a murine metastasis model.

Experiment 1: weekly-low dose 4D µCT scanning of metastasis-bearing mice induces a decrease in circulating platelets, increase in mean platelet volume, decrease in red blood cells and absolute white blood cell count, due to a decrease in number of lymphocytes. **(A)** Mouse body weight at end point. **(B)** *In vivo* BLI signal intensity expressed as total flux (p/s) from the lung, measuring metastatic load. **(C)** µCT-derived biomarkers (total lung volume, aerated lung volume, non-aerated lung volume and mean lung density). **(D)** Selected blood cell parameters: absolute platelet cell count, mean platelet volume, white blood cell count, lymphocyte count and neutrophil count and red blood cell count. Data are presented as individual values, group mean and 95% confidence intervals. P-values are presented in the graph when p < 0.05. HU, Hounsfield units.

Repetitive 4D μCT in a lung inflammation and fibrosis model

Next, repeated low-dose radiation was evaluated in a model involving endogenous rapidly dividing cells: bleomycin-induced lung fibrosis. Mice instilled with PBS or bleomycin were scanned at baseline and weekly for 4 weeks and compared with bleomycin-instilled controls only scanned at baseline and endpoint (Figure 1).

Due to high mortality in the bleomycin groups (2 mice of 8 (weekly CT) and 3 of 8 (control) reached the endpoint), our analysis was underpowered. Therefore, we included data of an experiment with the same set-up, except that mice were instilled with a reduced dose of bleomycin (0.04 U instead of 0.05 U). All mice were weekly scanned (Figure 3 in grey). 3 out of the 8 mice instilled with bleomycin reached the endpoint in this second cohort.

Similar to the lung metastasis model, platelet counts were decreased (mean -182.7 * 10^3 cells/μL; 95% CI: -333.8 to -31.62) in the weekly scanned bleomycin group compared to control bleomycin group (Figure 3E, supplementary table S2). Absolute white blood cell number was lower (mean -2.805 * 10^3 cells/μL; 95% CI: -3.277 to -2.334), with less circulating lymphocytes (mean -2.619 * 10^3 cells/μL; 95% CI: -2.936 to -2.301). Red blood cell numbers were also decreased (mean -1.072 * 10^6 cells/μL; 95% CI: -1.658 to -0.4862). Platelet counts for PBS-instilled weekly scanned mice were similarly decreased (mean -181.9 * 10^3 cells/μL; 95% CI: -318.1 to -45.72) and absolute white blood cells (mean -3.064 * 10^3 cells/μL 95% CI: -3.489 to -2.639) (attributed to a decrease in lymphocytes (mean -2.776 * 10^3 cells/μL; 95% CI: -3.062 to -2.490)) and less red blood cells (mean -1.586 * 10^6 cells/μL 95% CI: -2.114 to -1.058) were found.

Although the analysis of differences in disease severity between the bleomycin control and weekly scanned mice remained underpowered, no changes were found between these groups concerning body weight and our data indicate no clear influence from repeated scanning on mortality or pathology (extent of lung inflammation and fibrosis, assessed by histology, collagen content and μCT read-outs (Figure 3A-D)). PBS-instilled control mice were unaffected by radiation as evaluated by histology and μCT.

In conclusion, repetitive 4D μCT-scanning lowered circulating blood cells, irrespective of disease status.

Experiment 2: lung inflammation and fibrosis
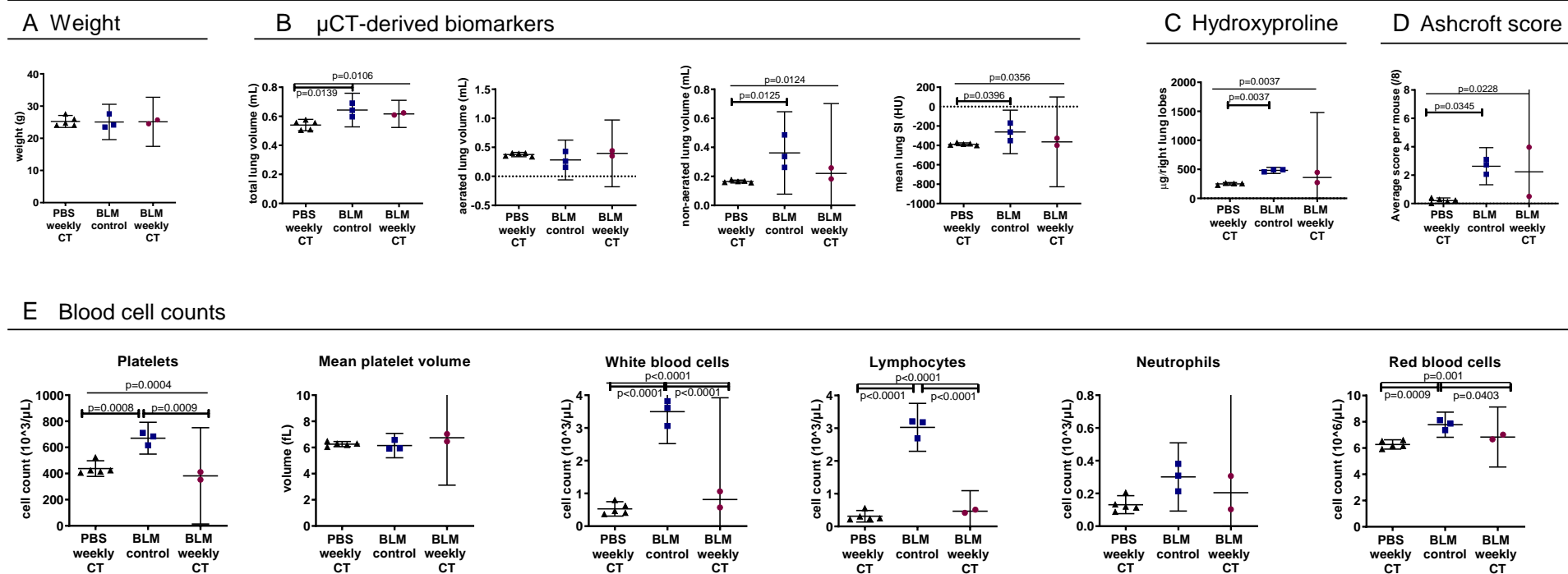
Figure 3: weekly low-dose 4D μCT alters blood cell counts in a bleomycin-induced mouse model.

Experiment 2: weekly-repeated 4D μCT scanning of bleomycin induced mice results in a decrease in platelets, red blood cells and a decrease in white blood cells, attributed to decreased lymphocyte counts. **(A)** Mouse body weight at end point **(B)** μCT-derived biomarkers reflecting disease progression of pulmonary fibrosis at endpoint (total lung volume, aerated lung volume, non-aerated lung volume and mean lung signal density). **(C)** collagen content as measured by hydroxyproline quantification of the right lung lobes and **(D)** Ashcroft score of extent of fibrosis of the left lung lobes **(E)** selected blood cell counts: absolute platelet cell count, mean platelet volume, white blood cell count, lymphocyte count and neutrophil count and red blood cell count. Data presented as individual values, group mean and 95% confidence intervals. Grey points represent mice instilled with 0.04 U of bleomycin, other points with 0.05 U. P-values and p-adjusted values are presented in the graph when p < 0.05. HU, Hounsfield unit.

Repeated 4D µCT in healthy mice

To further elucidate the contribution of disease status to the effects of repeated µCT, we investigated healthy mice. One group was scanned with the weekly regime (n = 4) and the other only at beginning and endpoint (n = 4). No differences were found concerning general health and lung µCT read-outs (Figure 4A). Similar to the findings in the two disease models, a decrease in platelets (mean -387.9 * 10^3 cells/µL; 95% CI: -521.6 to -254.3) and white blood cells (mean -0.3510 * 10^3 cells/µL; 95% CI: -0.6859 to -0.01608) (attributed to a decrease in lymphocytes (mean -0.02849 * 10^3 cells/µL; 95% CI: -0.5149 to -0.05496)) and a decrease in red blood cells (mean -1.832 * 10^6 cells/µL; 95% CI: -3.637 to -0.02679) was found in the weekly scanned healthy mice compared to controls (Figure 4B, supplementary table S3). These results confirm the effect of repeated low-dose 4D µCT-scanning on circulating blood cells, irrespective of disease or inflammatory status.

Experiment 3: healthy

A µCT-derived biomarkers
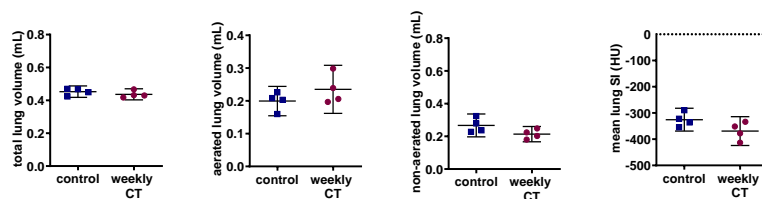
B Blood cell counts
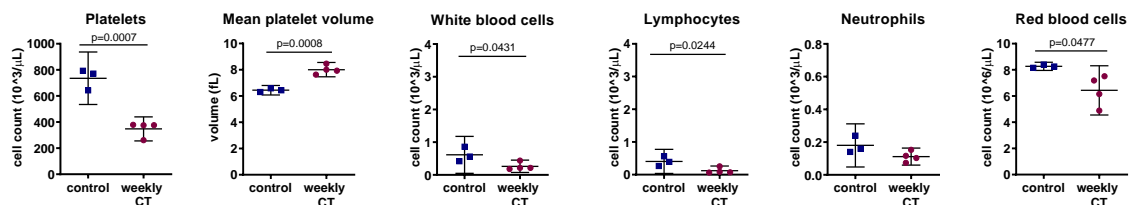
Figure 4: weekly low-dose 4D µCT does not influence the general health and disease outcomes but induces a decrease in blood cell counts of healthy mice.

Experiment 3: weekly-low dose 4D µCT scanning of healthy mice induces a decrease in platelets, increase in mean platelet volume, decrease in red blood cells and white blood cells, attributed to decreased lymphocyte counts. **(A)** µCT-derived biomarkers show no differences in healthy mice at endpoint (total lung volume, aerated lung volume, non-aerated lung volume and mean lung density). **(B)** Blood cell counts: absolute platelet cell count, mean platelet volume, white blood cell count, lymphocyte count and neutrophil count and red blood cell count. Data presented as individual values, group median and 95% confidence intervals. P- values are presented in the graph when p < 0.05. HU, Hounsfield unit.

To exclude that lower blood cell counts were a delayed effect of the second last scan, we compared blood cell counts of mice receiving a single scan a week before sacrifice (n = 6), and mice receiving no scan at all (n = 6). No significant differences were found for platelets, white blood cells and lymphocytes (Figure 5, supplementary table S4), indicating the observed effects in the previous experiments were indeed related to repeated exposure.

Experiment 4: healthy
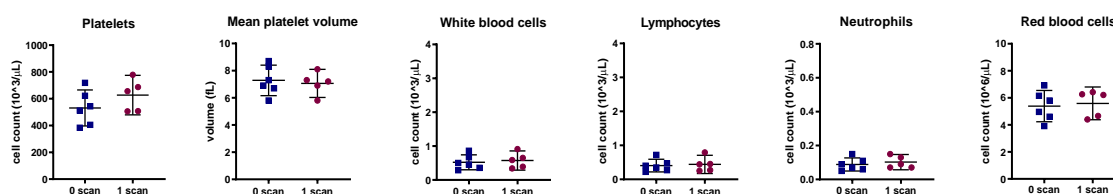
Figure 5: a low-dose 4D μCT scan does not affect blood cell counts one week after scanning.
Experiment 4: No differences are found in circulating blood cell counts between healthy control and scanned mice at endpoint, i.e. 1 week after the scan. Data presented as individual values, group mean and 95% confidence intervals. P-values are presented in the graph when p<0.05.

To isolate effects of repetitive x-ray exposure from potential influence of stress and anaesthesia associated with μCT, we included an additional healthy control group subjected to weekly anaesthesia and handling without μCT. This group showed no differences in blood cell counts (Figure 6C), further confirming that blood cell count effects can be attributed to repeated x-ray exposure.

Experiment 5: healthy
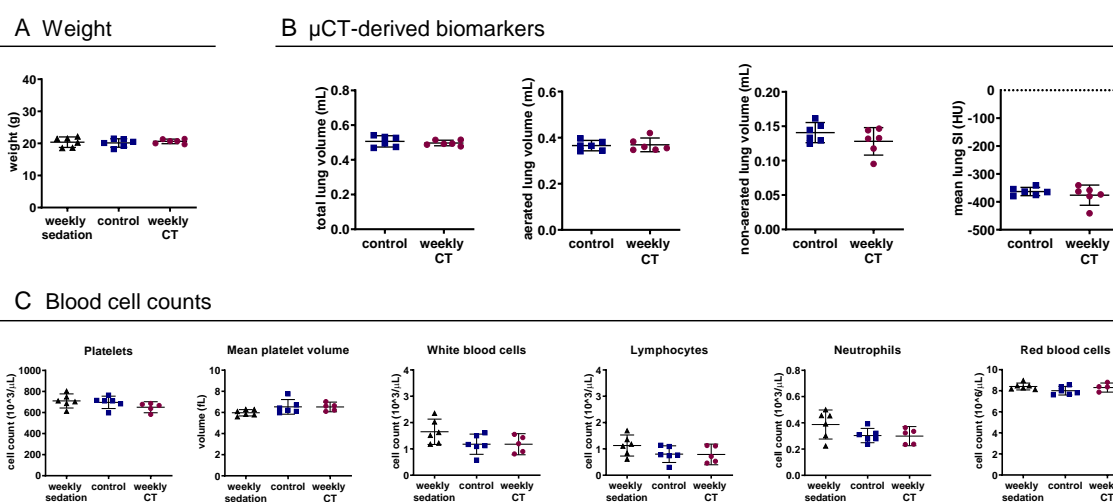
Figure 6: weekly low-dose 3D μCT is devoid of any effects on health, lung readouts and circulating blood cell counts.
Experiment 5 compares healthy mice scanned weekly or only at baseline and endpoint, and mice that underwent weekly isoflurane anaesthetics and handling without undergoing any μCT scans to isolate a potential effect from stress and anaesthesia from an effect of the x-ray dose associated with a μCT scan (weekly sedation). (A) Mouse body weight at end point. (B) μCT-derived biomarkers show no difference at endpoint (total lung volume, aerated lung volume, non-aerated lung volume and mean lung density) between the healthy control and healthy weekly scanned group. (C) selected blood cell counts: weekly low-dose 3D μCT scanning or weekly isoflurane sedation does not change the platelet, white blood cell or red blood cell counts. Data presented as individual values, group mean and 95% confidence intervals. P-values and p-adjusted values are presented in the graph when p<0.05.

Repeated 4D µCT: image quality and circulating blood cells

To eliminate effects on blood cells, while retaining high-quality images, we optimized a 3D protocol with expiration-weighted gating but without the possibility to acquire functional data. Scan time and dose were hereby much reduced compared to retrospective respiratory-gated 4D µCT. For accurate dosimetry, we used three different methods (Table 1). Radiation dose of a single µCT scan with the 3D versus 4D protocol ranged between 180-233 mGy versus 540-699 mGy respectively.

	Low-dose 4D µCT protocol	Low-dose 3D µCT protocol
IC in air	540 mGy	180 mGy
TLDs in phantom	699 mGy	233 mGy
RL probe in phantom	585 mGy	195 mGy

Table 1: dose measurements for the low-dose 4D and 3D µCT protocols.
Dose measurements were performed with ionization chamber (IC) in air, thermoluminescent detectors (TLDs) in mouse phantom and optical fiber radioluminescence (RL) probe in mouse phantom as specified in materials and methods.

Our 3D expiration-weighted strategy did not introduce any movement artefacts compared to respiratory-gated 4D scans. Analysis of signal-to-noise (SNR), contrast-to-noise ratio (CNR) and visual inspection confirmed equally high image quality (Figure 7) (a mean SNR of 26.9 and 25.65 and a mean CNR of 26.13 and 24.76 for 4D and 3D protocols, respectively, defined by the Rose criterion [155,156].
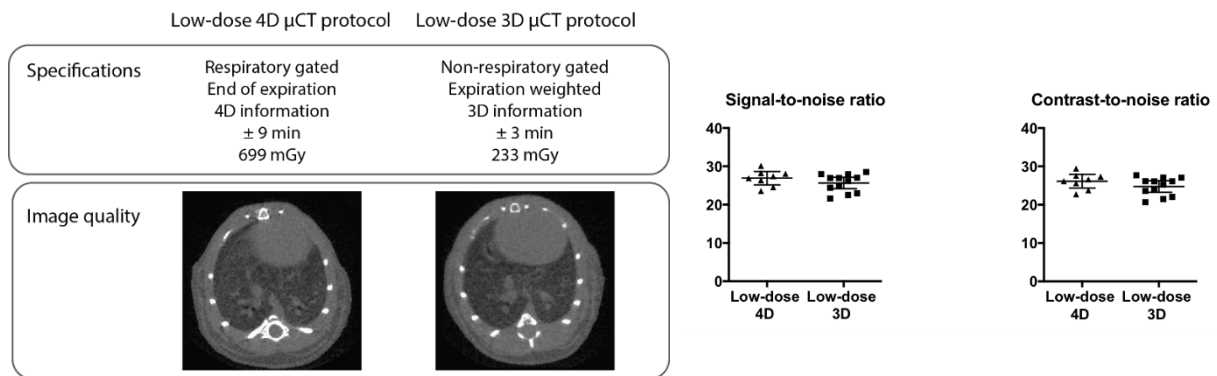
Figure 7: low-dose expiration-weighted 3D µCT yields equally high image quality as a 4D respiratory-gated protocol.
(A) Specifications of the 3D and 4D imaging protocols compared with representative reconstructed tomographic images at the level of lung and heart for both protocols, along with graphs of (B) signal-to-noise ratio and contrast-to-noise ratio compared for the respiratory-gated 4D (n = 8) and the expiration-weighted 3D µCT protocol (n = 12). Data presented as individual values, group mean and 95% confidence intervals.

In healthy mice, weekly 3D µCT did not affect body weight, µCT-derived lung biomarkers nor blood cell counts (Figure 6A-C, supplementary table S5): platelet numbers, white blood cells (lymphocytes as well as neutrophils) and red blood cells in weekly scanned healthy mice were not affected. In conclusion, repeated low-dose 3D µCT has no radiation effects on lungs or blood cells, while maintaining high image quality even for lung imaging in free-breathing mice.

Discussion

We investigated radiation dose and effects of repetitive whole-body µCT in different murine lung disease models and healthy mice, using a longitudinal imaging set-up typical for preclinical *in vivo* experiments: baseline scan, 4 weekly µCT scans for disease progression and sacrifice after last scan for *ex vivo* read-outs. Using a low-dose 4D retrospective respiratory-gating protocol, we observed no effects of repetitive scanning on disease outcomes in mice with lung metastasis, lung inflammation and fibrosis or healthy mice, but detected a decrease in circulating blood platelets and lymphocytes. With a 3D expiration-weighted scanning protocol, reducing the radiation dose by two thirds, this effect could be eliminated whilst retaining equally high imaging quality.

We analysed both healthy and diseased DBA/2 and C57Bl/6 mice, commonly utilized strains in preclinical pulmonary research. As we used immunocompetent mice, we can conclude that µCT has the potential to study disease processes where host response is an important factor, with C57Bl/6 mice in particular susceptible to lung fibrosis [157]. As we did not observe nor quantify an effect of radiation after weekly 4D µCT in healthy animals, our results are in line with previous studies reporting the absence of radiation-induced lung or cardiac damage in healthy mice scanned weekly for 5 to 12 weeks [127,150]. Furthermore, we assessed different lung disease models involving rapidly dividing exogenous and endogenous cells in immunocompetent mice. Repetitive µCT had no influence on disease progression in mice with progressing lung metastases. In mice with lung inflammation and fibrosis, our data also indicate no clear influence from repeated scanning on fibrosis, although this experiment was underpowered. Repeated low-dose 4D µCT can therefore be considered safe for the animal and disease process under investigation, even when involving rapidly dividing cells, but we continue to recommend the use of a similarly radiation exposed control group.

We next investigated whether repeated low-dose x-ray exposure may still have subtle effects on more radiosensitive processes by analysing circulating blood cells since the hematopoietic system and lymphocytes in particular are very sensitive to radiotoxicity [158,159]. In repetitively scanned mice, we observed less (but larger) circulating platelet and lymphocytes, neutrophils remained unaffected. Red blood cell numbers were lowered in repetitively scanned healthy and bleomycin-induced C57BL/6 mice, but not in DBA/2 mice with or without metastasis. The lower platelet and lymphocyte counts after repeated radiation in mice with lung metastasis, fibrosis and in healthy mice, points to disease-independent effect of the cumulative radiation dose. The decrease in platelets is likely sub-clinical, since we detected no bleeding problems. Also a murine platelet reduction up to 70% is reported not to result in clinical effects [160]. Defining values of clinically significant lymphopenia is more difficult, given the high variability in reported murine reference values [161]. The lymphocyte reduction could be

sub-clinical, not affecting the immune system, given the absence of infections or a correlation with disease outcomes in our study. Yet, we cannot formally exclude minimal effects on immune system functionality. Importantly, we nevertheless saw no influence of the decreased platelets and lymphocytes on the studied disease processes.

We examined blood cell counts immediately after the last scan (typical set-up of last scan followed by sacrifice and *ex vivo* work-up). Therefore, results reflect the short-term effect of cumulated radiation from weekly repeated μCT scans, no conclusions can be drawn on long-term effects and potential recuperation with time. Noteworthy, blood cell changes were not an effect of the last scan, since control groups received the same endpoint scan. No changes were seen one week after a single scan, ruling out delayed effects of the second-last scan. Moreover, no differences in circulating blood cells were observed comparing μCT-scanned healthy mice to controls that were sedated but never scanned. Therefore, we conclude that effects result from the cumulative radiation exposure.

To design longitudinal μCT protocols without radiotoxicity and still considering breathing movement corrections, we developed a respiration-weighted 3D protocol. This could lower the radiation dose per scan with two-thirds while maintaining the same lung image quality as the 4D protocol, with no increased movement artefacts, but without the possibility to extract functional lung read-outs (e.g. tidal volume, readouts at inspiration). This 3D protocol is nevertheless useful for most studies, where volume data from inspiratory phase are not needed. With this 3D protocol, we could eliminate all previously found radiation effects on blood cell counts, thereby offering a generically applicable longitudinal μCT protocol with demonstrated safety for the animal and (patho-)physiological processes under investigation. Our results further expand knowledge about maximum acceptable repeated dose exposure, as previous reports found no blood cell count changes in C57Bl/6 mice scanned less frequently (every other week for 3 times) [162], as well as in mice scanned more frequently (3 times/week for 4 weeks) [163], but with markedly lower radiation doses than our 3D protocol (reported dose 16.19 mGy measured at phantom center versus 180-233 mGy dose).

Indispensable in guarding over radiation exposure is awareness of dose exposure and hence accurate dosimetry. As currently no standard operating procedures exist for preclinical μCT dosimetry, we measured radiation dose of our 4D and 3D μCT protocols by three different methods: IC in air, in-phantom TLDs and an in-phantom RL probe. The doses measured in-phantom were higher compared to in-air, as expected due to the contribution of scattered x-rays. The IC is the reference and used for calibration of TLDs and RL probe. Nevertheless, size limits its use in μCT, since its dimensions do not enable complete dose profile measurements and the closed lead shielding may hamper insertion of an IC in the field-of-view during scanning. Moreover, the interest of using such IC combined with a mouse

phantom is limited in contrast with conventional CT in the clinical context where the dimensions of the IC are negligible compared to those of the CT Dose Index phantoms. TLDs are a practical alternative. Although their energy response is not as good as the IC, they are made of tissue-equivalent material and small enough to be inserted in-phantom. An inherent limitation of TLDs is they do not allow real-time dosimetry, needed during preclinical *in vivo* scan parameter optimization. Compared to TLDs, the RL probe results are subject to higher uncertainty because of the higher energy dependence of the RL material. Nevertheless, the advantages for μCT are its small size and capacity to perform online and real-time measurements, useful for scan protocol optimization.

To summarize, it is necessary and within our potential to design high-quality and safe μCT protocols, regarding the murine health status, disease process and host responses under investigation. We have established an upper dose limit to be delivered with repeated μCT scanning: a dose of 540-699 mGy delivered weekly for 5 times, can be considered as physiologically safe with a sub-clinical drop in circulating blood cell counts, while a dose of 180-233 mGy per single scan delivered under the same longitudinal regime is safe in absolute terms. More specifically, our results indicate the possibility to design high-resolution μCT protocols without influence on the most radiosensitive processes in the body, thereby ideal to study (lung) disease processes and host responses in rodent models.

Acknowledgements

Author contribution

G.V.V. conceived the study; N.B., K.D., J.D., E.D.L., R.B., M.H., R.L. and G.V.V. designed the experiments. N.B., K.D., E.M., J.D., A.H., J.W., J.D., T.V., E.T., M.L., R.B and G.V.V. performed the experiments. N.B., K.D., J.D., T.V. and E.T. analyzed the data. M.H., E.D.L., R.L. and G.V.V. supervised the experiments and data analysis. N.B. and K.D. wrote the manuscript. J.V., R.L. and G.V.V. reviewed the manuscript. All authors have read and approved the final manuscript.

Conflict of interest

All authors declare no conflict of interest.

Supplementary information

	Exp1 - lung metastasis						
	Metastasis control		Metastasis weekly CT				
	mean	95% CI	mean	95% CI	p-value	mean difference	95% CI
WBC (10³/µL)	0.9548	0.6381 to 1.272	0.5287	0.2823 to 0.7751	**0.0212**	**-0.4262**	-0.7740 to -0.0783
NEU (10³/µL)	0.3878	0.2210 to 0.5547	0.3032	0.1440 to 0.4624	0.3675	-0.0847	-0.2845 to 0.1152
NEU%	40.03	34.74 to 45.33	57.15	48.85 to 65.45	**0.0012**	**17.12**	8.579 to 25.65
LYM (10³/µL)	0.4602	0.3009 to 0.6194	0.1710	0.0091 to 0.2506	**0.0019**	**-0.2892**	-0.4435 to -0.1349
LYM%	48.27	40.72 to 55.81	33.58	24.6 to 42.57	**0.0092**	**-14.68**	-24.85 to -4.512
MONO (10³/µL)	0.0633	0.0393 to 0.0873	0.0355	0.0093 to 0.0617	0.0719	-0.0278	-0.0587 to 0.0030
MONO%	7,118	3.856 to 10.38	6,148	2.655 to 9.642	0.6133	-0.97	-5.114 to 3.174
EOS (10³/µL)	0.0162	0.0095 to 0.0228	0.0037	0.0017 to 0.0056	**0.0009**	**-0.0125**	-0.0185 to -0.0065
EOS%	1,677	1.175 to 2.178	0.6867	0.398 to 0.9753	**0.0013**	**-0.99**	-1.492 to -0.4883
BASO (10³/µL)	0.0272	0.0166 to 0.0377	0.0152	0.0008 to 0.0296	0.1146	-0.012	-0.0275 to 0.0003
BASO%	2.922	2.112 to 3.731	2,439	0.503 to 4.375	0.5676	-0.4825	-2.302 to 1.337
RBC (10⁶/µL)	8,728	8.351 to 9.106	8.54	8.245 to 8.835	0.3361	-0.1883	-0.6036 to 0.227
Hgb (g/dL)	11.78	11.25 to 12.31	11.68	11.32 to 12.05	0.6977	-0.1	-0.6573 to 0.4573
HCT%	64.6	61.61 to 67.59	64.45	62.37 to 66.53	0.9178	-0.15	-3.308 to 3.008
MCV (fL)	74	73.22 to 74.78	75.5	74.91 to 76.09	**0.0028**	**1.5**	0.6506 to 2.349
MCH (pg)	13.5	13.39 to 13.61	13.7	13.59 to 13.81	**0.0101**	**0.2**	0.0591 to 0.341
MCHC (g/dL)	18.25	18.19 to 18.31	18.13	18.02 to 18.24	**0.0346**	**-0.1167**	-0.2230 to -0.0103
RDW %CV	16.97	15.8 to 18.13	19.78	18.52 to 21.04	**0.0018**	**2,817**	1.331 to 4.303
PLT (10³/µL)	696.7	615.8 to 777.5	445.5	411.0 to 480	**<0.0001**	**-251.2**	-327.4 to -175.0
MPV (fL)	6,327	6.06 to 6.593	7,478	6.902 to 8.055	**0.0009**	**1,152**	0.6012 to 1.702
PCT %	0.4415	0.3804 to 0.5026	0.3328	0.3015 to 0.3642	**0.0022**	**-0.1087**	-0.1681 to -0.0492
PDW 10(GSD)	17.6	16.95 to 18.25	19.57	18.79 to 20.35	**0.0006**	**1,967**	1.087 to 2.846

Supplementary table S1: blood cell counts of control and weekly scanned mice with induced lung metastasis.
WBC=white blood cells; NEU=neutrophils; LYM=lymphocytes; MONO=monocytes; EOS=eosinophils; BASO=basophils; RBC=red blood cells; Hgb=hemoglobin; HCT=hematocrit; MCV=mean corpuscular (cell) volume; MCH=mean corpuscular hemoglobin; MCHC=mean corpuscular hemoglobin concentration; RDW=red cell distribution width; PLT=platelets; MPV=mean platelet volume; PCT=plateletcrit

	Exp2 - lung inflammation and fibrosis																
	PBS weekly CT		**Bleomycin control**		**Bleomycin weekly CT**			**PBS vs BLM CO**			**PBS vs BLM weekly CT**			**BLM CO vs BLM weekly CT**		
	mean	95% CI	mean	95% CI	mean	95% CI	p-value	p-adj value	mean difference	95% CI	p-adj value	mean difference	95% CI	p-adj value	mean difference	95% CI
WBC (10³/µL)	0.4327	0.3100 to 0.5554	3.497	2.522 to 4.472	0.6912	0.3573 to 1.025	**<0.0001**	**<0.0001**	-3.064	-3.489 to -2.639	0.2032	-0.2585	-0.6122 to 0.09520	**<0.0001**	2.805	2.334 to 3.277
NEU (10³/µL)	0.1118	0.07939 to 0.1442	0.3010	0.0927 to 0.5093	0.1758	0.04625 to 0.3054	**0.0038**	**0.0032**	-0.1892	-0.3155 to -0.06291	0.3650	-0.06400	-0.1691 to 0.04108	0.0882	0.1252	-0.01491 to 0.2653
NEU%	27.32	20.82 to 33.81	8.497	4.78 to 12.21	24.36	15.77 to 32.95	**0.0088**	**0.0076**	18.82	4.795 to 32.84	>0.9999	2.955	-8.713 to 14.62	**0.0450**	-15.86	-31.42 to -0.3057
LYM (10³/µL)	0.2507	0.1548 to 0.3466	3.030	2.298 to 3.762	0.4080	0.2619 to 0.5541	**<0.0001**	**<0.0001**	-2.779	-3.066 to -2.493	0.2864	-0.1573	-0.3954 to 0.08084	**<0.0001**	2.622	2.304 to 2.940
LYM%	56.19	47.03 to 65.35	86.67	81.13 to 92.20	61.12	44.78 to 77.46	**0.0057**	**0.0048**	-30.48	-51.85 to -9.108	>0.9999	-4.930	-22.71 to 12.85	**0.0328**	25.55	1.840 to 49.25
MONO (10³/µL)	0.0358	0.02376 to 0.04784	0.052	-0.0359 to 0.1399	0.0558	0.005798 to 0.1058	0.3861	>0.9999	-0.0162	-0.06538 to 0.03298	0.6231	-0.02	-0.06538 to 0.03298	>0.9999	-0.0038	-0.05836 to 0.05076
MONO%	8.718	5.723 to 11.71	1.461	-0.7380 to 3.659	7.620	3.116 to 12.12	**0.0325**	**0.0309**	7.257	0.5914 to 13.92	>0.9999	1.098	-4.448 to 6.644	0.1212	-6.159	-13.55 to 1.236
EOS (10³/µL)	0.0038	0.002262 to 0.005338	0.023	-0.0481 to 0.0941	0.008	0.0002957 to 0.0157	0.0573	0.0559	-0.01920	-0.03881 to 0.0004053	>0.9999	-0.0042	-0.02051 to 0.01211	0.2488	0.015	-0.00675 to 0.03675
EOS%	0.911	0.5863 to 1.236	0.7277	-1.667 to 3.122	1.11	0.3099 to 1.91	0.6761	>0.9999	0.1833	-0.8780 to 1.245	>0.9999	-0.1990	-1.082 to 0.6841	>0.9999	-0.3823	-1.560 to 0.7951
BASO (10³/µL)	0.0306	0.01754 to 0.04366	0.0943	0.0123 to 0.1764	0.1136	-0.08396 to 0.3112	0.1918	0.8053	-0.06373	-0.2131 to 0.08564	0.2766	-0.083	-0.2073 to 0.04129	>0.9999	-0.01927	-0.1850 to 0.1465
BASO%	6.862	4.804 to 8.920	2.653	1,016 to 4,290	5.798	2.152 to 9.444	0.0931	0.0962	4.209	-0.5899 to 9.007	>0.9999	1.064	-2.929 to 5.07	0.3972	-3.145	-8.468 to 2.179
RBC (10⁶/µL)	6.194	5.993 to 6.395	7.78	6,820 to 8,740	6.708	6.356 to 7.060	**<0.0001**	**<0.0001**	-1.586	-2.114 to -1.058	**0.0198**	-0.5140	-0.9533 to -0.07468	**0.0005**	1.072	0.4862 to 1.658
Hgb (g/dL)	9.625	9.323 to 9.927	11.3	10,80 to 11,80	10.25	9.528 to 10.98	0.0002	0.0001	-1.675	-2.475 to -0.8754	0.0670	-0.6290	-1.294 to 0.03628	**0.0188**	1.046	0.1590 to 1.933
HCT%	52.31	50.50 to 54.12	60.53	56.06 to 65.01	56.34	52.47 to 60.21	**0.0006**	**0.0007**	-8.223	-12.87 to -3.579	**0.0396**	-4.030	-7.894 to -0.1659	0.1336	4.193	-0.9588 to 9.346
MCV (fL)	84.49	83.74 to 85.24	77.77	73.81 to 81.73	77.77	73.81 to 81.73	**<0.0001**	<0.0001	6.723	4.582 to 8.864	>0.9999	0.5300	-1.251 to 2.311	**<0.0001**	-6.193	-8.569 to -3.818
MCH (pg)	15.55	15.36 to 15.74	14.57	13.39 to 15.74	15.26	14.97 to 15.55	**0.0006**	**0.0004**	0.9833	0.4566 to 1.510	0.2848	0.2900	-0.1483 to 0.7283	**0.0180**	-0.6933	-1.278 to -0.1089
MCHC (g/dL)	18.42	18.30 to 18.54	18.70	18.04 to 19.36	18.20	18.02 to 18.38	**0.0056**	0.0916	-0.2800	-0.5959 to 0.03588	0.1186	0.2200	-0.04283 to 0.4828	**0.0048**	0.5000	0.1496 to 0.8504
RDW %CV	19.74	18.64 to 20.84	17.53	17.15 to 17.91	19.44	16.64 to 22.24	0.1620	0.4863	2.207	-0.7422 to 5.156	>0.9999	0.3000	-2.154 to 2.754	0.4118	-1.907	-5.178 to 1.365
PLT (10³/µL)	488.4	440.1 to 536.7	670.3	548.7 to 791.9	487.6	359.3 to 615.9	**0.0070**	**0.0079**	-181.7	-318.1 to -45.72	>0.9999	0.8000	-112.5 to 114.1	**0.0159**	182.7	31.62 to 333.8
MPV (fL)	6.265	6.110 to 6.420	6.147	5.214 to 7.079	6.430	5.943 to 6.917	0.4116	>0.9999	0.1183	-0.4077 to 0.6444	0.9780	-0.1650	-0.6027 to 0.2727	0.6319	-0.2833	-0.8669 to 0.3003
PCT %	0.3061	0.2747 to 0.3375	0.4127	0.3048 to 0.5206	0.3114	0.2404 to 0.3824	**0.0118**	**0.0120**	-0.1066	-0.1912 to -0.02197	>0.9999	-0.0053	-0.07569 to 0.06509	**0.0325**	0.1013	0.007414 to 0.1951
PDW 10(GSD)	17.30	16.97 to 17.63	17.43	16.67 to 18.19	17.62	16.79 to 18.45	0.5342	>0.9999	-0.1333	-1.042 to 0.7749	0.8156	-0.3200	-1.076 to 0.4357	>0.9999	-0.1867	-1.194 to 0.8209

Supplementary table S2: blood cell counts of control and weekly µCT-scanned healthy and animals with bleomycin-induced lung inflammation and fibrosis.
WBC=white blood cells; NEU=neutrophils; LYM=lymphocytes; MONO=monocytes; EOS=eosinophils; BASO=basophils; RBC=red blood cells; Hgb=hemoglobin; HCT=hematocrit; MCV=mean corpuscular (cell) volume; MCH=mean corpuscular hemoglobin; MCHC=mean corpuscular hemoglobin concentration; RDW=red cell distribution width; PLT=platelets; MPV=mean platelet volume; PCT=plateletcrit

	Exp3 - healthy						
	Healthy control		**Healthy weekly CT**				
	mean	95% CI	mean	95% CI	p-value	mean difference	95% CI
WBC (10³/µL)	0.6140	0.04885 to 1.179	0.2630	0.07476 to 0.4512	**0.0431**	**-0.3510**	-0.6859 to -0.01608
NEU (10³/µL)	0.1800	0.04855 to 0.3114	0.1115	0.05936 to 0.1636	0.0858	-0.06850	-0.1510 to 0.01396
NEU%	29.93	21.78 to 38.08	44.30	30.89 to 57.71	**0.0405**	**14.37**	0.9147 to 27.82
LYM (10³/µL)	0.4057	0.03771 to 0.7736	0.1208	-0.02367 to 0.2652	**0.0244**	**-0.2849**	-0.5149 to -0.05496
LYM%	66.00	58.72 to 73.28	42.75	21.58 to 63.92	**0.0335**	**-23.25**	-43.81 to -2.695
MONO (10³/µL)	0.01733	-0.02720 to 0.06186	0.01550	0.008443 to 0.02256	0.8474	-0.001833	-0.02509 to 0.02142
MONO%	2.450	-1.817 to 6.717	6.635	2.084 to 11.19	0.0770	4.185	-0.6591 to 9.029
EOS (10³/µL)	0.001667	-0.002128 to 0.005461	0.007000	-0.007983 to 0.02198	0.3862	0.005333	-0.009112 to 0.01978
EOS%	0.3303	-0.2564 to 0.9170	3.114	-3.988 to 10.22	0.3404	2.784	-4.010 to 9.578
BASO (10³/µL)	0.009667	-0.02119 to 0.04053	0.008250	0.001836 to 0.01466	0.835	-0.001417	-0.01802 to 0.01518
BASO%	1.264	-1.915 to 4.444	3.190	2.242 to 4.138	**0.0425**	**1.926**	0.09624 to 3.755
RBC (10⁶/µL)	8.267	7.954 to 8.579	6.435	4.554 to 8.316	**0.0477**	**-1.832**	-3.637 to -0.02679
Hgb (g/dL)	11.07	10.44 to 11.69	8.678	6.238 to 11.12	**0.0476**	**-2.389**	-4.742 to -0.03664
HCT%	61.03	58.26 to 63.80	48.80	34.71 to 62.89	0.0678	-12.23	-25.77 to 1.305
MCV (fL)	73.87	71.99 to 75.75	75.90	74.91 to 76.89	**0.0112**	**2.033**	0.6998 to 3.367
MCH (pg)	13.40	12.65 to 14.15	13.50	13.16 to 13.84	0.6268	0.1000	-03967 to 0.5967
MCHC (g/dL)	18.17	17.65 to 18.68	17.78	17.23 to 18.32	0.1423	-0.3917	-0.9702 to 0.1869
RDW %CV	17.83	15.10 to 20.57	19.33	17.62 to 21.03	0.1309	1.492	-0.6327 to 3.616
PLT (10³/µL)	735.7	534.4 to 936.9	347.8	255.7 to 439.8	**0.0007**	**-387.9**	-521.6 to -254.3
MPV (fL)	6.443	6.083 to 6.804	8.005	7.459 to 8.551	**0.0008**	**1.562**	1.010 to 2.114
PCT %	0.4743	0.3252 to 0.6235	0.2770	0.2167 to 0.3373	**0.0030**	**-0.1973**	-0.2916 to -0.1031
PDW 10(GSD)	17.30	16.64 to 17.96	19.28	17.47 to 21.08	**0.0340**	**1.975**	0.2217 to 3.728

Supplementary table S3: blood cell counts of control and weekly µCT-scanned healthy animals.
WBC=white blood cells; NEU=neutrophils; LYM=lymphocytes; MONO=monocytes; EOS=eosinophils; BASO=basophils; RBC=red blood cells; Hgb=hemoglobin; HCT=hematocrit; MCV=mean corpuscular (cell) volume; MCH=mean corpuscular hemoglobin; MCHC=mean corpuscular hemoglobin concentration; RDW=red cell distribution width; PLT=platelets; MPV=mean platelet volume; PCT=plateletcrit

	Exp4 - healthy						
	Healthy control		**Healthy one CT**				
	mean	95% CI	mean	95% CI	p-value	mean difference	95% CI
WBC (10³/μL)	0.5217	0.3006 to 0.7427	0.5760	0.2932 to 0.8588	0.6908	-0.05433	-0.3535 to 0.2449
NEU (10³/μL)	0.08833	0.04940 to 0.1273	0.1020	0.05689 to 0.1471	0.5545	-0.01367	-0.06402 to 0.03669
NEU%	17.18	13.13 to 21.24	18.46	11.78 to 25.14	0.6575	-1.277	-7.576 to 5.023
LYM (10³/μL)	0.4050	0.2179 to 0.5921	0.4400	0.1711 to 0.789	0.775	-0.03500	-0.3038 to 0.2338
LYM%	77.35	72.84 to 81.86	74.7	65.54 to 83.86	0.4748	2.650	-5.388 to 10.69
MONO (10³/μL)	0.008333	0.004049 to 0.01262	0.01800	0.007611 to 0.02839	**0.0332**	**-0.009667**	-0.01837 to -0.0009632
MONO%	1.633	0.9012 to 2.365	3.360	0.1238 to 6.596	0.1504	-1.727	-4.211 to 0.7577
EOS (10³/μL)	0.01167	-0.0006017 to 0.02394	0.00800	-0.002389 to 0.01839	0.5727	0.003667	-0.01051 to 0.01784
EOS%	1.933	0.5688 to 3.298	1.800	-0.3524 to 3.952	0.8871	0.1333	-1.933 to 2.199
BASO (10³/μL)	0.003333	-0.002086 to -0.007106	0.00400	-0.007106 to 0.01511	0.8801	-0.0006667	-0.01039 to 0.009055
BASO%	0.6500	-0.2122 to 1.512	1.060	-0.5072 to 2.627	0.5315	-0.4100	-1.836 to 1.016
RBC (10⁶/μL)	5.390	4.232 to 6.548	5.590	4.379 to 6.801	0.7599	-0.2000	-1.636 to 1.236
Hgb (g/dL)	7.883	6.184 to 9.583	8.240	6.424 to 10.06	0.7130	-0.3567	-2.482 to 1.768
HCT%	25.25	18.89 to 31.61	27.04	20.48 to 33.60	0.6182	-1.790	-9.635 to 6.055
MCV (fL)	46.60	44.73 to 48.47	48.22	46.73 to 49.71	0.1189	-1.620	-3.746 to 0.5064
MCH (pg)	14.60	14.42 to 14.78	14.78	14.62 to 14.94	0.0823	-0.1800	0.3882 to 0.02824
MCHC (g/dL)	31.38	30.16 to 32.60	30.66	29.82 to 31.50	0.2528	0.7233	-0.6157 to 0.5919
RDW %CV	13.20	12.59 to 13.81	14.12	13.58 to 14.66	**0.0169**	**-0.9200**	-1.631 to -0.2085
PLT (10³/μL)	531.0	369.9 to 665.1	627.2	479.8 to 774.6	0.2315	-96.20	-265.8 to 73.41
MPV (fL)	7.283	6.160 to 8.407	7.060	6.026 to 8.094	0.7131	0.2233	-1.108 to 1.555
PCT %	0.3750	0.3139 to 0.4361	0.4440	0.3139 to 0.5741	0.1992	-0.06900	-0.1817 to 0.04365

Supplementary table S4: blood cell counts of control and healthy animals after a single μCT scan.
WBC=white blood cells; NEU=neutrophils; LYM=lymphocytes; MONO=monocytes; EOS=eosinophils; BASO=basophils; RBC=red blood cells; Hgb=hemoglobin; HCT=hematocrit; MCV=mean corpuscular (cell) volume; MCH=mean corpuscular hemoglobin; MCHC=mean corpuscular hemoglobin concentration; RDW=red cell distribution width; PLT=platelets; MPV=mean platelet volume; PCT=plateletcrit

| | Exp5 - healthy | | | | | | | | | | | | | | | |
| | Healthy weekly sedation | | Healthy control | | Healthy weekly CT | | | Healthy WS vs healthy CO | | | Healthy WS vs healthy weekly CT | | | Healthy CO vs healthy weekly CT | | |
	mean	95% CI	mean	95% CI	mean	95% CI	p-value	p-adj value	mean difference	95% CI	p-adj value	mean difference	95% CI	p-adj value	mean difference	95% CI
WBC (10^3/µL)	1.650	1.168 to 2.132	1.178	0.7948 to 1.1560	1.178	0.7774 to 1.578	0.0921	0.1642	-0.4725	-1.085 to 0.1401	0.1969	-0.4722	-1.115 to 0.1704	>0.9999	0.003000	-0.6423 to 0.6429
NEU (10^3/µL)	0.3870	0.2761 to 0.4979	0.3030	0.2480 to 0.3580	0.2988	0.2259 to 0.3717	0.1260	0.2407	0.3870	-0.2051 to 0.03706	0.2398	-0.08820	-0.2152 to 0.03877	>0.9999	-0.004200	-0.1312 to 0.1228
NEU%	24.03	17.46 to 30.60	27.42	19.84 to 35	26.68	17.23 to 36.13	0.6895	>0.9999	3.383	-7.622 to 14.39	>0.9999	2.647	-8.896 to 14.19	>0.9999	-0.7367	-12.28 to 10.81
LYM (10^3/µL)	1.127	0.7268 to 1.527	0.8027	0.4856 to 1.120	0.7896	0.3975 to 1.182	0.1900	0.3511	-0.3242	-0.8516 to 0.2033	0.3593	-0.3372	-0.8904 to 0.2159	>0.9999	-0.0131	-0.5662 to 0.5401
LYM%	67.40	58.08 to 76.72	66.42	58.63 to 74.20	65.46	52.40 to 78.52	0.9375	>0.9999	-0.9833	-14.97 to 13.00	>0.9999	-1.940	-16.61 to 21.73	>0.9999	-0.9567	-15.62 to 13.71
MONO (10^3/µL)	0.05650	0.02252 to 0.09048	0.03383	0.02111 to 0.04656	0.05200	0.005235 to 0.09876	0.3842	0.5852	-0.02267	-0.06793 to 0.02260	>0.9999	-0.004500	-0.05198 to 0.04298	0.9480	0.01817	-0.02931 to 0.06564
MONO%	3.641	1.177 to 6.105	2.955	2.204 to 3.706	4.710	0.4641 to 8.956	0.4820	>0.9999	-0.6858	-4.363 to 2.992	>0.9999	1.069	-2.788 to 4.926	0.7096	1.755	-2.102 to 5.612
EOS (10^3/µL)	0.02567	0.01723 to 0.03411	0.02117	0.009511 to 0.03282	0.01800	0.006860 to 0.02914	0.4246	>0.9999	-0.004500	-0.01940 to 0.01040	0.6110	-0.007667	-0.02329 to 0.007959	>0.9999	-0.003167	-0.01879 to 0.01246
EOS%	1.575	1.119 to 2.031	1.770	1.019 to 2.521	1.493	0.9352 to 2.050	0.6965	>0.9999	0.3204	-0.6755 to 1.066	>0.9999	-0.08220	-0.9955 to 0.8311	>0.9999	-0.2775	-1.191 to 0.6358
BASO (10^3/µL)	0.05383	0.03005 to 0.07762	0.02950	-0.001876 to 0.06088	0.01880	0.006004 to 0.03160	0.0627	0.2680	-0.02433	-0.06056 to 0.01189	0.0755	0.05383	-0.07303 to 0.002963	>0.9999	-0.01070	-0.04870 to 0.02730
BASO%	3.317	1.855 to 4.779	1.428	1.010 to 1.847	1.658	0.4805 to 2.835	**0.0117**	**0.0171**	**-1.888**	-3.463 to -0.3139	**0.0488**	**-1.659**	-3.310 to -0.007812	>0.9999	0.2293	-1.422 to 1.881
RBC (10^6/µL)	8.405	8.082 to 8.728	8.005	7.596 to 8.414	8.304	7.871 to 8.737	0.1603	0.2046	0.2990	-0.9502 to 0.1502	>0.9999	-0.1010	-0.6780 to 0.4760	0.5426	0.2990	-0.2780 to 0.8760
Hgb (g/dL)	11.15	10.66 to 11.64	10.68	10.10 to 11.27	10.80	9.588 to 12.00	0.5739	0.9591	-0.4667	-1.688 to 0.7547	>0.9999	-0.3533	-1.575 to 0.8681	>0.9999	0.1133	-1.108 to 1.335
HCT%	60.87	58.64 to 63.09	58.28	55.12 to 61.45	60.68	57.76 to 63.60	0.1877	0.2989	-2.583	-6.565 to 1.398	>0.9999	-0.1867	-4.362 to 3.989	0.4233	2.3970	-1.779 to 6.572
MCV (fL)	72.42	71.77 to 73.06	72.80	72.02 to 73.58	73.12	72.37 to 73.87	0.2431	0.9942	0.3833	-0.6521 to 1.419	0.3006	0.7033	-0.7660 to 1.406	>0.9999	0.3200	-0.7660 to 1.406
MCH (pg)	13.27	13.06 to 13.47	13.35	13.21 to 13.49	13.54	13.35 to 13.73	**0.0459**	>0.9999	0.08333	-0.1753 to 0.3420	**0.0480**	**0.2733**	0.002087 to 0.5446	0.2331	0.1900	-0.08125 to 0.4612
MCHC (g/dL)	18.35	18.19 to 18.51	18.35	18.26 to 18.44	18.50	18.38 to 18.62	0.0868	>0.9999	0.000	-0.1828 to 0.1828	0.1552	0.1500	-0.4172 to 0.3417	0.1552	0.1500	-0.4172 to 0.3417
RDW %CV	18.25	17.41 to 19.09	17.38	15.82 to 18.94	18.12	17.96 to 18.28	0.3137	0.4794	-0.8667	-2.453 to 0.7198	>0.9999	-0.1300	-1.794 to 1.534	0.7465	0.7367	-0.9272 to 2.401
PLT (10^3/µL)	710.0	643.0 to 777.0	696.7	638.3 to 755.1	650.2	597.8 to 702.6	0.2168	>0.9999	-13.33	-100.3 to 73.63	0.2894	-59.80	-151.0 to 31.41	0.5636	-46.47	-137.7 to 44.74
MPV (fL)	5.972	5.670 to 6.274	6.528	5.839 to 7.218	6.520	6.063 to 6.977	0.1043	0.1805	0.5567	-0.1833 to 1.297	0.2263	0.5483	-0.2277 to 1.324	>0.9999	-0.008333	-0.7844 to 0.7677
PCT %	0.4245	0.3748 to 0.4742	0.4520	0.4271 to 0.4769	0.4290	0.3500 to 0.5080	0.4844	0.7847	0.02750	-0.03684 to 0.09184	>0.9999	0.004500	-0.06743 to 0.07643	>0.9999	-0.02300	-0.09493 to 0.04893
PDW 10(GSD)	17.87	17.46 to 18.27	18.73	16.57 to 20.89	18.38	16.71 to 20.04	0.5710	0.9021	0.8667	-1.341 to 3.075	>0.9999	0.5083	-1.960 to 2.977	>0.9999	-0.3583	-2.827 to 2.110

Supplementary table S5: blood cell counts of control and weekly µCT-scanned healthy animals.
WBC=white blood cells; NEU=neutrophils; LYM=lymphocytes; MONO=monocytes; EOS=eosinophils; BASO=basophils; RBC=red blood cells; Hgb=hemoglobin; HCT=hematocrit; MCV=mean corpuscular (cell) volume; MCH=mean corpuscular hemoglobin; MCHC=mean corpuscular hemoglobin concentration; RDW=red cell distribution width; PLT=platelets; MPV=mean platelet volume; PCT=plateletcrit

Chapter 4

Longitudinal micro-computed tomography-derived biomarkers quantify non-resolving lung fibrosis in a silicosis mouse model

Kaat Dekoster, Tatjana Decaesteker, Nathalie Berghen, Sofie Van den Broucke, Anne-Charlotte Jonckheere, Jens Wouters, Anton Krouglov, Rik Lories, Ellen De Langhe, Peter Hoet, Erik Verbeken, Jeroen Vanoirbeek, Greetje Vande Velde

Abstract

In spite of many compounds identified as anti-fibrotic in preclinical studies, pulmonary fibrosis remains a life-threatening condition for which highly effective treatment is still lacking. Towards improving the success-rate of bench-to-bedside translation, we investigated *in vivo* µCT-derived biomarkers to repeatedly quantify experimental silica-induced pulmonary fibrosis and assessed clinically relevant readouts up to several months after silicosis induction. Mice were oropharyngeally instilled with crystalline silica or saline and longitudinally monitored with respiratory-gated-high-resolution µCT to evaluate disease onset and progress using scan-derived biomarkers. At weeks 1, 5, 9 and 15, we assessed lung function, inflammation and fibrosis in subsets of mice in a cross-sectional manner. Silica-instillation increased the non-aerated lung volume, corresponding to onset and progression of inflammatory and fibrotic processes not resolving with time. Moreover, total lung volume progressively increased with silicosis. The volume of healthy, aerated lung first dropped then increased, corresponding to an acute inflammatory response followed by recovery into lower elevated aerated lung volume. Imaging results were confirmed by a significantly decreased Tiffeneau index, increased neutrophilic inflammation, increased IL-13, MCP-1, MIP-2 and TNF-α concentration in bronchoalveolar lavage fluid, increased collagen content and fibrotic nodules. µCT-derived biomarkers enable longitudinal evaluation of early onset inflammation and non-resolving pulmonary fibrosis as well as lung volumes in a sensitive and non-invasive manner. This approach and model of non-resolving lung fibrosis provides quantitative assessment of disease progression and stabilization over weeks and months, essential towards evaluation of fibrotic disease burden and anti-fibrotic therapy evaluation in preclinical studies.

Introduction

Interstitial lung diseases (ILDs) are a heterogeneous group of lung diseases characterized by the presence of cellular proliferation, cellular infiltration and/or fibrosis of the lung parenchyma not due to infection or neoplasia [4,5]. Depending on the cause of disease, different types of ILD can be identified: e.g. hypersensitivity pneumonitis, pulmonary sarcoidosis, silicosis or ILD secondary to an underlying autoimmune disease most of which remain untreatable [5].

Although multiple therapeutic compounds have shown promising results in preclinical models of pulmonary fibrosis, only few of them have been successfully translated to the clinic [6,7,164]. Several challenges in the research field may explain this translational problem. Animal models are indispensable to fibrosis and therapy research but have the inherent limitation that no model exactly mimics the human disease [57,165]. Second, in spite of technological advancements [75,99,166], only endpoint measurements (biochemical assessment of collagen content, gene expression, histology and lung function) are typically used to evaluate the burden of lung disease and drug efficacy. These often come with high variability, only provide a snapshot of a certain stage of the disease and are unable to give temporal and spatial information of the pathology over the entire lung. Moreover, they differ substantially from the endpoints used in clinical studies (e.g. computed tomography, lung functional readouts such as forced vital capacity (FVC), forced expiratory volume (FEV1) and Tiffeneau index (FEV0.1/FVC)), stressing the need for more clinically relevant readouts which would improve comparing pathology in human ILD and animal models thereof, and the preclinical screening efficiency of new therapeutics. Lastly, most often only prophylactic testing of the drug is performed because the currently most used mouse models and readouts only allow for this type of set-up due to their limited and/or variable fibrotic phase. Therapeutic testing when fibrosis is appearing or omnipresent would better mimic the real-life situation and be more relevant to evaluate the anti-fibrotic properties of a putative compound [6].

To evaluate interventions in a truly therapeutic regime, we need to know if, when and how much fibrosis and inflammation are present at the time of drug administration. This is only possible by the use of non-invasive techniques such as imaging by micro-computed tomography (μCT), in combination with a not spontaneously resolving fibrotic disease model. The often-used acute bleomycin model is characterized by spontaneous regression of fibrosis, an observation that does not reflect reality in human patients. Chronic models of lung fibrosis such as the silica-induced pulmonary fibrosis model better resemble this persistent aspect of human disease and may therefore be a better model for preclinical studies.

µCT has already proven to have important benefits for longitudinal evaluation of disease in preclinical animal models [75,91,99-102]. Due to its high air-tissue contrast, it is a particularly excellent technique to study and quantify lung disease burden such as pulmonary fibrosis [75,91-94], whereby its added non-invasive value to standard endpoint readouts such as histology and hydroxyproline assays has been established. Yet, most often µCT is still not implemented in preclinical therapy studies in spite of its capacity to longitudinally visualize and quantify the inflammatory and fibrotic process for each animal individually, thereby identifying the window for therapeutic intervention.

Bridging the gap between preclinical and clinical research by assessing quantitative and clinically relevant CT- and lung function-derived readouts in a relevant animal model would have critical impact on research efficiency in identifying therapeutic targets and compounds, ultimately leading to better patient care. Therefore, we here (1) evaluate the silica-induced pulmonary fibrosis model with *in vivo* and *ex vivo* readouts and postulate it to be a model more relevant to human disease; (2) we assess the added value of longitudinal imaging using µCT to provide non-invasive biomarkers characterizing pulmonary fibrosis progression in mouse and (3) we correlate *in vivo* µCT-derived biomarkers with endpoint measurements of lung function, host response and lung fibrosis, thereby addressing analogies and dissimilarities between mouse and human fibrotic lung disease regarding interpretation of clinically relevant readouts.

Materials and methods

Animal model

All animal experiments were carried out in compliance with national and European regulations and were approved by the animal ethics committee of KU Leuven (P057/2018). Mice were kept in a conventional animal facility with individually ventilated cages and free access to food and water. Eight-week-old male C57Bl/6JRj mice (Janvier, Le Genest, France) were oropharyngeally instilled with crystalline silica particles (5 mg/animal), kindly provided by B Fubini (Facoltà di Farmacia, Università di Torino, Italy), or saline (NaCl 0.9%). Silica particles were baked for 2 hours at 180°C and dissolved in saline with a concentration of 0.125 mg/µL. Next, the solution was probe sonicated for 16 minutes. Animals were anesthetized by inhalation of 5% isoflurane (Piramal Healthycare, Morpeth, Northumberlang, United Kingdom) in 100% oxygen. By simultaneously holding the tongue and covering the nose, animals were oropharyngeal instilled with 40 µL of silica/saline [63,167].

Experimental design

Mice were randomly divided over treatment groups. Animals were scanned at baseline, weekly for the first 5 weeks and every two weeks for the following 10 weeks. At 1, 5, 9 and 15 weeks after silica instillation, a randomly selected cohort of the animals was sacrificed for endpoint measurements (Figure 1). The total number of animals used was 58.
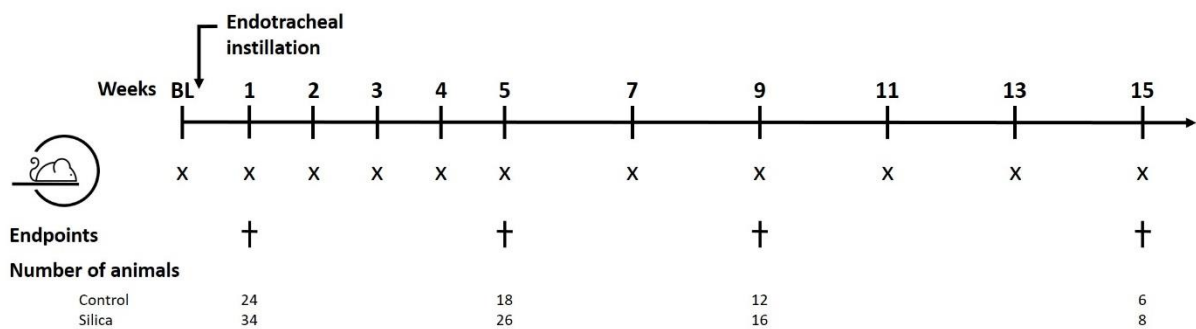

Figure 1: experimental design.
This scheme summarizes the followed protocol. X indicates a µCT scan. At four endpoints (1, 5, 9 and 15 weeks post instillation), a cohort of animals was sacrificed to obtain lung function and *ex vivo* measurements. At each endpoint, the number of animals is indicated and represents the number of animals up until that endpoint.

Micro-computed tomography

Mice were anesthetized by inhalation of 1.5-2% isoflurane in 100% oxygen and scanned in supine position using a dedicated *in vivo* µCT scanner (Skyscan 1278, Bruker µCT, Kontich, Belgium). The following parameters were used: 50 kVp X-ray source voltage and 918 µA current combined with a composite X-ray filter of 1 mm aluminium, 55 ms exposure time per projection, acquiring projections with 0.9° increments over a total angle of 220°, and 10 cm field of view covering the whole body

producing reconstructed 3D data sets with 50 µm isotropic reconstructed voxel size. The data was acquired with retrospective respiratory gating; images were acquired in list mode with 9 projections per view, retrospectively time-based sorted, resulting in four reconstructed 3D data sets corresponding to four different phases of the breathing cycle (4D). We here report data at the end of the expiratory phase.

Software provided by the manufacturer (TSort, NRecon, DataViewer, and CTan) was used to retrospectively gate, reconstruct, visualize, and process µCT data as described previously [89,128]. For Hounsfield unit (HU) calibration, a phantom was scanned consisting of an air-filled 1.5 mL tube inside a water-filled 50 mL tube. Based on full stack histograms of a volume-of-interest (VOI) containing only water or air, the main grayscale index of water (133) was set at 0 HU and grayscale index of air (9) at -1000 HU. Quantification of the mean lung density, non-aerated lung volume, aerated lung volume, and total lung volume was carried out for a VOI covering the lung, manually delineated on the coronal µCT images, avoiding the heart and main blood vessels. When defining the VOI covering the lungs, we define the top of the lungs by the CT section defined by the point where the clavicle touches the sternum and the bottom by a plane under the lungs through the liver. The threshold used to distinguish aerated from non-aerated lung tissue volume was manually set at -223 HU and kept constant for all data sets.

Pulmonary function

Lung function was assessed at 1, 5, 9 and 15 weeks after silica instillation using the flexiVent FX system (SCIREQ, EMKA Technologies, Montreal, Canada). The system was designed to concurrently measure forced oscillations and forced expiration parameters, as described previously [166]. Briefly, the system operated with flexiWare 7.6 software and was equipped with a FX1 module, a negative pressure forced expiration (NPFE) extension for mice. Mice were anesthetized with an intraperitoneal injection of pentobarbital (70 mg/kg BW, Nembutal). Once sufficiently anesthetized, a tracheotomy was performed to insert an 18-gauge metal cannula. Mice were quasi-sinusoidal ventilated with a tidal volume of 10 mL/kg and a frequency of 150 breaths/min to mimic spontaneous breathing.

At the start of the experiment, two successive deep inflations were applied to maximally inflate the lungs to a pressure of 30 cmH2O in order to open the lungs and determine the inspiratory capacity (IC). Between each set of perturbation, a deep inflation was applied. Next, the forced oscillation perturbation 'Prime-8' (P8) that generates forced oscillations with a frequency between 1-20.5 Hz during 8 sec, was executed five times. The reported central airway resistance (Rn), tissue damping (G), tissue elasticity (H) and tissue hysteresivity (eta = G/H) are the average of three measurements. Next, a NPFE (negative pressure forced expiratory flow) perturbation was performed to measure the peak expiratory flow (PEF), forced vital capacity (FVC) and forced expiratory volume in 0.1 seconds (FEV0.1).

Reported values are the average of three accepted measurements (COD>0.9) for each individual data point.

Inflammatory and permeability evaluations

Immediately after the lung function measurements, plasma was collected to measure surfactant protein (SP)-D concentration by ELISA (Duoset ELISA, R&D Systems Inc., DY6839-05) according to the manufacturers' instructions. The whole lung was lavaged three times *in situ* with 0.7 mL sterile saline (0.9% NaCl), the collected fluid pooled and analysed for total and differential cell counts. The total number of cells in the BAL fluid was counted using a Bürker hemocytometer. Subsequently the bronchoalveolar lavage (BAL) fluid was centrifuged (1000 g, 4 °C, 10 min) and the supernatant collected and frozen (-80 °C) until further analysis. For differential cell counts, the cells were resuspended in 1 mL saline (0.9% NaCl), of which 250 µL of the resuspended cells were spun (300 g, 4 °C, 6 min; Cytospin 3, Shandon, TechGen, Zellik, Belgium) onto microscope slices, air-dried and stained (Diff-Quik method, Medical Diagnostics, Düdingen, Germany). For each sample, 200 cells were counted to quantify the number of macrophages, eosinophils, neutrophils and lymphocytes. Protein concentration was determined on the cell-free BAL supernatant using the Bradford method with bovine serum albumin as a standard. Cytokine counts (IFN-γ, IL-10, IL-13, IL-1β, IL-17A, IL-17F, IL-6, MCP-1, MIP-2, TNF-α, TGF-β1, TGF-β2 and TGF-β3) were determined on the cell-free BAL supernatant using a U-PLEX Biomarker Assay and U-PLEX TGF-β Combo Assay (Meso Scale Discovery, Maryland, USA) according to manufacturers' instructions.

Histopathological and histochemical analysis

The left lung lobe was manually inflated up until physiological total lung capacity was reached, fixed with 4% paraformaldehyde and paraffin embedded. 5 µm sagittal sections were stained with haematoxylin-eosin (H&E) and Sirius red and examined with polarized light to visualize the silica particles and collagen formation.

The right lung lobes were clamped, collected and stored at -80 °C for hydroxyproline quantification as previously described [154]. In short, right lung lobes were hydrolysed for 3 hours in 6M HCl at 120 °C. After cooling down for 15 minutes, the pH was neutralized (pH 6–7) using 500 ml NaOH. Free hydroxyproline was oxidized with Chloramine-T for 20 minutes after which the oxidation reaction was stopped using 70% perchloric acid. Ehrlich's reagent was added, and samples were heated for 20 minutes in a 60 °C water bath. After cooling down, absorbance was measured at 570 nm and concentrations were calculated based on a standard curve. OH-proline concentrations are given per right lung lobes.

Statistical analysis

The data were analysed using GraphPad Prism (version 8.02. Graphpad Software Inc., San Diego, USA). The data are presented as mean with standard deviation (SD). Normal distribution was assessed by the Kolmogorov-Smirnov test and visual inspection of the QQ-plots. For cross-sectional data with a balanced design, two-way ANOVA with Sidak's multiple comparison *post hoc* test was performed. Two-way ANOVA with Sidak's correction for multiple comparison was based on the following number of animals: w1 6 control and 6 silica mice; w5 6 control and 10 silica mice; w9 6 control and 8 silica mice; w15 6 control and 8 silica mice. Data of longitudinal µCT-derived biomarkers (with missing values and an unbalanced design; mean lung density, total lung volume, non-aerated lung volume and aerated lung volume) were analysed using a mixed-effects model with Geisser-Greenhouse correction, for assessing the interaction between time and treatment. For multiple comparison, Sidak's *post hoc* test was used. Mixed-effects model with Geisser-Greenhouse correction was based on the following number of animals for every timepoint: BL-w1 24 control and 34 silica mice; w2-5 18 control and 26 silica mice; w7-9 12 control and 16 silica mice; w11-15 6 control and 8 silica mice. For correlation analysis, the Pearson correlation coefficient was determined. For all tests, statistical significance was assumed when * p-value < 0.05; ** p-value < 0.01 and *** p-value < 0.001.

Results

In vivo µCT non-invasively captures the non-resolving inflammatory and fibrotic response to silica instillation

Mice were instilled with silica or vehicle, scanned at baseline and longitudinally for a period of 15 weeks with respiratory-gated high-resolution low-dose µCT. Silica-instilled mice initially lost weight, then fully recovered and regained normal body weight within 7-14 days without signs of distress (Figure S1). Survival rate was 100%.

µCT showed large hyperdense areas that were most pronounced one week after silica-instillation, most likely corresponding to acute inflammatory processes (Figure 2a).
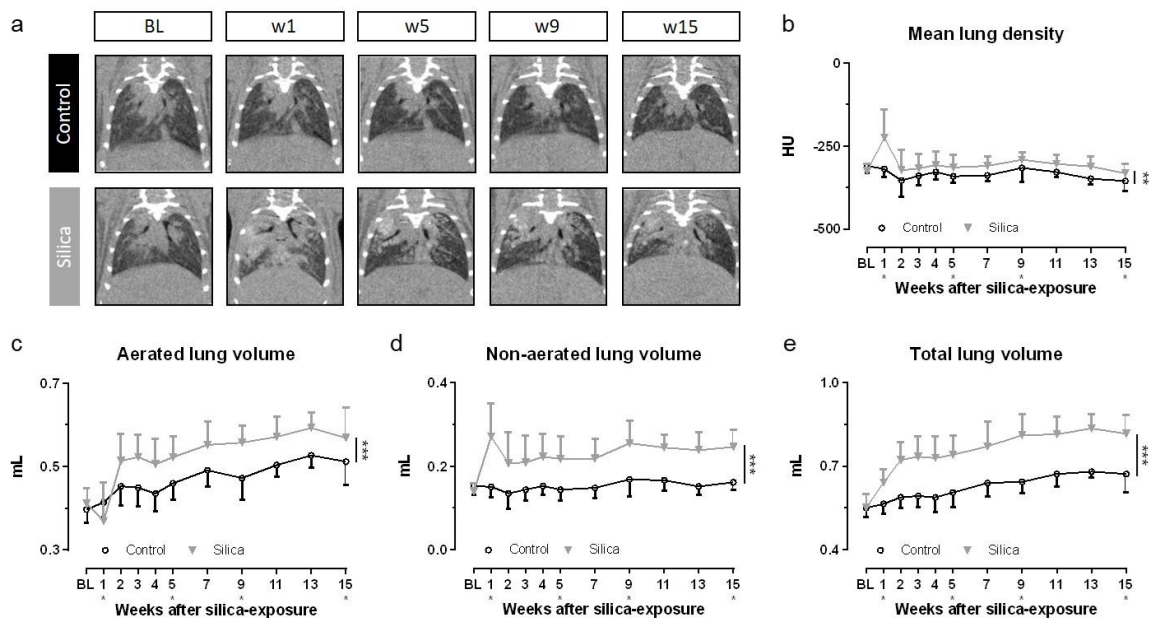

Figure 2: µCT visualizes and quantifies onset and progression of the inflammatory and fibrotic response upon silica-instillation.
(a) Representative images of one control and one silica-instilled animal at selected time points, from baseline up until 15 weeks, visualize the inflammatory and fibrotic response. µCT-derived biomarkers reflect disease onset and progression in silica-instilled animals: (b) mean lung density expressed in HU (c) aerated lung volume (mL) (d) non-aerated lung volume (mL) (e) total lung volume (mL). Data are presented as mean ± SD. Full line represents longitudinal data. Mixed-effects model with Geisser-Greenhouse correction was based on the following number of animals for every timepoint: BL-w1 24 control and 34 silica mice; w2-5 18 control and 26 silica mice; w7-9 12 control and 16 silica mice; w11-15 6 control and 8 silica mice. * p-value < 0.05; *** p-value < 0.001; BL=baseline; *under the x-axes indicate endpoints.

Past the first week, the presence of hyperdense areas remained extensive but their volume and density decreased to then remain stable, coinciding with the regain of body weight. Quantification of longitudinal µCT-derived biomarkers corroborated these visual observations (Figure 2b-e). Silica instillation resulted in a significantly increased mean lung density starting at week 1 that remained present until endpoint. The non-aerated lung volume, which directly quantifies inflammatory and

fibrotic disease burden [89], also peaked at week 1 and remained significantly and stably increased up until endpoint. The aerated lung volume transiently decreased at week 1 to steadily increase at elevated levels thereafter, in contrast to loss of aerated lung volume previously observed in the bleomycin model [75]. The bleomycin induced pulmonary fibrosis model is a more acute model than the silica-induced model. Animals do not have the time to increase their aerated lung volume to compensate for the increase in non-aerated lung volume and loss of airspaces.

The increase in aerated and non-aerated lung volume is paralleled by the total lung volume that is progressively increased up until endpoint in silica-instilled mice, in contrast to control mice where small lung volume changes only reflect normal changes with aging [89].
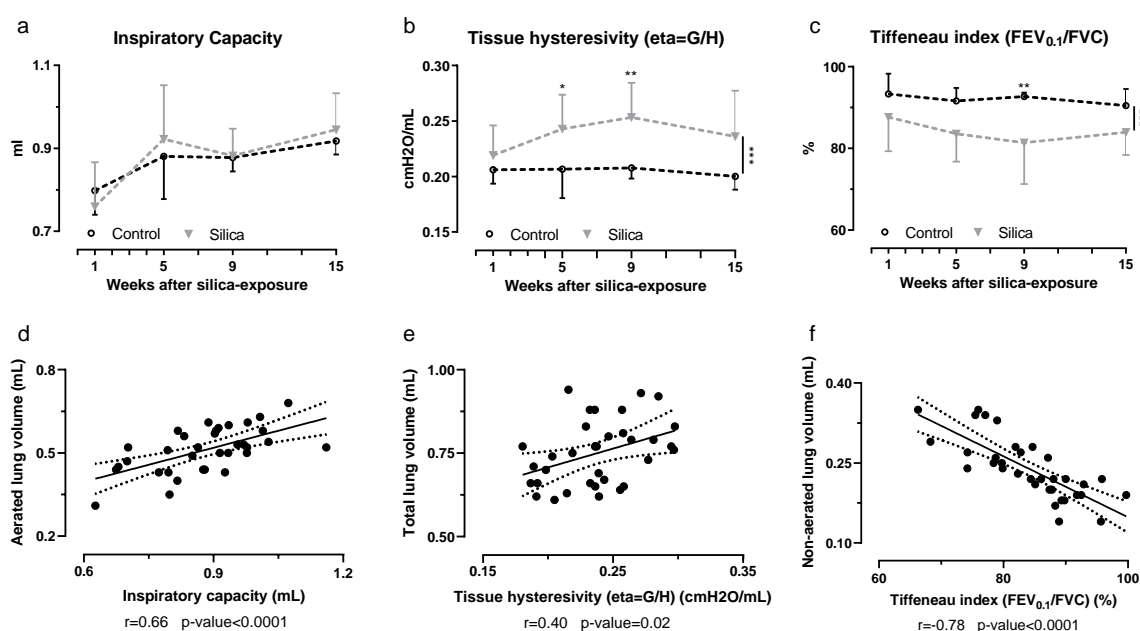

Figure 3: pulmonary function data reflect fibrotic disease and correlate with *in vivo* µCT-derived biomarkers.
At every endpoint, lung function was assessed by performing (a) deep inflation, (b) forced oscillations and (c) negative pressure-driven forced expiration maneuvers. Data are presented as mean ± SD. Dashed line represents cross-sectional data. Two-way ANOVA with Sidak's correction for multiple comparison was based on the following number of animals: w1 6 control and 6 silica mice; w5 6 control and 10 silica mice; w9 6 control and 8 silica mice; w15 6 control and 8 silica mice. * p-value < 0.05; ** p-value < 0.01; *** p-value < 0.001. Correlations between µCT-derived biomarkers and lung function measurements indicate the agreement between both methods (d) aerated lung volume and inspiratory capacity (e) total lung volume and tissue hysteresivity (f) non-aerated lung volume and Tiffeneau index. For every correlation the Pearson correlation coefficient and the p-value are given. Correlations only include silica-instilled animals.

Silica instillation significantly alters lung function

We cross-validated our *in vivo* µCT findings with lung function readouts at endpoint from sub-cohorts of animals at week 1, 5, 9 and 15 after instillation. These timepoints were chosen to cover the initial inflammatory phase (week 1) followed by the fibrotic phase (week 5-15). The inspiratory capacity of silica mice was unaltered compared to controls (Figure 3a) and correlated with the aerated lung volume derived from the µCT scans (r = 0.6612, p-value < 0.0001) (Figure 3d). The airway resistance,

tissue damping and tissue elasticity were not different after silica-instillation (Figure S3a-f), but the tissue hysteresivity, reflecting tissue inhomogeneity's and structural changes in the lungs, was significantly increased and correlated with the total lung volume (r = 0.4027, p-value = 0.0182) (Figure 3b-e). The Tiffeneau index (FEV0.1/FVC) was significantly decreased after silica instillation and correlated with the non-aerated lung volume (r = 0.7764, p-value < 0.0001) (Figure 3c-f). Contrary to what would be expected in human restrictive disease but consistent with the µCT-derived lung volumes for this model, peak expiratory flow, forced vital capacity and forced expiratory flow in 0.1s were not affected in this mouse model (Figure S3g-l).
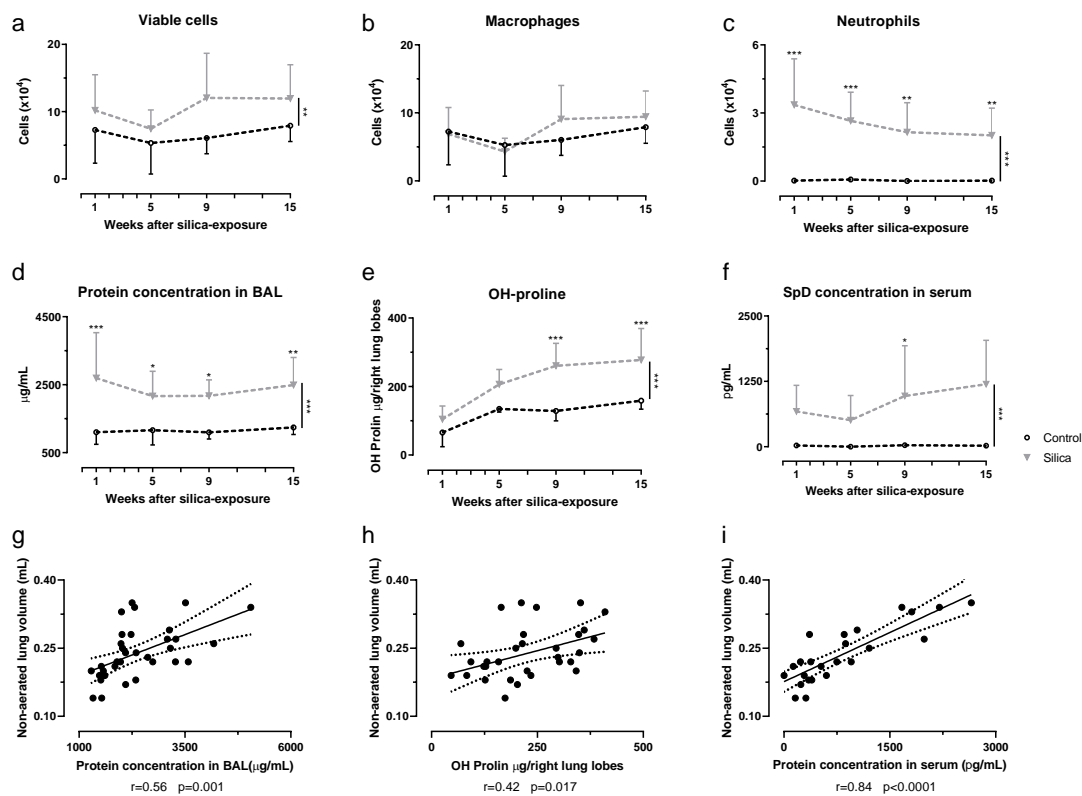

Figure 4: silica-instillation changes inflammatory readouts of BAL fluid and serum and increases the collagen content.
At every endpoint, several *ex vivo* readouts for inflammatory and fibrotic responses were obtained. Silica instillation changed the number of viable cells (a) and neutrophils (c) but did not alter the number of macrophages (b) in the BAL fluid. Moreover, silica increased the protein concentration in the BAL fluid (d), the collagen content measured by OH-proline assay reflecting a fibrotic response on the silica particles (e) and the surfactant protein D (SpD) concentration in serum (f). Data are presented as mean ± SD. Dashed line represents cross-sectional data. Two-way ANOVA with Sidak's correction for multiple comparison was based on the following number of animals: w1 6 control and 6 silica mice; w5 6 control and 10 silica mice; w9 6 control and 8 silica mice; w15 6 control and 8 silica mice. * p-value < 0.05; ** p-value < 0.01; *** p-value < 0.001. Correlations between µCT-derived biomarkers and *ex vivo* measurements indicate the agreement between the inflammatory and fibrotic disease and µCT-derived biomarkers (g) non-aerated lung volume and protein concentration in bronchoalveolar lavage fluid, (h) non-aerated lung volume and OH-proline content, (i) non-aerated lung volume and protein concentration in serum. For every correlation the Pearson correlation coefficient is given and the p-value. Correlations only include silica-instilled animals.

Ex vivo readouts confirm the functional and imaging-based detection of inflammatory and fibrotic responses

Cellular analysis of the BALF showed a significant neutrophilic inflammation that remained elevated up until 15 weeks (20% neutrophils of total cells at 15 weeks, Figure S2) and did not differ significantly between time points (Figure 4a-c, Figure S2). The number of macrophages was unaffected. Additionally, protein concentration in BALF increased (Figure 4d), indicative of the inside-out leaky epithelium. Surfactant protein D (SpD) concentration in serum was significantly elevated upon silica instillation, which points to outside-in leakage. The hydroxyproline content, reflecting the amount of collagen in lung tissue, was significantly elevated from 9 weeks on (Figure 4e). Both the higher inflammatory and fibrotic burden determined from the µCT scans (non-aerated lung volume) correlated with a higher protein concentration in BALF ($r = 0.5557$, p-value = 0.0006), serum ($r = 0.8445$, p-value < 0.0001) and OH-proline content ($r = 0.4187$, p-value = 0.0171) (Figure 4g-i).

Further characterizing the time course of the inflammatory and fibrotic response to silica-induction revealed that silica instillation resulted in a significant elevation of type 2 cytokine IL-13 and pro-inflammatory cytokines TNF-α and MIP-2 levels (Figure 5a-c). Moreover, we observed an overall increase of type 1 cytokine IFN-γ, type 2 cytokine IL-10, type 3 cytokines IL-17A and IL-17F, pro-inflammatory cytokines IL-1β and IL-6, chemokine MCP-1 and pro-fibrotic cytokines TGF-β1 and TGF-β2 (Figure S4a-i). No significant difference was found for TGF-β3 (Figure S4j).
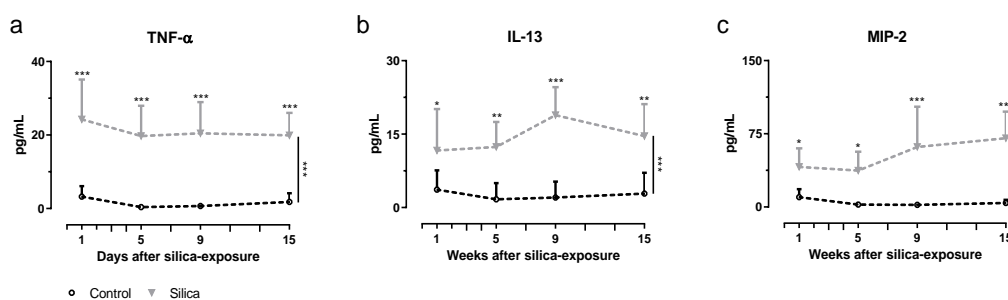

Figure 5: silica instillation induces a pro-inflammatory response characterized by an increased TNF-α, IL-13 and MIP-2 content in BAL fluid.

At every endpoint cytokine concentration was determined. Silica-instillation altered the amount of (a) TNF-α, (b) IL-13 and (c) MIP-2 concentration in the BAL fluid. Data is presented as mean ± SD. Dashed line represents cross-sectional data. Two-way ANOVA with Sidak's correction for multiple comparison was based on the following number of animals: w1 6 control and 6 silica mice; w5 6 control and 10 silica mice; w9 6 control and 8 silica mice; w15 6 control and 8 silica mice. * p-value < 0.05; ** p-value < 0.01; *** p-value < 0.001.

One week after silica-instillation, histopathological examination showed a general, mostly centrilobular located inflammatory reaction that was completely absent in controls (Figure 6). Silica particles were encapsulated with neutrophils, macrophages, proteins and wound fluid. Only native

collagen was observed at this timepoint, same as in control animals. Five weeks after silica instillation, polarization microscopy visualized newly formed collagen indicating a fibrotic pattern consisting of several fibrotic nodules, located centrilobularly. The same type of pathology was observed at 9- and 15-weeks post instillation indicating long-lasting fibrosis, whereas controls did not show any inflammatory response nor fibrotic nodules at any time point.
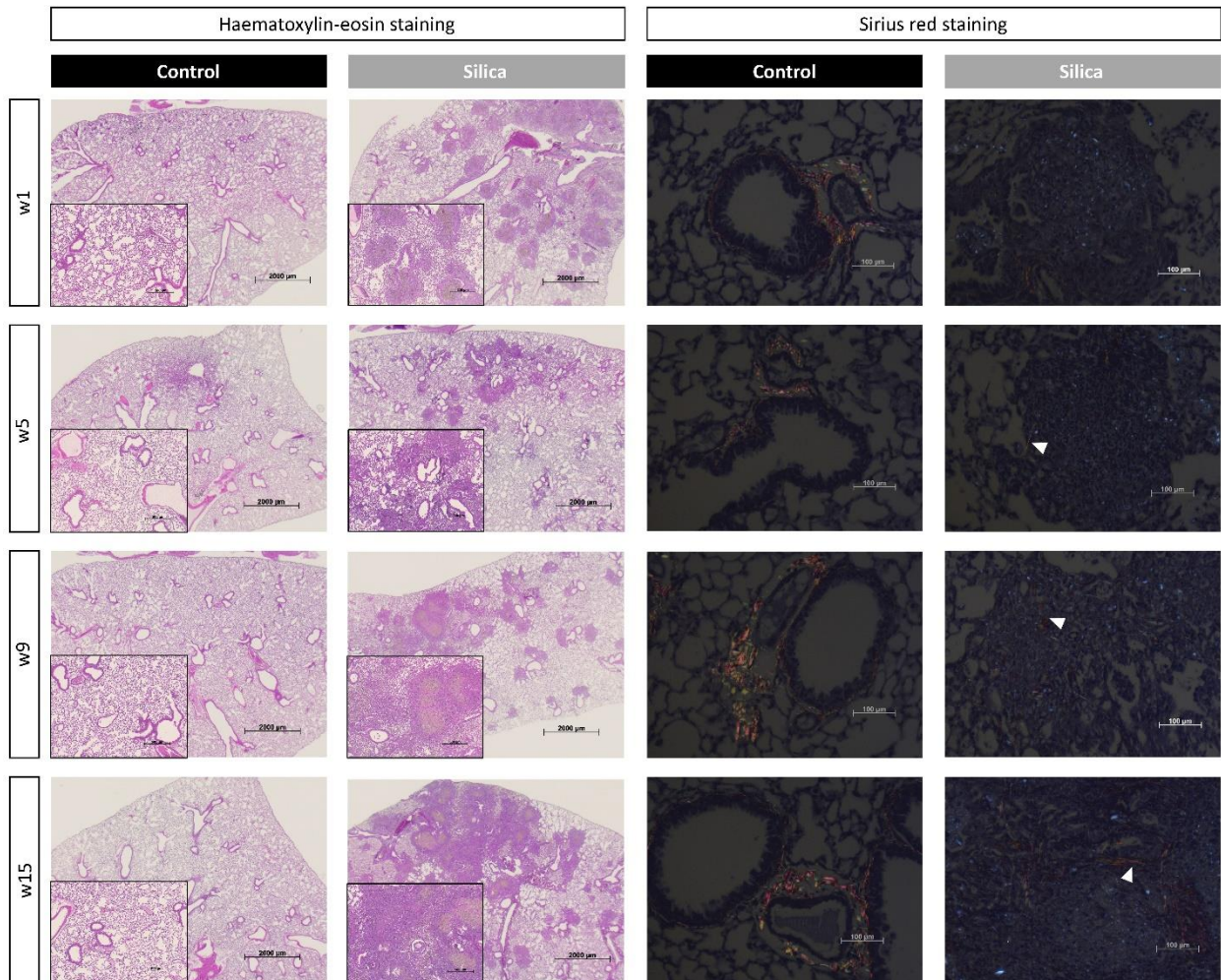

Figure 6: histopathological analysis of silica-instilled animals at every timepoint.
Representative H&E stained images are shown for every timepoint for control and silica-instilled animals (magnification of 12.5x and 50x). Representative Sirius Red images are shown for every timepoint for control and silica-instilled animals (magnification of 200x). For control animals, only native collagen is shown in centrilobular area. For silica-instilled animals, centrilobular located nodules with increasing amount of newly formed collagen (indicated with white arrows) are shown.

Discussion

More and more attention has been given to the disease silicosis lately, as it affects millions of people in India, China, Australia, Turkey and USA, emphasizing the importance of silica-induced pulmonary fibrosis research [168-170]. Clinically relevant readouts delivered by translational techniques such as µCT and lung function measurements would add to the current standard methodology used to evaluate disease process and therapeutic effects in pulmonary fibrosis mouse models [6]. In this study, we show that *in vivo* longitudinal µCT-derived biomarkers identify and quantify lung inflammatory and fibrotic disease in the context of silicosis, its onset and progress, which is paramount over endpoint readouts and will allow precise timing of possible future anti-fibrotic therapy testing.

We selected a silica-induced pulmonary fibrosis model for which we identified a steady-state fibrotic phase of 10 weeks in which interventions can be tested. We cross-validated with *in vivo* µCT-derived biomarkers, lung function and routinely used *ex vivo* read-outs that fibrosis did not spontaneously resolve. This study is the first to demonstrate the power of µCT to deliver non-invasive biomarkers that quantify in a mouse model of silica-induced fibrosis in a longitudinal manner the degree of inflammation and fibrosis, on top of providing visual information of silicosis [92,94]. The combination of imaging-derived biomarkers with a persistent fibrotic mouse model and translational readouts such as the Tiffeneau index is a novel approach that allows assessment of disease progression and its stabilization over several weeks.

The choice of animal model to mimic human lung fibrotic disease and the way it is evaluated is essential for the translational relevance of mouse study results to man. At present, the most used and best-characterized animal model for lung fibrosis research and therapy evaluation is the more acute bleomycin model [55,57]. This model suffers from a high mortality rate and variability, is prone to survival bias and is claimed to be self-limiting in time [55]. The short timespan over which fibrosis develops and peaks does not allow truly therapeutic testing of interventions with anti-fibrotic potential, warranting gearing up to alternative, chronic models where fibrosis does not spontaneously resolve, such as irradiation-induced lung fibrosis [78,171], transgenic mice and silicosis [172]. Silica instillation leads to fibrotic nodules that resemble those seen in patients exposed to environmental triggers such as dust and particulates [57]. When combined with longitudinal µCT, we here confirm that fibrosis is persistent in this model, offering a 10-week time frame allowing to test therapeutics [57,65], two of the key aspects that the most often-used bleomycin model is lacking. Additionally, it is cheap, easy to perform, has a low inter-animal variability, zero mortality rate and a 100% success rate of fibrosis development. Disadvantages of this model are the lack of reproducibility of the fibrotic pattern and the UIP pattern observed in IPF patients is not present [57,65].

Further in-depth characterization of the inflammatory and fibrotic response in this model revealed neutrophilic inflammation, peaking one week after silica instillation to slowly decrease to a neutrophilic inflammation of 20%, indicating a constant trigger of the immune system since particles are not easily cleared from the lungs by alveolar macrophages [64]. The neutrophilic inflammation is in concordance with several other studies [86,173], although not as chronic as in our model, which might be due to differences in administration method, type and dose of silica and mouse strain used. Macrophages are the first to ingest silica particles, resulting in a cascade involving other inflammatory cells and several pro-inflammatory cytokines and chemokines [64,174]. We did not find an increased number of macrophages, though we did not evaluate macrophage activation status, nor macrophage sub-types. Studies have shown that both the M1 (pro-inflammatory) and M2 (anti-inflammatory/pro-fibrotic) subtypes play an important role in the silica-induced pathology [175].

We found a variety of cytokines and chemokines in this silicosis model that have been implicated with pulmonary fibrosis. The increased concentration of TNF-α and IFN-γ suggests a pro-inflammatory response [92,176,177]. IL-13, mostly associated with wound-healing processes and considered pro-fibrotic, was increased during the entire disease process, indicating a type-2 response. Though Liu *et al*. suggest an induction of the Th2-response by crystalline silica particles [178], we cannot conclude whether the increased IL-13 concentration is originating from Innate Lymphoid Cells type 2, Th2-cells or the epithelial cells since we did not formerly assess lymphocytes in lung tissue [179]. Type 3 cytokines IL-17A and IL-17F were elevated in our model as well as in other silica models [180]. All these readouts, together with the increased pro-fibrotic TGF-β cytokine, put forward an interplay between several innate and adaptive inflammatory (type 1, 2 and 3) and fibrotic processes over the entire time course of disease. We found an elevated SP-D concentration in serum, consistent with a similar finding in rats [181]. Alveolar type II and bronchiolar epithelial cells are responsible for the overproduction of SP-D after silica instillation and increased plasma SP-D levels have been suggested as an indication of lung injury and inflammation [64,182]. Together with the increased protein concentration in the BALF, this indicates epithelial damage due to the silica particles and a leaky epithelial barrier.

Several inflammatory and fibrotic indicators (protein concentrations in BAL, serum and OH-proline content) correlated with the non-aerated lung volume derived from the μCT scans. Moreover, lung function-derived tissue hysteresivity differences clearly indicate tissue inhomogeneity's corresponding to inflammation and non-resolving fibrosis that also correlated with the μCT-derived non-aerated lung volume. We therefore propose the non-aerated lung volume as an alternative, non-invasive marker of disease burden consisting of intertwined fibrotic as well as inflammatory responses.

Where the non-aerated lung volume is a direct quantitative marker for the extent of pathology, the

aerated lung volume is regarded a biomarker of lung function. Indeed, it correlated with volumetric readouts from endpoint lung function measurements such as inspiratory capacity. In this silicosis model, the aerated lung volume is enlarged during the plateau of the fibrotic phase, consistent with the absence of a lowered inspiratory capacity, FVC, FEV0.1 or increased elasticity; lung function readouts that would typically be affected in human restrictive disease or in the bleomycin model [75,166,183].

The key to correct interpretation of lung function readouts lies in the consistently increased total lung volume retrieved from the μCT scans, reflecting enlargement of the lungs with silicosis (Figure 2e). We interpret the enlargement of total lung volume, observed in this and other mouse models of lung diseases, as a compensation mechanism for the otherwise excessive loss of airspaces [89,100,184,185]. This phenomenon is absent in human patients, but in mouse models this enlargement of the lungs affects the interpretation of μCT-and lung function-derived readouts. Where lung function volumetric readouts may underestimate the presence of restrictive lung disease in this model, μCT offers readouts on the presence of inflammation and fibrosis and potential compensatory reaction thereto by enlargement of (aerated) lung volumes. Our findings here further emphasize the paramount importance of adding μCT examinations to the standard preclinical workflow to characterize the response of mouse models to lung insults.

Our imaging approach overcomes the limitations of standard endpoint assessments and lung function examinations, allows the individual monitoring of every animal throughout its entire disease process, thereby giving information with high statistical power on the extent of inflammatory and fibrotic processes. Including μCT-derived biomarkers in fibrosis research gives us important opportunities towards translation of preclinical study results given the availability of medical imaging data in routine patient care, and opens up avenues towards testing interventions therapeutically. This provides the necessary leap forward to move away from the currently most used prophylactic way of anti-fibrotic drug evaluation.

Acknowledgements

Author contribution

G.V.V. and J.V. conceived the study. K.D., J.V. and G.V.V. designed the experiments. K.D., T.D., N.B., S. V., A.J., J.W., A.K. and J.V. performed the experiments. K.D., E.V. and J.V. analyzed the data. J.V. and G.V.V. supervised the experiments and data analysis. K.D. wrote the manuscript. J.V., R.L., E.D., P.H., E.V. and G.V.V. reviewed the manuscript. All authors have read and approved the final manuscript.

Conflict of interest

All authors declare no conflict of interest related to this work.
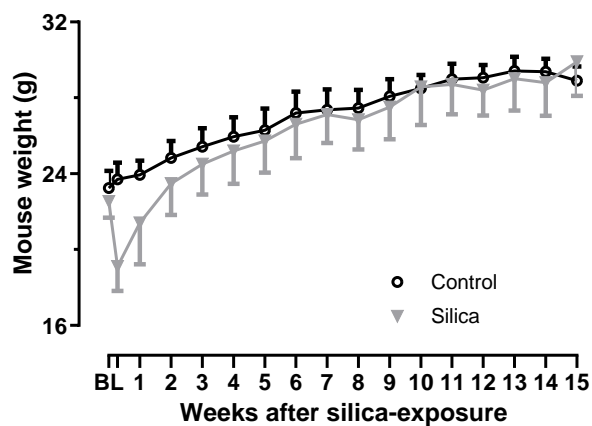
Supplementary figures

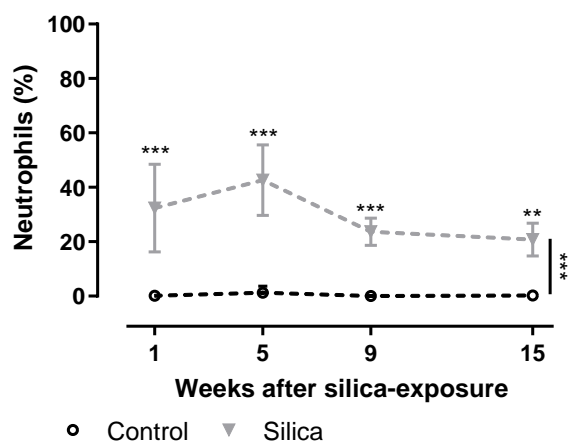**Figure S1: mouse weight after silica exposure.**

Figure S2: percentage of neutrophils after silica exposure.
At every endpoint, *ex vivo* readouts for inflammatory and fibrotic responses were obtained. Silica instillation changed the percentage of neutrophils. Data are presented as mean ± SD. Dashed line represents cross-sectional data. Two-way ANOVA with Sidak's correction for multiple comparison was based on the following number of animals: w1 6 control and 6 silica mice; w5 6 control and 10 silica mice; w9 6 control and 8 silica mice; w15 6 control and 8 silica mice. ** p-value < 0.01; *** p-value < 0.001.
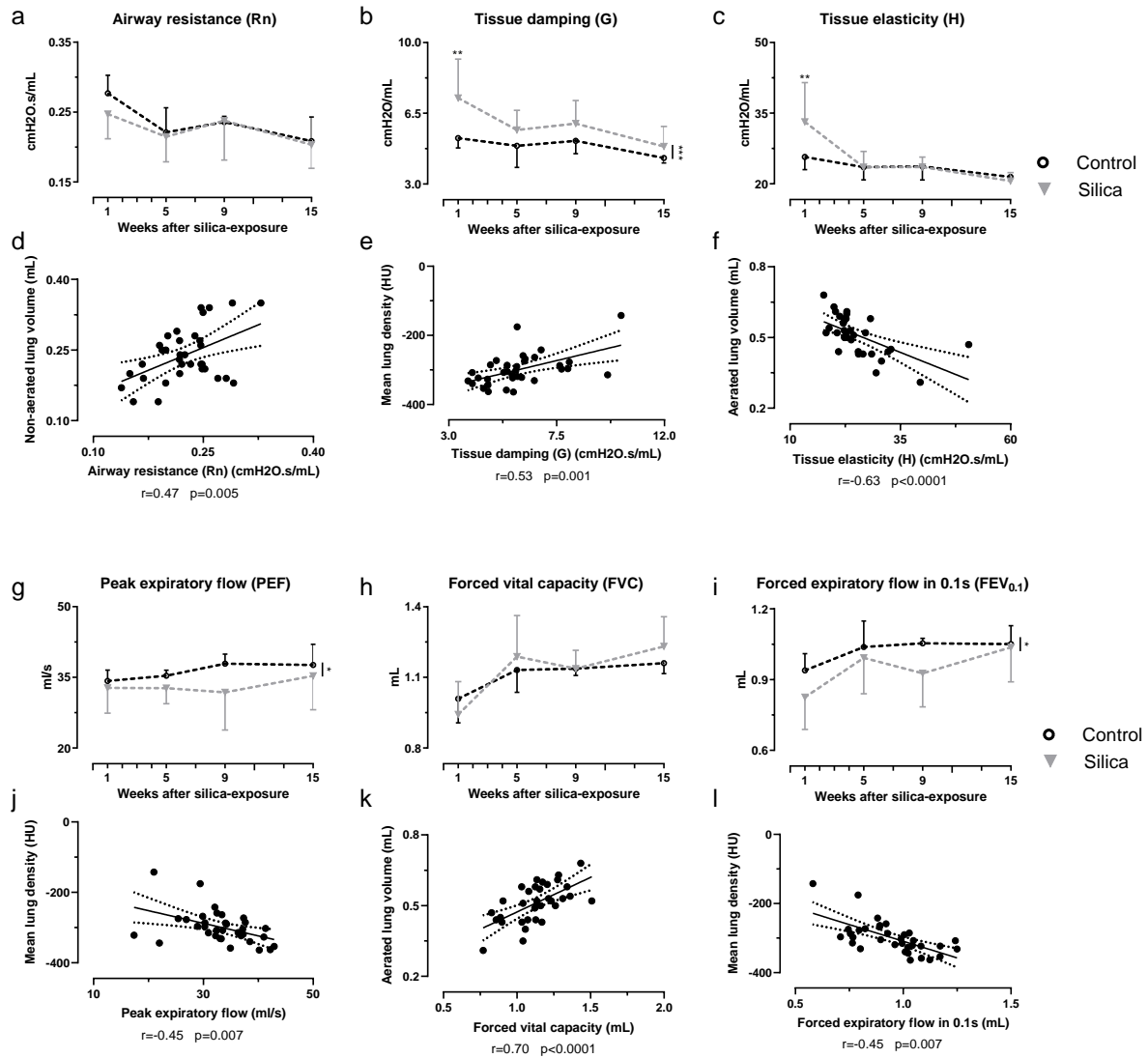
Figure S3: additional pulmonary function readouts and their correlation with *in vivo* µCT-derived biomarkers.
At every endpoint lung function was assessed by performing deep inflation, (a-c) forced oscillations and (g-i) negative pressure-driven forced expiration maneuvers. Data are presented as mean ± SD. Dashed line represents cross-sectional data. Two-way ANOVA with Sidak's correction for multiple comparison was based on the following number of animals: w1 6 control and 6 silica mice; w5 6 control and 10 silica mice; w9 6 control and 8 silica mice; w15 6 control and 8 silica mice. * p-value < 0.05; ** p-value < 0.01; *** p-value < 0.001. Correlations between µCT-derived biomarkers and lung function measurements indicate the agreement between both methods (d) non- aerated lung volume and R, (e) mean lung density and G, (f) aerated lung volume and H, (j) mean lung density and PEF, (k) aerated lung volume and FVC, (l) mean lung density and FEV0.1. For every correlation the Pearson correlation coefficient is given and the p-value. Correlations only include silica-instilled animals.
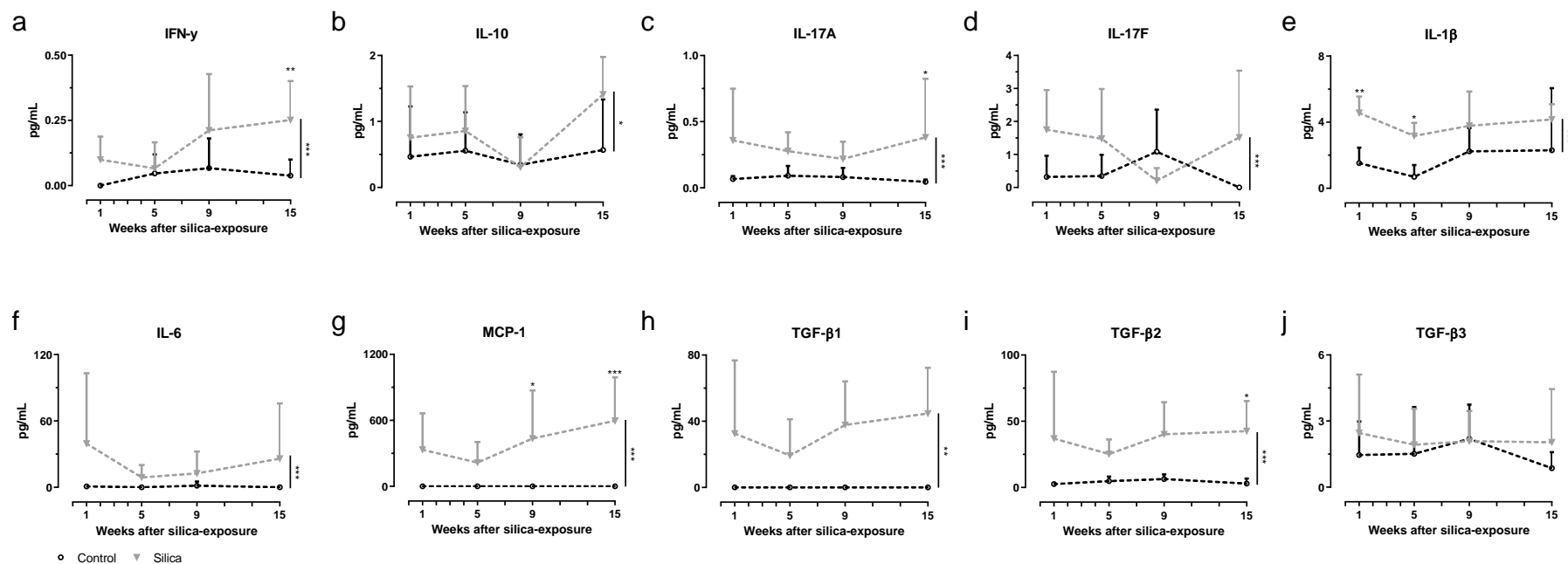
Figure S4: additional cytokines involved in inflammatory and fibrotic response measured in the BAL fluid.
At every endpoint, different cytokine concentrations were determined. Silica instillation changed the amount of (a) IFN-γ, (b) IL-10, (c) IL-17A, (d) IL-17F, (e) IL-1β, (f) IL-6, (g) MCP-1, (h) TGF-β1, (i) TGF-β2 concentration in the BAL fluid. It did not significantly change the (j) TGF-β3 concentration in the BAL fluid. Data are presented as mean ± SD. Dashed line represents cross-sectional data. Two-way ANOVA with Sidak's correction for multiple comparison was based on the following number of animals: w1 6 control and 6 silica mice; w5 6 control and 10 silica mice; w9 6 control and 8 silica mice; w15 6 control and 8 silica mice. For TGF-β1-2-3 analysis, the following number of animals was used: w1 6 control and 8 silica mice; w5 6 control and 9 silica mice; w9 6 control and 8 silica mice; w15 6 control and 8 silica mice. * p-value < 0.05; ** p-value < 0.01; *** p-value < 0.001.

Chapter 5

µCT: a preclinical anti-fibrotic drug screening tool?

Kaat Dekoster, Jorien Derycke, Anne-Charlotte Jonckheere, Rik Lories, Peter Hoet, Erik Verbeken, Jeroen Vanoirbeek, Greetje Vande Velde

Abstract

Idiopathic pulmonary fibrosis is an interstitial lung disease with limited knowledge of the aetiology. Despite multiple clinical trials and efforts to develop effective therapeutics the past years, only two drugs made it to the market: Nintedanib and Pirfenidone, with varying degrees of success. To improve/extend the tools for preclinical evaluation of idiopathic fibrosis therapeutics, we evaluated the anti-inflammatory and anti-fibrotic characteristics of Nintedanib using a longitudinal *in vivo* μCT approach. Mice received a single oropharyngeal instillation with crystalline silica particles (2.5 mg/animal) or saline to induce pulmonary fibrosis. Two treatment protocols (daily Nintedanib treatment by oral gavage, 100 mg/kg body weight) were tested, an anti-inflammatory and anti-fibrosis, starting one and five weeks after silica instillation, respectively. Mice were longitudinally monitored with high-resolution μCT to evaluate disease onset, progression and therapeutic effects. Nine weeks after silica instillation, we assessed lung function, inflammation and fibrosis in a cross-sectional manner. After silica-instillation, the non-aerated lung volume, a marker for early onset and progression of disease, increased up to 150%, where after it decreased after administering Nintedanib in both the anti-inflammatory and anti-fibrosis protocol. Nintedanib did not influence the total and aerated lung volume in the anti-inflammatory protocol, whereas it did influence both the total and aerated volumes in the anti-fibrosis protocol as confirmed by end-stage lung function measurements. Yet, lung inflammation (BAL neutrophils) was not changed by Nintedanib treatment. Our data indicates that Nintedanib treatment onset, both at an early moment as later in the disease, influences disease progression, based on lung volumes, but does not influence ongoing lung inflammation. Additionally, our imaging readouts are in agreement with *ex vivo* endpoint measurements indicating that μCT in combination with a stable inflammatory and fibrosis mouse model can contribute substantially to preclinical anti-fibrotic drug screening.

Introduction

Idiopathic pulmonary fibrosis (IPF) is a chronic progressive interstitial lung disease (ILD) with limited knowledge on the aetiology. It is one of the most common forms of ILD, with an incidence of 3 to 9 cases per 100.000 person/year [11,12,14]. The hypothesis is that repeated injury and genetic predisposition are the two most important drivers in the development of pulmonary fibrosis [26]. Currently, Nintedanib and Pirfenidone are the only two available drugs on the market for IPF, which slow down the progressive reduction in forced vital capacity in randomized controlled trial [15,16,50].

Nintedanib (BIBF 1120) is a tyrosine kinase inhibitor and targets the fibroblast growth factor receptor (FGFR) 1, 2 and 3, platelet derived growth factor receptor (PDGFR) α and β and vascular endothelial growth factor receptor (VEGFR) 1, 2 and 3 [50,51]. Previous *in vivo* studies showed the anti-inflammatory and anti-fibrotic characteristics of Nintedanib in different mouse models of pulmonary fibrosis [186-188], with a focus on endpoint measurements, which resulted in limited information different from clinical readouts, with no knowledge on disease onset, progression and therapeutic effects.

Micro-computed tomography (µCT) is an established technique to longitudinally evaluate the disease state of the lungs in experimental rodent models [75,111,146,189]. Multiple studies have shown the applicability of µCT to visualise end-stage therapeutic efficacy in pulmonary fibrosis rodent models [190-194]. However, longitudinal evaluation using µCT in these models is almost non-existing. Using µCT in a longitudinal fashion, instead of only end-stage to evaluate the differences between treated and untreated animals, allows assessing the early onset, progression and possible resolving of lung disease, in therapy testing in preclinical *in vivo* models. Applying lung disease µCT in a longitudinal fashion would facilitate some more in-depth analysis of disease burden and therapeutic efficacy at the level of individual animals. Currently, most of the times only the mean lung density as a measure of disease is reported, but it is known that this is influenced by total lung volume [89]. A more detailed analysis of the µCT images, including aerated, non-aerated and total lung volume is essential to retrieve more relevant data on disease progression and treatment effects [75]. The selected use of mean lung density can lead to an overestimation of disease burden thereby misinterpreting treatment.

In most preclinical therapy studies, treatment is applied in a prophylactic manner, meaning, before or at the time of disease induction. This type of experimental set-up allows making conclusion on disease onset or prevention of onset, but does not allow conclusion on true anti-inflammatory nor anti-fibrotic responses. Moreover, it does not resemble the clinical situation. The currently often-used single-shot bleomycin pulmonary fibrosis model does not allow a true therapeutic experimental setup.

We hypothesize that µCT in combination with a stable inflammatory and fibrosis mouse model can contribute substantially to test preclinical drug screening. In this study, we evaluated a commercially available therapeutic (Nintedanib) on its anti-inflammatory and anti-fibrotic characteristics in a mouse model of silica-induced fibrosis by *in vivo* µCT and other golden standard end-stage analyses.

Materials and methods

Animal model

All animal experiments were carried out in compliance with national and European regulations and were approved by the animal ethics committee of KU Leuven (P057/2018). Mice were kept in a conventional animal facility with individually ventilated cages and free access to food and water. Eight-week-old male C57Bl/6JRj mice (Janvier, Le Genest, France) were oropharyngeally instilled with crystalline silica particles (2.5 mg/animal), kindly provided by B Fubini (Facoltà di Farmacia, Università di Torino, Italy), or saline (NaCl 0.9%). Silica particles were baked for 2 hours at 180°C and suspended in saline with a concentration of 0.0625 mg/μL. Next, the solution was probe sonicated for 16 minutes. Animals were anesthetized by inhalation of 5% isoflurane (Piramal Healthycare, Morpeth, Northumberlang, United Kingdom) in 100% oxygen for 2 minutes. By simultaneously holding the tongue and covering the nose, animals were oropharyngeal instilled with 40 μL of silica/saline [63,167]. Mice were weighted daily. The total number of animals used in this experiment was 43.

Therapy

The anti-inflammatory and anti-fibrosis therapy was started 1 and 5 weeks, respectively, after administration of silica particle suspension or saline (Figure 1). Nintedanib (Boehringer Ingelheim, Germany) or milliQ as sham treatment were administered daily via oral gavage (100 mg/kg body weight). Nintedanib solution was prepared fresh twice per week. Nintedanib was dissolved in milliQ at 50°C (final concentration of 10 mg/mL).
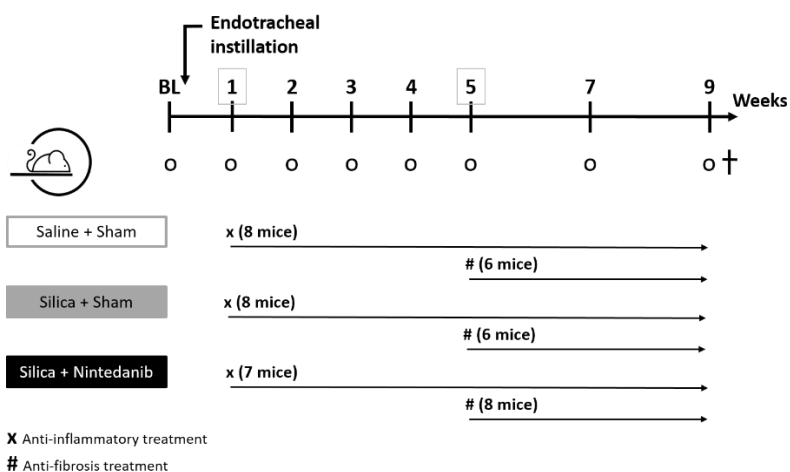

Figure 1: experimental design.
'o' indicates a μCT scan. Nintedanib was tested in an anti-inflammatory (x) and anti-fibrosis manner (#), with initiation of treatment (daily oral gavage, 100 mg/kg) starting on week 1 (total treatment duration of 8 weeks) or week 5 (total treatment duration of 4 weeks), respectively. The number of animals per group is indicated by an 'x' (anti-inflammatory treatment) or '#' (anti-fibrosis treatment). 9 weeks post silica exposure; all animals were sacrificed to obtain lung function and *ex vivo* measurements.

Experimental design

Mice were randomly divided over the treatment groups. All mice were scanned at baseline and afterwards weekly for the first 5 weeks, from then on every two weeks until the end. Ad day 63, (9 weeks after induction), animals were sacrificed for *ex vivo* endpoint measurements (Figure 1).

Micro-computed tomography

Mice were anesthetized by inhalation of 1.5-2% isoflurane in 100% oxygen and scanned in supine position using a dedicated *in vivo* μCT scanner (Skyscan 1278, Bruker μCT, Kontich, Belgium). The following parameters were used: 50 kVp X-ray source voltage and 346 μA current combined with a composite X-ray filter of 1 mm aluminium, 150 ms exposure time per projection, acquiring 3 projections per view with 0.9° increments over a total angle of 220°, and 10 cm field of view covering the whole body producing reconstructed 3D data sets with 50 μm isotropic reconstructed voxel size [75,189,195].

Image analysis

Software provided by the manufacturer (TSort, NRecon, DataViewer, and CTan) was used to retrospectively gate, reconstruct, visualize, and process μCT data as described previously [89,128]. For Hounsfield unit (HU) calibration, a phantom was scanned consisting of an air-filled 1.5 mL tube inside a water-filled 50 mL tube. Based on full stack histograms of a volume-of-interest (VOI) containing only water or air, the main grayscale index of water (127) was set at 0 HU and grayscale index of air (6) at -1000 HU. Quantification of the mean lung density, non-aerated lung volume, aerated lung volume, and total lung volume was carried out for a VOI covering the lung, manually delineated on the coronal μCT images, avoiding the heart and main blood vessels. When defining the VOI covering the lungs, we define the top of the lungs by the CT section defined by the point where the clavicle touches the sternum and the bottom by a plane under the lungs through the liver. The threshold used to distinguish aerated from non-aerated lung tissue volume was manually set at -183 HU and kept constant for all data sets.

Lung function

Lung function was assessed at day 63, 9 weeks after silica instillation using the flexiVent FX system (SCIREQ, EMKA Technologies, Montreal, Canada). Briefly, the mice were anesthetized with an intraperitoneal injection of pentobarbital (120 mg/kg BW, Dolethal). Once sufficiently anesthetized, a tracheotomy was performed to insert an 18-gauge metal cannula. Mice were quasi-sinusoidal ventilated with a tidal volume of 10 mL/kg and a frequency of 150 breaths/min to mimic spontaneous

breathing [166]. An FX1 module with a negative pressure forced expiration (NPFE) extension was used, in combination with the flexiware 7.6 software.

At the start of the measurements, two successive deep inflations were applied to maximally inflate the lungs to a pressure of 30 cmH2O in order to open the lungs and determine the inspiratory capacity (IC). Between each set of perturbation, a deep inflation was performed to normalize the lungs. The forced oscillation perturbation 'Prime-3' (P3) which generates forced oscillations with a frequency between 1-20.5 Hz during 3 sec, was executed at least three times. The reported central airway resistance (Rn), tissue damping (G), tissue elasticity (H) and tissue hysteresivity (eta = G/H) are the average of three accepted measurements (COD>0.9). In between, a NPFE (negative pressure forced expiratory flow) perturbation was performed to measure the peak expiratory flow (PEF), forced vital capacity (FVC) and forced expiratory volume in 0.1 seconds (FEV0.1). Reported values are the average of three accepted measurements (COD>0.9) for each individual data point.

Inflammatory and permeability evaluations

Immediately after the lung function assesment, whole blood was collected and centrifuged (4 °C, 10 min) to isolate the serum, in which we measured surfactant protein (SP)-D concentration by ELISA (Duoset ELISA, R&D Systems Inc., DY6839-05) according to the manufacturers' instructions. The whole lung was lavaged three times *in situ* with 0.7 mL sterile saline (0.9% NaCl), the collected fluid pooled and analysed for total and differential cell counts. The total number of cells in the BAL fluid was counted using a Bürker hemocytometer. Subsequently the bronchoalveolar lavage (BAL) fluid was centrifuged (1000 g, 4 °C, 10 min) and the supernatant collected and frozen (-80 °C) until further analysis. For differential cell counts, the cells were resuspended in 1 mL saline (0.9% NaCl), of which 250 µL of the resuspended cells were spun (300 g, 4 °C, 6 min; Cytospin 3, Shandon, TechGen, Zellik, Belgium) onto microscope slices, air-dried and stained (Diff-Quik method, Medical Diagnostics, Düdingen, Germany). For each sample, 200 cells were counted to quantify the number of macrophages, eosinophils, neutrophils and lymphocytes. Protein concentration was determined on the cell-free undiluted BAL supernatant using the Bradford method with bovine serum albumin as a standard.

Histopathological and histochemical analysis

The left lung lobe was manually inflated until visually judged total lung capacity was reached, fixed with 4% paraformaldehyde and paraffin embedded. Five µm sagittal sections were stained with haematoxylin-eosin (H&E). H&E stained sections were blindly scored from 0 to 3 on both the alveolar parenchyma and bronchovascular bundle for lymphocytes, neutrophils, lymphoid follicles,

macrophages/macrophage crystals, granuloma formation and collagen formation by an experienced pathologist.

The right lung lobes were clamped, collected and stored at -80 °C for hydroxyproline quantification as previously described [154]. In short, right lung lobes were hydrolysed for 3 hours in 6M HCl at 120 °C. After cooling down for 15 minutes, the pH was neutralized (pH 6–7) using 500 ml NaOH. Free hydroxyproline was oxidized with chloramine-T for 20 minutes after which the oxidation reaction was stopped using 70% perchloric acid. Ehrlich's reagent was added, and samples were heated for 20 minutes in a 60 °C water bath. After cooling down, absorbance was measured at 570 nm and concentrations were calculated based on a standard curve.

Statistical analysis

The data were analysed using GraphPad Prism (version 8.02. Graphpad Software Inc., San Diego, USA). The data are presented as mean with standard deviation (SD) or as mean with individual values. Normal distribution was assessed by the Kolmogorov-Smirnov test. Data of longitudinal μCT-derived biomarkers (with missing values and an unbalanced design; mean lung density, total lung volume, non-aerated lung volume and aerated lung volume) were analysed using a mixed-effects model with Geisser-Greenhouse correction, for assessing the interaction between time and treatment. Data of endpoint measurements were analysed by Kruskal-Wallis and Dunn's *post hoc* multiple comparison test was used. For the number of animals per group, we refer to Figure 1. For all tests, statistical significance was assumed when * p-value < 0.05; ** p-value < 0.01 and *** p-value < 0.001.

Results

Establishment of a subtle silicosis model

In this study, we dosed the mice with half of the concentration (2.5 mg in 40 µL) compared to our previously published silica-induced pulmonary fibrosis model[189], aiming at a more subtle induction of fibrosis, similar to other models [186]. Mice were scanned at baseline, then instilled with silica particles or saline and assessed longitudinally for 9 weeks with high-resolution low-dose µCT (Figure 1). Silica instillation caused an immediately weight loss compared to the saline instillation, but the mice recovered within the first week (Figure 2). In the anti-inflammatory set-up, Nintedanib treatment was started 1 week after silica instillation, while in the anti-fibrosis set-up, Nintedanib treatment started 5 weeks post silica exposure (Figure 1). Mice that received Nintedanib from week one appeared to stagnate in weight gain, compared to both saline groups (Figure 2A), while mice that received Nintedanib from week 5, lost some body weight on week 7 and 9 (Figure 2B).
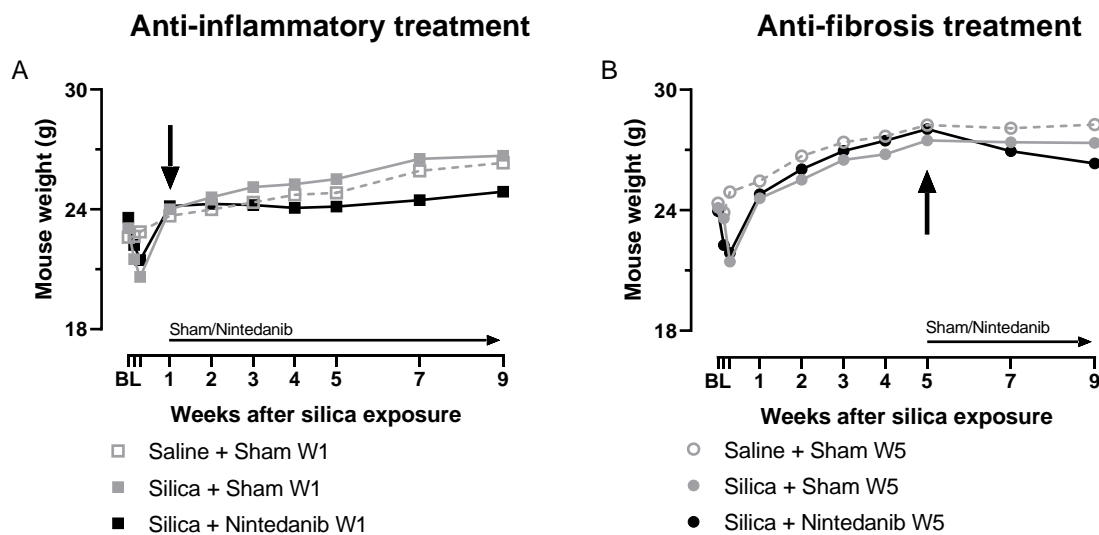

Figure 2: effect of silica exposure and Nintedanib treatment on mouse body weight.
Every animal was weighted daily during the whole experiment. Data are presented as mean. Mixed-effects model was used to compare the different groups. For post-hoc testing, Sidak's multiple comparison was used to evaluate Saline + Sham vs Silica + Sham, Saline + Sham vs Silica + Nintedanib and Silica + Sham vs Silica + Nintedanib. No significant differences were found between groups. The arrows indicate the start of the Nintedanib or sham treatment.

To follow up and evaluate disease onset and treatment effects, we weekly performed µCT. Figure 3 shows representative images at week 9 after silica instillation. Visual inspection of the µCT images revealed changes in the lungs after silica exposure and Nintedanib treatment, both in after early onset of treatment (week 1) and late onset treatment (week 5) (Figure 3).
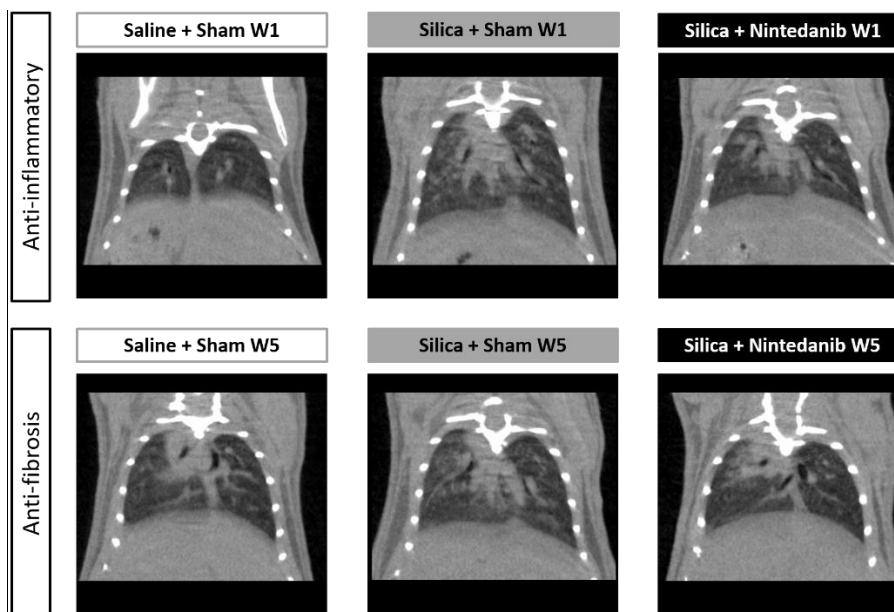
Figure 3: µCT visualizes inflammatory and fibrotic processes after silica administration and Nintedanib treatment. Representative coronal images of one animal per group at endpoint (9 weeks after silica instillation).

To further objectify the visual inspection of the µCT scans, we quantified different µCT-derived biomarkers to evaluate disease onset and progression after silica-instillation. The non-aerated lung volume, which is a direct measurement for the extent of inflammation and fibrotic processes present in the lungs [89,189], was significantly increased compared to the baseline values and remained stably elevated after silica exposure in both the anti-inflammatory and anti-fibrosis treatment groups indicating disease induction (Figure 4A-B). The aerated lung volume and total lung volume both increased after silica instillation (Figure 4C, D, E, F).

Evaluating µCT-derived biomarkers for therapeutic efficacy testing

After the start of Nintedanib treatment, both in the anti-inflammatory (at week 1, black squares figure 4A) and anti-fibrosis group (at week 5, black dots figure 4B), the non-aerated lung volume decreased but remained elevated above normal control level. In the anti-inflammatory treatment experimental group, Nintedanib administration did not influence the aerated lung volume nor the total lung volume (dark grey squares, figure 4C, E). In the anti-fibrosis treatment group, the aerated and total lung volume is increased at week 7, 2 weeks after the start of Nintedanib administration and remained elevated compared to control levels (dark grey dots, figure 4D, F). The mean aerated lung density is the density of the aerated lung compartment. This density decreased after silica instillation in both the anti-inflammatory and anti-fibrosis treatment experiment. After starting the Nintedanib treatment, this decreased density was similar to the complete control group in the anti-inflammatory experiment (Figure 4H). In the anti-fibrosis experiment, the mean aerated lung density increased substantially in the mice receiving Nintedanib treatment from week 5 on (Figure 4I).
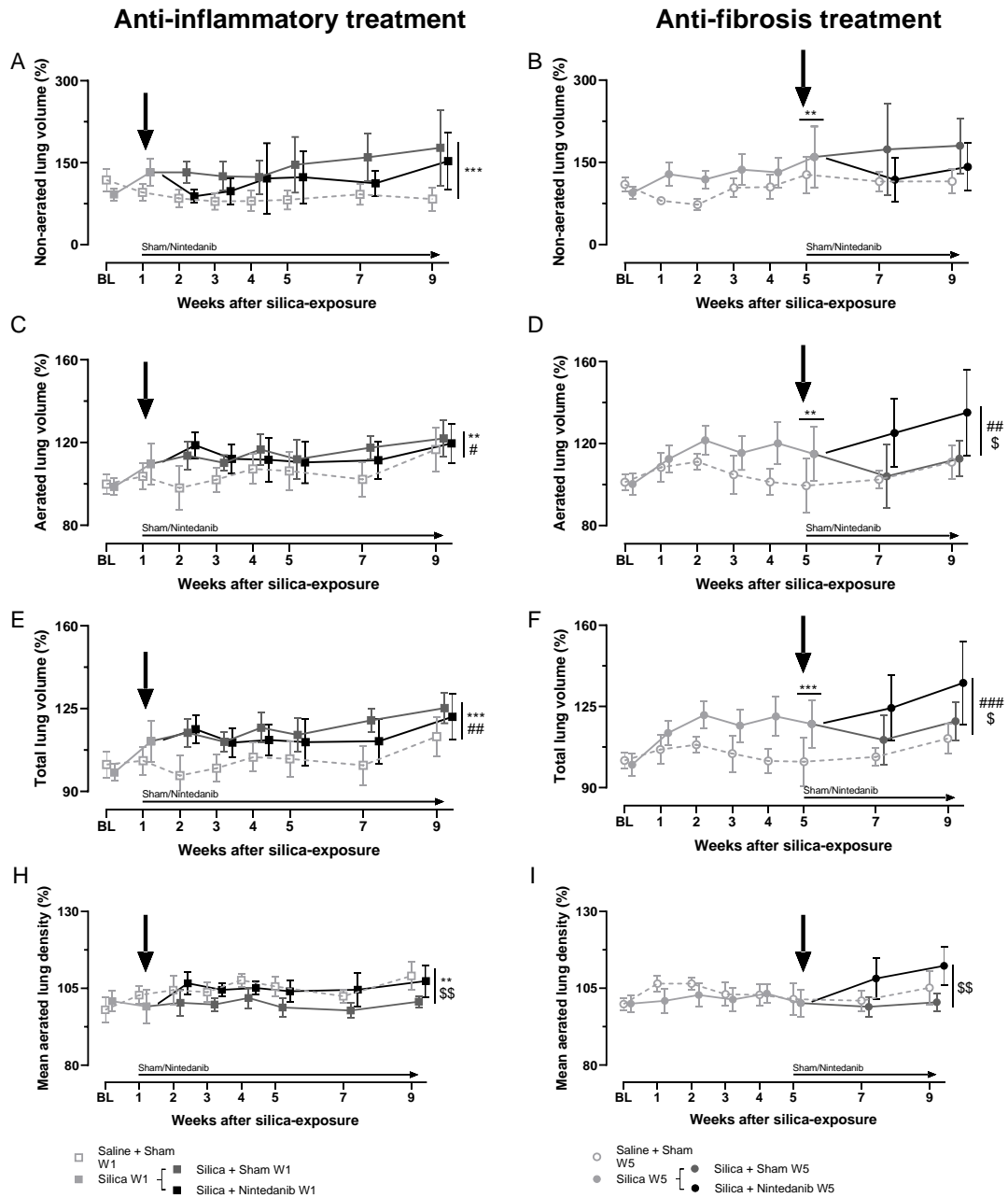
Figure 4: anti-inflammatory and anti-fibrosis treatment effects of Nintedanib quantified by µCT.
µCT-derived biomarkers follow up disease onset, progression and therapeutic effects in silica-instilled animals. All biomarkers are given as the percentage of increase compared to baseline: (A-B) non-aerated lung volume (%) (C-D) aerated lung volume (%) (E-F) total lung volume (%) (G-H) mean aerated lung density (%). Data are presented as mean ± SD. Note the different scaling of y-axis. First, we evaluated silica-induction: Saline + Sham W1 (n = 8) versus Silica W1 (n = 15) from baseline to week 1 and Saline + Sham W5 (n = 6) versus Silica W5 (n = 14) from baseline to week 5. Significance indicated by * above graph. Second, we evaluated treatment effects: Saline + Sham W1 (n = 8) versus Silica + Sham W1 (n = 8) versus Silica + Nintedanib W1 (n = 7) from week 2 to week 9 and Saline + Sham W5 (n = 6) versus Silica + Sham W5 (n = 8) versus Silica + Nintedanib W5 (n = 8) from week 7 to week 9. Mixed-effects model was used. For post-hoc tests, Sidak's multiple comparison was used. Significance indicated at right side of graph: Saline vs Silica + Sham by *, Saline vs Silica + Nintedanib by # and Silica + Sham vs Silica + Nintedanib by $. Single symbol: p value < 0.05, double symbols: p value < 0.01, triple symbols: p value < 0.001. BL=baseline. The arrows indicate the start of the Nintedanib treatment.

End-stage, *ex vivo* measurements and agreement with μCT data

At experimental endpoint, we performed lung function and *ex vivo* measurements to validate our *in vivo* findings. Figure 5A and C show the invasive lung function assessment at day 63. Silica instillation did not significantly influence the inspiratory capacity (IC) and forced expiratory volume in 0.1 sec (FEV$_{0.1}$) (Figure 5A, C), nor tissue damping (G), tissue elasticity (H) and tissue hysteresivity (G/H) corresponding to a more sub significant silicosis mouse model (data not shown). Yet, Nintedanib treatment started one week after silica instillation significantly increased the IC, compared to the complete control group. When Nintedanib treatment was started 5 weeks after silica instillation, both IC and FEV$_{0.1}$ were significantly higher compared to both other groups.
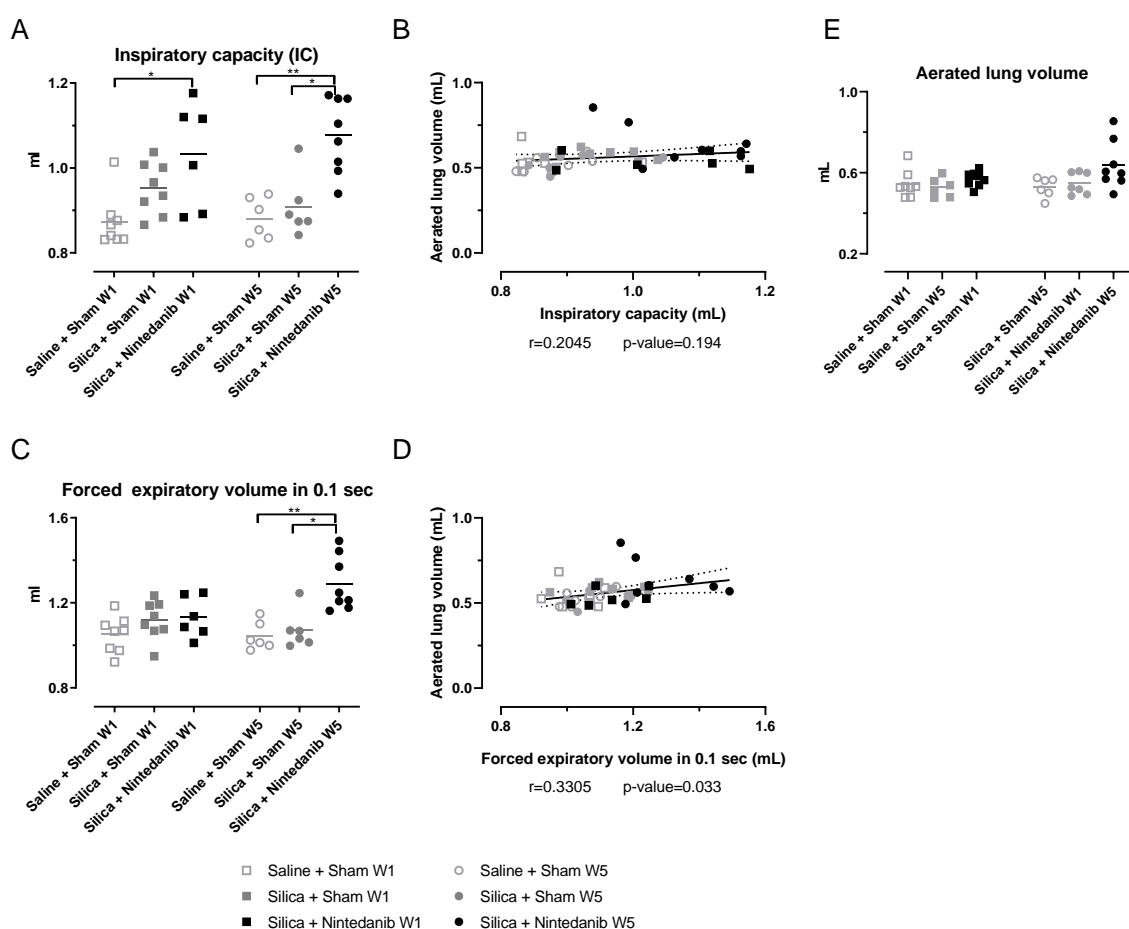

Figure 5: nintedanib enlarges the lungs observed by an increased inspiratory capacity and FEV0.1 on lung function measures.

9 weeks after silica exposure and Nintedanib treatment, animals were sacrificed to obtain lung function measurements. Nintedanib induced an increased (A) inspiratory capacity (mL), (C) forced expiratory volume in 0.1 sec. (B, D) correlations between μCT-derived biomarkers and lung function measurements. (E) μCT-derived aerated lung volume at endpoint (mL). Data are presented as mean and individual values. Kruskal-Wallis test was used to compare control and disease animals in the anti-inflammatory and anti-fibrosis group with the following number of animals: 8 Saline + Sham W1, 8 Silica + Sham W1, 7 Silica + Nintedanib W1 and 6 Saline + Sham W5, 6 Silica + Sham W5, 8 Silica + Nintedanib W5. For *post hoc* tests, a Dunn's multiple comparison test was used. For correlation analysis, the Pearson correlation coefficient was calculated. * p value < 0.05, ** p value < 0.01.

In a second step, we try to find correlations and agreement between the last *in vivo* μCT image and the *ex vivo* lung function measurements. No correlations were found between *in vivo* μCT biomarkers and *ex vivo* lung function measurements, although the μCT-derived aerated lung volume showed a similar trend on a qualitative level as the IC and $FEV_{0.1}$ (Figure 5B, D, E).

To further validate our *in vivo* findings, we measured the collagen content and inflammatory readouts. The OH-proline content in lung tissue, which tended to be a bit higher in the silica instilled groups, not reaching statistical significance, possibly pointing to a mild silicosis induction (Figure 6A). Although there were no differences in absolute OH-proline concentrations, we did find that the OH-proline concentrations correlated with the non-aerated lung volume measured with the μCT (r=0.4426, p-value=0.003) (Figure 6B). Also for the total protein concentration in BAL, a measure for epithelial damage, no differences were found between the treatment groups (Figure 6C), yet again we found a correlation with the non-aerated lung volume as measured by μCT (r=0.3790, p-value=0.013) (Figure 6D). The protein surfactant D concentrations in serum were increased after silica instillation, which is a proxy for epithelial damage. Nintedanib treatment at week 1, nor at week 5, could reverse this effect (Figure 6E). The SpD concentration showed significant correlation with the non-aerated lung volume measured with μCT (r=0.6337, p-value<0.001) (Figure 6F). Nintedanib treatment, started at week 1, nor week 5 attenuated the BAL neutrophilic inflammation induced by silica instillation (Figure 6G). In addition, the BAL neutrophils showed a high correlation with the non-aerated lung volume measured with μCT (r=0.5663, p-value<0.001) (Figure 6H).

Figure 7 shows an overview of the histological abnormalities that are found in the bronchovascular bundle, and scored in a semi-quantitative way. The histological quantification revealed significantly increased lymphocytic inflammation and lymphoid follicles 9 weeks after silica exposure (Figure 7A, C), with signs of neutrophils, granuloma and collagen formation (Figure 7B, D, E). No necrosis was found (data not shown). Nintedanib treatment started at week 1, nor at week 5 reverse the effects of silica exposure observed on histology. We observed similar findings in the alveolar parenchyma (Figure S1). Silica instillation increased lymphocytes and macrophages, with signs of neutrophils, lymphoid follicles, granuloma and collagen formation. Nintedanib did not attenuate these observations.
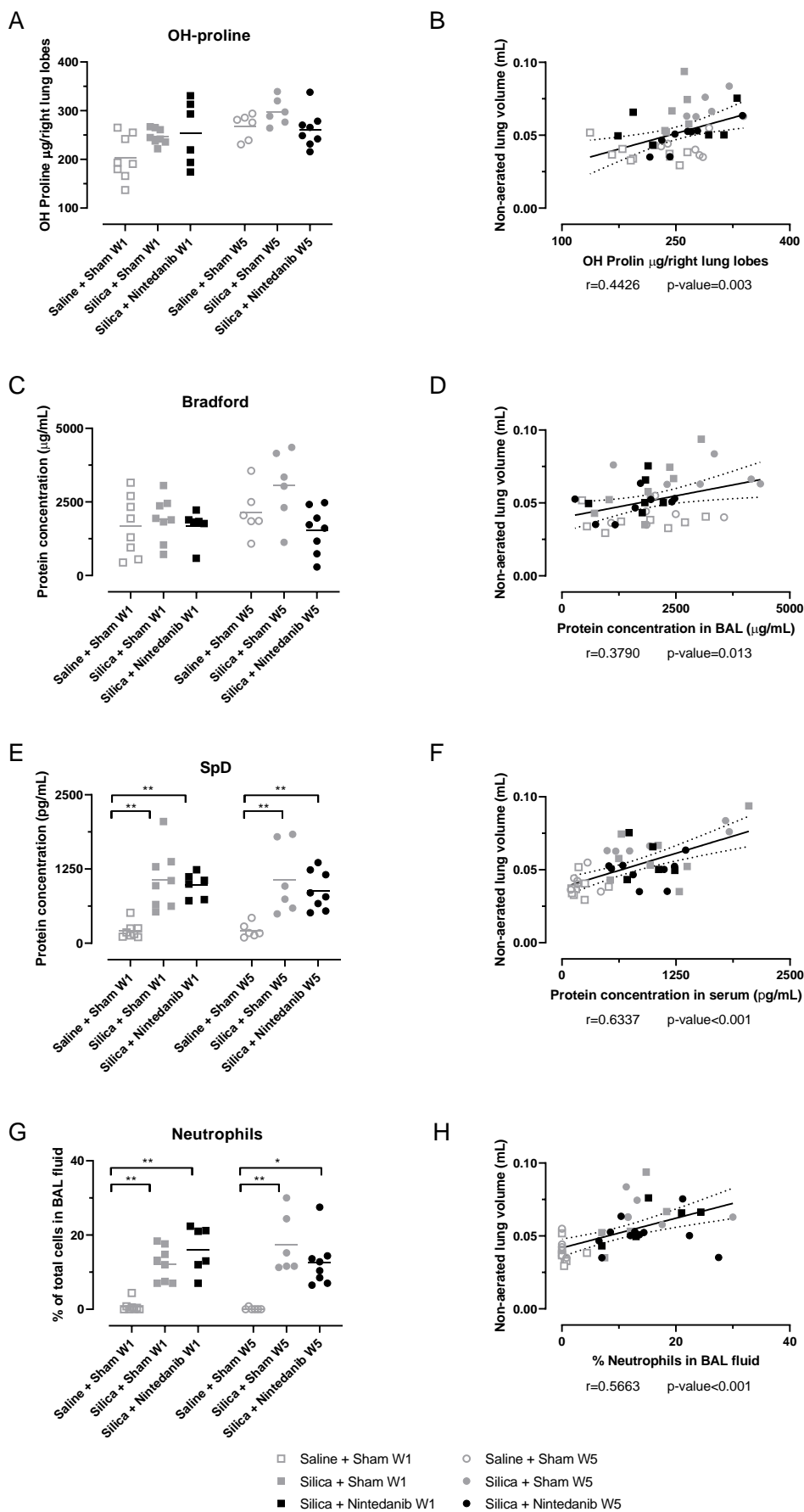
Figure 6: nintedanib has a limited effect on collagen content and SpD concentration in serum and the neutrophilic inflammation induced by silica instillation.

9 weeks after silica exposure and Nintedanib treatment, animals were sacrificed to obtain *ex vivo* endpoint measurements. Nintedanib did not change (A) the collagen content measured by a hydroxyproline assay, (C) protein concentration in the BAL fluid and (E) SpD concentration in serum. Nor did it influence the (G) neutrophilic inflammation induced by silica instillation. (B-D-F-H) correlations between *in vivo* µCT-derived biomarkers and *ex vivo* measurements. Data are presented as mean and individual values. Kruskal-Wallis test was used to compare the groups in the anti-inflammatory and anti-fibrosis group with the following number of animals: 8 Saline + Sham W1, 8 Silica + Sham W1, 7 Silica + Nintedanib W1 and 6 Saline + Sham W5, 6 Silica + Sham W5, 8 Silica + Nintedanib W5. For *post hoc* tests, a Dunn's multiple comparison test was used. For correlation analysis, the Pearson correlation coefficient was calculated. * p value < 0.05 ** p value < 0.01 *** p value < 0.001.
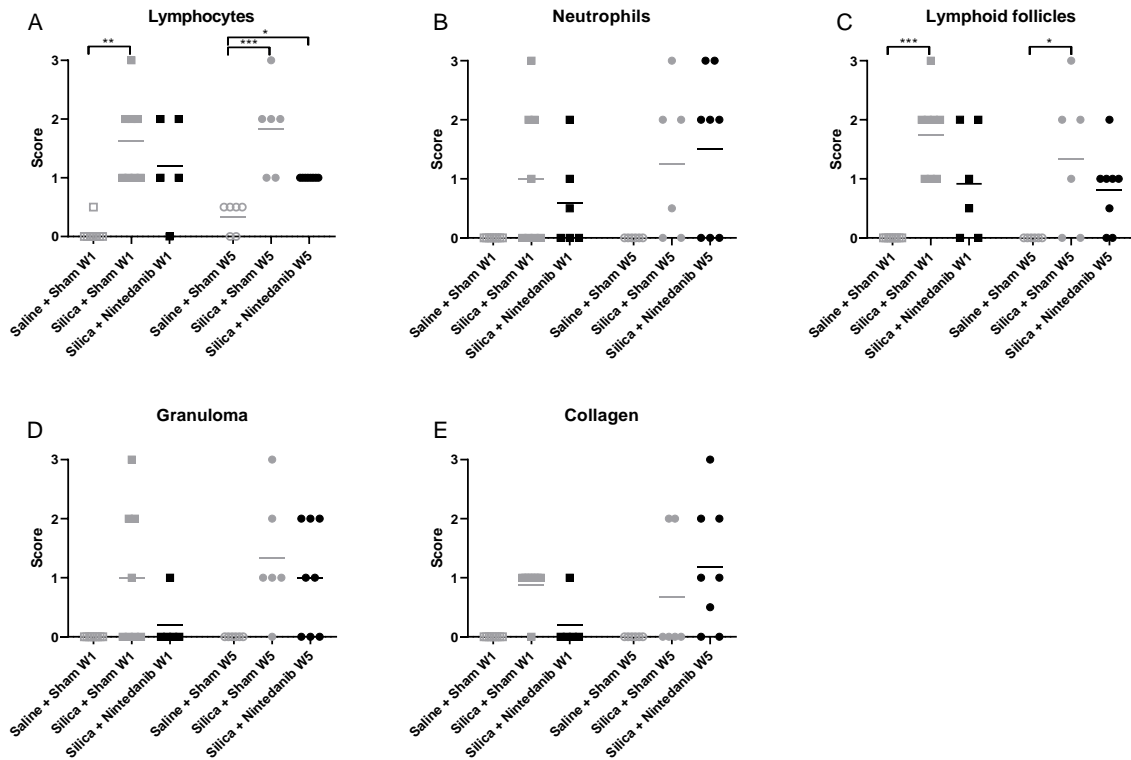
Figure 7: histology confirms *ex vivo* findings: Nintedanib has no influence on neutrophilic inflammation, nor on granuloma formation or collagen content of the bronchovascular bundle.

9 weeks after silica exposure and Nintedanib treatment, animals were sacrificed to obtain *ex vivo* endpoint measurements. Scoring was performed on H&E stained slices of the left lung lobe by a pathologist: (A) lymphocytes, (B) neutrophils, (C) lymphoid follicles, (D) granuloma formation and (E) collagen formation. Data are presented as mean and individual values. Kruskal-Wallis test was used to compare the groups in the anti-inflammatory and anti-fibrosis group with the following number of animals: 8 Saline + Sham W1, 8 Silica + Sham W1, 7 Silica + Nintedanib W1 and 6 Saline + Sham W5, 6 Silica + Sham W5, 8 Silica + Nintedanib W5. For *post hoc* tests, a Dunn's multiple comparison test was used. * p value < 0.05 ** p-value < 0.01 *** p value < 0.001.

Discussion

In this study, we evaluated the anti-inflammatory and anti-fibrotic properties of Nintedanib in a mouse model of stable silica-induced fibrosis, in combination with the potential of µCT to serve as a preclinical tool to investigate the efficacy of disease improvement. We applied Nintedanib, an anti-fibrotic therapeutic available on the market for IPF, in a silicosis mouse model and monitored the mice for 9 weeks. Two different treatment regimens were tested: (1) an anti-inflammatory experiment, in which we started Nintedanib treatment 1 week after silica exposure when a high inflammatory phase is present and (2) an anti-fibrosis experiment, in which we started Nintedanib treatment 5 weeks after silica exposure, when both inflammation and fibrosis are present. Our data show that Nintedanib treatment slightly decreased the non-aerated lung volume in both treatment regimes, while it increased the end-expiratory aerated and total lung volume as assessed by µCT, which was confirmed by *ex vivo* IC and $FEV_{0.1}$ lung function measurements.

Based on the initial weight loss (immediately after silica instillation) and the increased non-aerated lung volume, we can conclude that disease induction was persistent in all silica-instilled mice. Notably, in this study, we only instilled 0.0625 mg/µL silica particles per animal, which is half of the concentration compared to our previous study in chapter 4 (0.125 mg/µL silica particles)[189], thereby limiting the severity of the lung disease as seen by the limited increase in collagen content on histology and only slightly increased OH-proline contents. The choice for the lower concentration was made because the higher concentration from the previous study led to histological changes that were less relevant for human silicosis [189]. The dose used in chapter 4 led to a severe model where therapeutics would possible only have minor effects. Yet, this makes the interpretation of the current data and the therapeutic effects more challenging. All effect sizes seen in the current study are less pronounced in comparison with the higher dose model. It remains a question how the treatment effect would have influenced the more severe inflammation and fibrosis induced by 5 mg of silica in 40 µL. Accordingly, the concentration and dosing regimen of Nintedanib can be debated. In the studies of Wollin *et al.*, Ninetedanib was administered twice daily, in a 50 mg/kg concentration, where we gave once daily 100 mg/kg concentration [186]. Yet, although OH-proline did not differ in absolute values between the treatment groups, it did correlate well at the level of the individual animal with the non-aerated lung volume as measured by the µCT, suggesting an ongoing profibrotic response to the instilled silica particles.

The decrease in non-aerated lung volume, might be indicative for a potential anti-inflammatory and anti-fibrotic properties of Nintedanib detected by µCT. The µCT analysis also revealed the ongoing increase in total and aerated lung volume in the silica-instilled group that received Nintedanib

treatment from week 5 onwards. This increase in lung volume was confirmed by the lung function measurements (increased IC and $FEV_{0.1}$). It is not the first time that the phenomena of increasing aerated and total lung volume is observed. It occurs in several other lung disease models and in the silica-induced pulmonary fibrosis model itself [89,100,184,185,189]. A possible explanation is a hyper compensation response to the excessive loss of air spaces. In this study, we cannot conclude whether the ongoing increase after Nintedanib administration starting at week 5 is due to harmful effects or functional improvements. Moreover, the observed increase in lung function does not necessarily imply clinical improvement of the animals. The inclusion of an extra treatment group, being saline instillation in combination with Nintedanib treatment would give more insights in the effect of Nintedanib on the lung independent from the profibrotic context. The Nintedanib dose given daily, 100 mg/kg, was relatively high and resulted in a slower gain of body weight in groups receiving treatment but overall the treatment was well tolerated by the animals.

In an anti-fibrotic context, studies (from other groups) including µCT are rare [75,89,194]. Due to its non-invasiveness, it is an ideal candidate for providing information on the amount of fibrosis present when administering the therapeutic. De Ruysscher et al. concluded that the mean lung density was not able to capture differences induced by Nintedanib treatment, their explanation being that the CT density is mostly affected by alveolar wall thickness and macrophage infiltration, both not affected by Nintedanib [194]. However, it is important to note that the mean lung density provides information on the bulk changes in the lungs; the aerated and non-aerated compartment together. As observed in this study and previously shown, other biomarkers would be more accurate to provide information on what truly happens inside the lungs [89,189].

In a previous study, Nintedanib was able to reduce the collagen content, granuloma formation, lymphocyte and neutrophil count in a silica-induced fibrosis model [186]. These effects of Nintedanib were seen when it was administered in a preventive strategy, meaning before and immediately after administering silica particles. This experimental strategy also resulted in less pronounced disease symptoms, compared to a real therapeutic regimen. In our study, Nintedanib did not reduce the lung inflammation as shown by the BAL neutrophilic inflammation and the interstitial lymphocytic inflammation. In addition, the epithelial damage found in our model was also not reversed by Nintedanib treatment [64,182]. Yet, this was to be expected, because Nintedanib's mode of action as a tyrosine kinase inhibitor which mostly interferes with central processes such as fibroblast proliferation, migration and differentiation [51]. Reversing the epithelial damage when silica particles remain present was not possible by Nintedanib. When silica particles remain present, a constant trigger for the

immune system to produce neutrophils keep on being active. Yet, we expected to find an effect of Nintedanib on the number of neutrophils in the lungs, as previously found [186].

To conclude, although Nintedanib only showed a small treatment effect in the context of a silicosis mouse model of limited severity, it was picked up by *in vivo* μCT with good agreement between *in vivo* μCT biomarkers and *ex vivo* readouts (i.e. flexiVent, histology and inflammatory markers). Additional evaluation of μCT with an improved subtle silicosis mouse model and treatment regimen of Nintedanib would possibly provide further evidence for the routine implementation of μCT in a preclinical anti-fibrotic evaluation platform. The combination of a stable and long-term pulmonary fibrosis mouse model with longitudinal imaging-derived biomarkers are important add-ons for a toolbox in preclinical treatment efficacy studies.

Acknowledgements

Conflict of interest

All authors declare no conflict of interest.

Supplementary figures
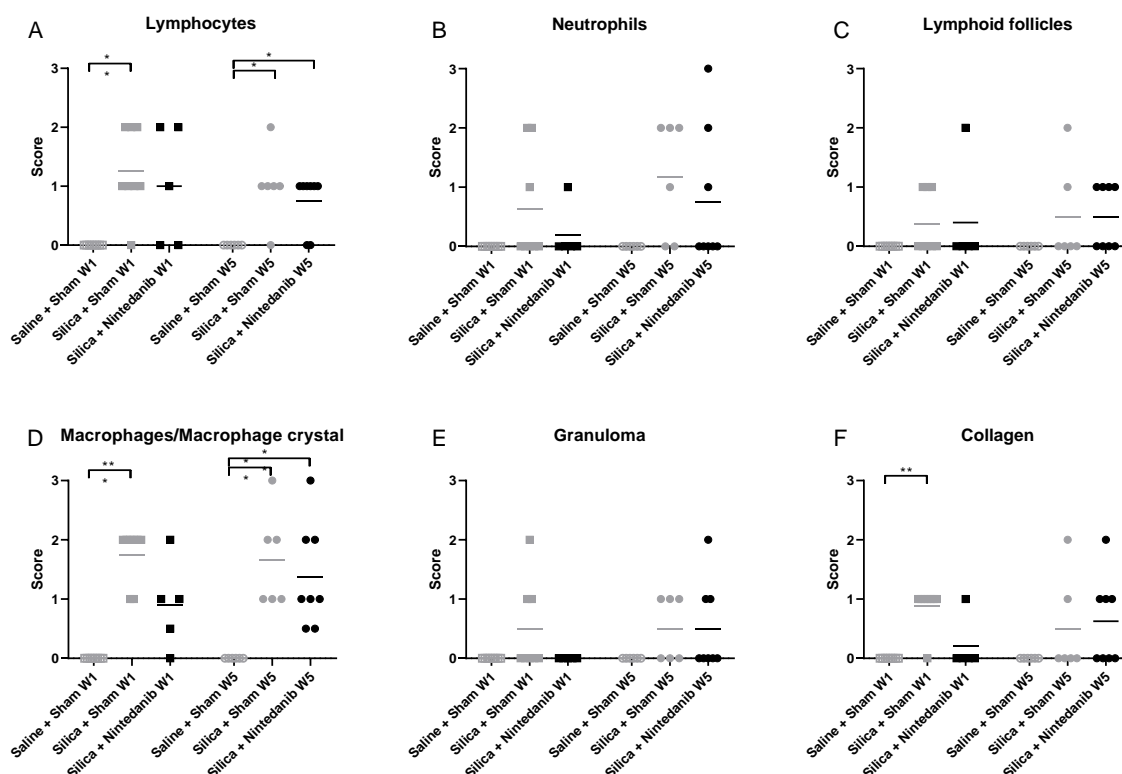
Figure S1: histological results of the alveolar parenchym.

9 weeks after silica exposure and Nintedanib treatment, animals were sacrificed to obtain *ex vivo* endpoint measurements. Scoring (from 0 to 3) was performed on H&E stained slices of the left lung lobe by a pathologist: (A) lymphocytes, (B) neutrophils, (C) lymphoid follicles, (D) macrophages/macrophage crystals, (E) granoluma formation and (F) collagen formation. Data are presented as mean and individual values. Kruskal-Wallis test was used to compare the groups in the anti-inflammatory and anti-fibrotic group with the following number of animals: 8 Saline + Sham W1, 8 Silica + Sham W1, 7 Silica + Nintedanib W1 and 6 Saline + Sham W5, 6 Silica + Sham W5, 8 Silica + Nintedanib W5. For *post hoc* tests, a Dunn's multiple comparison test was used. * p value < 0.05 ** p-value < 0.01 *** p value < 0.001.

Chapter 6

The Centre of Tidal Volume, a novel μCT-derived functional lung biomarker for preclinical research

Kaat Dekoster, Ellen De Langhe, Sofie Van den Broucke, Peter Hoet, Rik Lories, Jeroen Vanoirbeek, Greetje Vande Velde

Abstract

Micro-computed tomography (µCT) is emerging as a modality to follow-up lung disease progression in rodent models. Respiratory-gated µCT is less explored and covers the different cycles of breathing, which provides the opportunity to extract functional lung readouts *in vivo*. In this study, we extracted non-invasive µCT-derived lung function biomarkers of free-breathing anesthetised animals with different lung pathologies (pulmonary fibrosis, emphysema, infection, and epithelial barrier damage), thereby gaining novel insights in lung (patho)physiology of rodent models. For each lung pathology (bleomycin- and silica-induced pulmonary fibrosis, elastase-induced emphysema, *Cryptococcus* lung infection, naphthalene-induced lung epithelial barrier damage), mice were scanned weekly throughout disease development and progression with respiratory-gated high-resolution µCT (4D). 4D µCT provides information on the breathing cycle on top of 3D morphological information. The 4D time-based retrospectively gated µCT data allowed extraction of functional readouts including; end-inspiratory (EIV) and end-expiratory (EEV) lung volume, tidal volume (TV) and centre of tidal volume (cTV). We defined two biomarkers from our scans: (1) the TV is the volume of air, which the animal inhales with every breath; (2) the cTV is the Functional Residual Capacity plus half of the tidal volume (FRC+TV/2) which corresponds to the volume around which the animals spontaneously breathe. We found a decreased imaging-derived cTV in the bleomycin-induced lung fibrosis model, while it was not altered in the silica-induced lung fibrosis model. In the elastase-induced emphysema, both the TV and the cTV were increased, while in the *Cryptococcus* model only the cTV was increased. In the mouse model for epithelial barrier damage, no differences in TV, nor cTV were found. From the µCT scans, we are able to extract lung function readouts of free breathing anesthetized animals. This non-invasive approach allows longitudinal functional follow-up of parameters that cannot be measured by any other device throughout an entire lung disease process. The novel cTV parameter resulted in original observations that can contribute to preclinical lung research, emphasizing the importance of µCT for longitudinal lung studies.

Introduction

Animal models are an important tool for pulmonary research. A variety of models exists that mimic asthma, emphysema and fibrosis among others, preferably mimicking the clinical features of human pathology [57,196,197]. A frequently used and essential clinical readout in patients and experimental animal models is lung function, which provides important information concerning the physiological characteristics of lung disease [81,198]. To test therapy in experimental models, it is essential to understand the resemblance of the model with the clinical physiology.

Currently, there are several non-invasive and invasive techniques available to perform lung function measurements in small animals, each with its own benefits as well as their limitations [81]. Unrestrained whole-body plethysmography (WBP) is a non-invasive method to monitor spontaneous airway mechanics giving us information such as frequency of breathing, tidal volume and peak flows [79,80]. However, its specificity to determine a lung disease remains unclear. Vanoirbeek *et al*. showed that it was difficult with WBP to differentiate end-stage lung diseases in different mouse models [81]. Therefore, WBP is often substituted by invasive lung function measurements [199]. Two invasive systems are commercially available: Buxco (DSI) and flexiVent (SCIREQ – EMKA Technologies). Both systems require anesthetized and tracheotomised animals and are mostly, but not always, terminal [79,82]. These systems determine physiological readouts such as pressure-volume and flow-volume curves resulting in clinically relevant readouts e.g. vital capacity, resistance and compliance [83,84]. Due to their invasiveness, these systems provide more extensive readouts in animals. The most important restriction of both methods is likewise their invasiveness, which makes them difficult to apply in a longitudinal setup in order to monitor lung function over an entire disease process. Follow-up of individual animals throughout the whole process is not possible and therefore endpoint measures of different animals are often used.

To overcome this problem, micro-computed tomography (µCT) could be used as it has the possibility to extract *in vivo* functional lung readouts in individual animals throughout the entire disease process. µCT is an emerging modality to non-invasively follow lung disease progression in rodent models [75,91,99-102]. Due to its high air-tissue contrast, it provides visual and quantitative anatomical 3D information of the lungs, as shown in different animal models of fibrosis, lung metastasis, lung infection, emphysema and asthma [75,91,93,99-102,200,201]. In preclinical lung imaging, gating strategies are used to avoid image blurring due to breathing motion. With a prospective gating approach, images are acquired only during a steady phase of the breathing cycle [115,116], either by restricting acquisition to the relatively stable expiration phase, or during a breath hold manoeuvre. For the latter approach, animals need to be intubated and connected to a ventilator similar as to lung function measurements, which is an invasive

procedure not without risk in small animals [117-119]. A second gating option is through retrospective gating, which deals with filtering out breathing motion after acquisition. Two alternatives for extracting information on the breathing pattern needed for retrospective gating are available, time-based and image-based retrospective gating. For image-based gating, the intensity changes within a defined region on the image due to breathing are extracted as breathing signal from the images and used as a proxy for the breathing cycle. Each projection image is then assigned to a certain breathing phase based on the breathing signal extracted by image analysis. For time-based gating, physiological time-points, i.e. each inhalation and exhalation of the breathing cycle are recorded either by a hydraulic pressure pad taped against the thorax, or ideally by video movement detection (as this does not interfere with lung anatomy). With this breathing signal measured either externally or extracted from the projection images, images are sorted according to a certain breathing phase they were acquired in [120,202]. Contrary to prospective gating, respiratory-gated µCT data covers the entire breathing cycle. In this study, we demonstrate that this approach allows extraction of both morphological as well as functional biomarkers including lung volumes at inspiration, expiration and tidal volume. This results in functional biomarkers reflecting the different phases of the breathing cycle. Moreover, this approach can be performed on free-breathing animals under light anaesthesia, reflecting more the physiological state of the animal.

In this study, we extracted novel lung function readouts from time-based retrospectively gated longitudinal µCT data of free-breathing anesthetized animals with bleomycin- and silica-induced pulmonary fibrosis, elastase-induced emphysema, fungal infection and naphthalene-induced epithelial barrier damage and compared them to readouts of lung function available from standard endpoint lung function measurements (flexiVent).

Materials and methods

Animal models

The Animal Ethics Committee of the KU Leuven approved all experimental procedures (P057/2018, P236/2014, p103/2012 and p116/2011). All animals were housed in individually ventilated cages (IVC) in a conventional animal facility with access to water and food *ad libitum*, according to European, national and institutional guidelines for animal welfare and experimental conduct. Part of the data in this study is extracted from previously published mouse data, for which we previously investigated µCT-derived morphological, inflammatory (BAL and histology) and end-stage invasive lung function [75,189,203]. µCT data was reanalysed with the here optimized algorithm and additional biomarkers extracted. The total number of animals used was 60.

Bleomycin induced pulmonary fibrosis Eight-week old male C57Bl/6 mice (Janvier, Le Genest, France), weighing 22-25 grams, were anaesthetized with intra-peritoneal injection of ketamine and xylazine and fibrosis was induced by intratracheal instillation via a tracheotomy of 0.05 U bleomycin (Sanofi-Aventis, Diegem, Belgium) in 50 µL of sterile PBS or PBS as a control [75].

Silica-induced pulmonary fibrosis Eight-week old male C57Bl/6JRj mice (Janvier, Le Genest, France), weighing 22-25 grams, were anaesthetised by inhalation of 4% isoflurane (Piramal Healthycare, Morpeth, Northumberlang, United Kingdom) in 100% oxygen and endotracheally instilled with crystalline silica particles (5 mg/animal dissolved in saline), or saline (NaCl 0.9%) [189].

Elastase-induced emphysema Eight-week old male C57Bl/6 mice (Janvier, Le Genest, France), weighing 22-25 grams, were anaesthetized with intra-peritoneal injection of ketamine and xylazine and fibrosis was induced by intratracheal instillation of 0.5 U of porcine pancreatic elastase (PPE) in 50 µL of sterile PBS. The control group was instilled with PBS [75].

Cryptococcus lung infection Eight to ten-week old female Balb/cAnNCrl mice (Charles River Laboratories, bred at the KU Leuven animal facility, Leuven, Belgium) were infected by inhalation of a GFP-expressing *C. gattii* R265 [204] cell suspension of 500 or 50.000 live cells in PBS (20 µl, 10 µl per nostril) or with PBS alone (sham control) under 2% isoflurane gas anaesthesia.

Naphthalene-induced lung epithelial barrier damage Seven-week old male C57Bl/6J mice (Envigo, Horst, The Netherlands) were intra-peritoneally injected with naphthalene (NA) in a dose of 200 mg/kg body weight (BW) dissolved in mineral oil (MO, 10 mL/kg BW). The control group received an injection of MO only [203].

Experimental design

Animals were scanned at baseline and weekly post disease induction, unless mentioned otherwise (Figure 1).
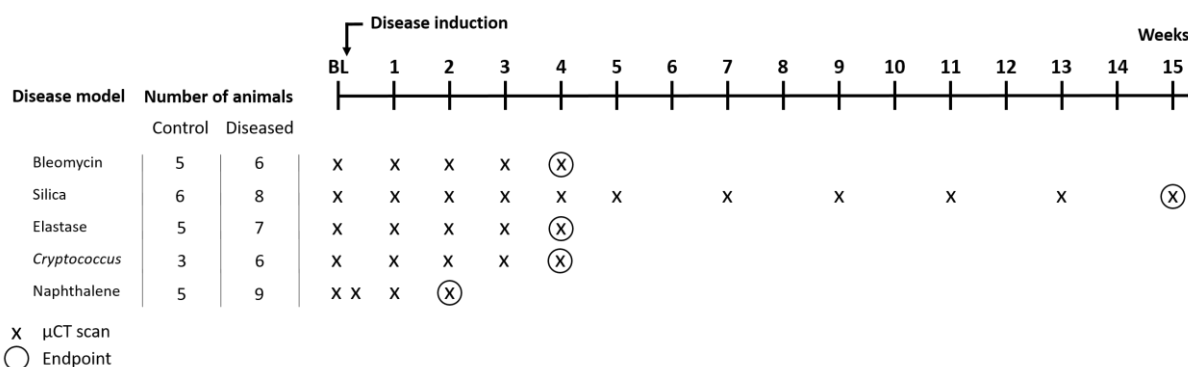

Figure 1: experimental design.

This scheme summarizes the scanning protocol for all animal models, including the number of control animals and animals with induced lung disease. X indicates a 4D μCT scan. At endpoint, we evaluated the following readouts: μCT, lung function by flexiVent and *ex vivo* measurements.

Micro-computed tomography

Mice were anesthetized by inhalation of 1.5-2% isoflurane in 100% oxygen and scanned with a dedicated *in vivo* μCT scanner (Skyscan 1278 or Skyscan 1076, Bruker microCT, Kontich, Belgium) with time-based retrospective respiratory-gated 4D acquisition [75,195]. Mice were scanned in supine position and during image acquisition thoracic movement was recorded with a visual camera, detecting the up- and downward movement of the thorax [75,203]. Images were acquired with retrospective time-based gating in list mode with nine projections per view. The following scan parameters were used:

(1) SkyScan 1278: 50 kVp X-ray source voltage and 918 μA current combined with a composite X-ray filter of 1 mm aluminium, 55 ms exposure time per projection, acquiring projections with 0.9° increments over a total angle of 220° and field of view covering the whole body producing reconstructed 3D data sets covering the thorax, with 50 μm isotropic reconstructed voxel size.

(2) SkyScan 1076: 50 kVp X-ray source voltage and 180 μA current combined with a composite X-ray filter of 0.5 mm aluminium, 120 ms exposure time per projection, acquiring projections with 0.7° increments over a total angle of 220° and field of view covering the thorax producing reconstructed 3D data sets with 35 μm isotropic reconstructed voxel size.

Image analysis

Software provided by the manufacturer (TSort, NRecon, DataViewer, and CTan) was used to retrospectively gate, reconstruct, visualize, and process μCT data. The duration of a complete respiratory cycle was divided into four phases of identical length, corresponding with the four different phases of the respiratory cycle (4D), from initiation of inspiration to end-expiration. All images were

sorted according to the phase of the breathing cycle in which they were logged. This resulted in four different reconstructed datasets corresponding to four different breathing cycle phases. An in-house developed automated algorithm was used for the segmentation of aerated lung volumes [75]. In short, this algorithm was based on defining a region of interest that equals the image of the animal by a threshold that separates the animal from the surrounding air and 'despeckle' manoeuvre. Next, a second threshold was set (optimized per animal model and depending on the type of settings used, Table 1) to separate the lung pathology from the connected healthy lung tissue, thereby determining the aerated lung volume within the animal. From the retrospectively gated 4D µCT datasets, we considered reconstructed datasets corresponding to four different phases of the breathing cycle from which we extracted aerated lung volumes corresponding to the different phases of breathing. End inspiratory aerated lung volume (EIV) was defined as the volume at the end of inspiration (Figure 2). End expiratory aerated lung volume (EEV) was defined as the volume at the end of expiration (Figure 2). Based on these volumes the following readouts were determined:

$$Tidal\ volume = EIV - EEV \tag{1}$$

$$cTV = EEV + \frac{Tidal\ volume}{2} = \frac{EIV + EEV}{2} \tag{2}$$

Table 1: type of scanner and threshold used to separate pathology from the connected healthy lung tissue for each animal model.

Animal model	Scanner	Threshold (HU)
Bleomycin	Skyscan1076	-385
Silica	Skyscan1278	-223
Elastase	Skyscan1076	-385
Cryptococcus	Skyscan1076	-385
Naphthalene	Skyscan1278	-223

Tidal volume (TV) and centre of the tidal volume (cTV) were calculated for all animals at every scan time point. At endpoint, the two different functional readouts were visualized by a sinusoidal wave using the statistical program R (RStudio Team (2016). RStudio: Integrated Development for R. RStudio, Inc., Boston, MA URL http://www.rstudio.com). All parameters of the sinusoidal function were calculated based on the aerated lung volumes determined by the algorithm at end-inspiration and end-expiration:

$$y = a * \sin(b * t + c) + d \tag{3}$$

With: a = amplitude = tidal volume/2;   c = phase shift = 0;

       b = period, arbitrary;   d = vertical shift = EEV + (TV/2) = cTV.

We included models of obstructive and restrictive human pathology in this study, which are previously published studies, with confirmed progressive lung pathology by *in vivo* µCT data and lung function measurements for each model [75,89,189,203]. Here, we reanalysed the retrospectively time-based gated 4D µCT data to extract imaging-derived lung functional readouts. From the four reconstructed datasets, two correspond with inspiration and expiration. We extracted the end-expiratory (EEV) and end-inspiratory (EIV) aerated lung volume using an automated algorithm optimized per disease model. These volumes allowed us to calculate the tidal volume (TV) and the centre of tidal volume (cTV) (Figure 2).
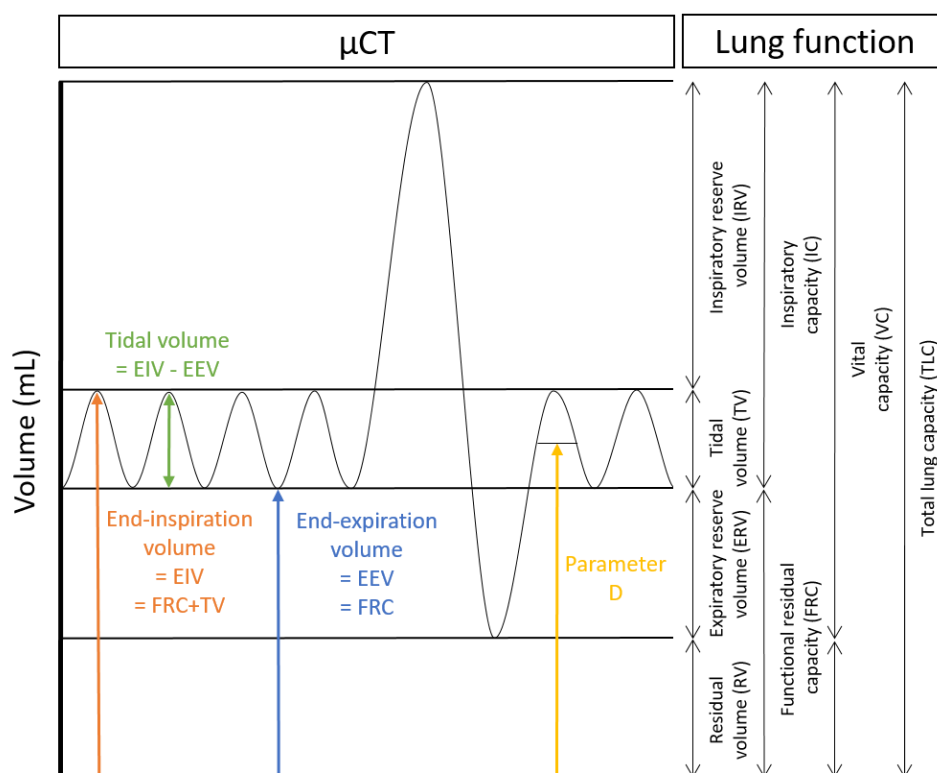
Figure 2: overview of lung function and µCT-derived readouts.
Several breathing cycles are depicted on the figure. On the right side frequently used lung function readouts are given, acquired under artificial ventilation in animals. In colour, µCT-derived functional biomarkers (of free-breathing animals) are displayed: tidal volume (TV), end-inspiration volume (EIV), end-expiration volume (EEV) and Centre of tidal volume (cTV). Note, due to the manner of derivation, µCT-derived and lung function readouts are therefore not fully equal.

Mathematically, the TV corresponds with the amplitude of the sinusoidal wave (Eq (1) and (3); the cTV corresponds with the oscillation level of the sinusoidal wave (Eq (2) and (3) in materials and methods, 'Image analysis'). Functionally, the TV is the volume of air, which the animal takes in with every breath [205]. The cTV is the functional residual capacity plus half of the tidal volume (FRC+TV/2) and this corresponds with the volume around which the animals spontaneously breathe. It reflects both the tidal volume as well as end-expiratory volume.

Statistical analysis

The data were analysed using GraphPad Prism (version 8.02. Graphpad Software Inc., San Diego, USA). The data are presented as mean and individual values. Normal distribution was assessed by the Kolmogorov-Smirnov test. Data at endpoint were analysed by an unpaired t-test if normally distributed. Data of longitudinal µCT-derived biomarkers (without missing values and with a balanced design) were analysed using repeated measures ANOVA. Data of longitudinal µCT-derived biomarkers (with missing values and an unbalanced design) were analysed using a mixed-effects model with Geisser-Greenhouse correction. For multiple comparison, Sidak's *post hoc* test was used. For all tests, statistical significance was assumed when * p-value < 0.05; ** p-value < 0.01 and *** p-value < 0.001. Number of animals for every disease model, per group are shown in figure 1.

Results

Centre of tidal volume (cTV) and tidal volume (TV), novel imaging-derived functional biomarkers

All mice in each of the different lung disease models (bleomycin- and silica-induced pulmonary fibrosis, elastase-induced emphysema, *Cryptococcus* lung infection naphthalene-induced lung epithelial barrier damage) were scanned at baseline and received weekly a follow-up scan using respiratory-gated 4D μCT to longitudinally evaluate lung disease progression in a free-breathing setting (Figure 1, experimental design).

We found substantial changes in TV (green arrows) and cTV (yellow arrows) in several lung disease models investigated (grey line = diseased mice vs black line = control mice) at endpoint of the model (Figure 3). Figure 3 shows a visual representation of the shift in TV and cTV. In Figure 4, the quantification of this data can be found. The shift of the cTV is most obvious in the bleomycin fibrosis model and the elastase-emphysema model compared to its own 'healthy' control group. In the silica-fibrosis model, the cryptococcal infection model and the epithelial barrier model, minor differences in cTV and TV are found.

μCT derived functional data quantitatively reflects disease status of the animal

We calculated the TV and cTV to look in detail to lung function changes derived from our μCT scans at the end stage of disease i.e. at the last experimental time point; the most severe disease phase. Compared to the control group, the bleomycin-induced lung fibrosis model showed a significantly decreased cTV (mean -0.2158; 95% CI: -0.3851 to -0.04656) (Figure 4B), confirmed by a downward shifted pressure-volume loop and a decreased compliance derived from flexiVent previously published [75]. In contrast, the cTV is not decreased in the silica-induced lung fibrosis model, compared to its own control (mean 0.06414; 95% CI: -0.02446 to 0.1524) (Figure 4B). This was confirmed by previously published flexiVent data by an unaltered inspiratory capacity at endpoint [189]. In the elastase-induced emphysema model, we found a significantly TV (mean 0.06601; 95% CI: 0.003643 to 0.1284) and cTV (mean 0.3665; 95% CI: 0.2576 to 0.4754) (Figure 4A and 4B), which corresponded with increased compliance measured by flexiVent [75]. The cTV was also significantly increased for the *Cryptococcus* infection model, compared to non-infected mice (mean 0.06559; 95% CI: 0.02150 to 0.1097) (Figure 4B). Moreover, the cTV of control and infected mice were lower compared to the other mouse models due to a different strain used (balb/c). In the mouse model of naphthalene-induced epithelial lung damage, we did not find any differences in imaging-derived TV (mean 0.03372; 95% CI: -0.002777 to 0.07022) nor in cTV (mean 0.07149; 95% CI: -0.03930 to 0.1823) compared to its own control (Figure 4B) whereas on flexiVent an increased forced vital capacity was found [203].
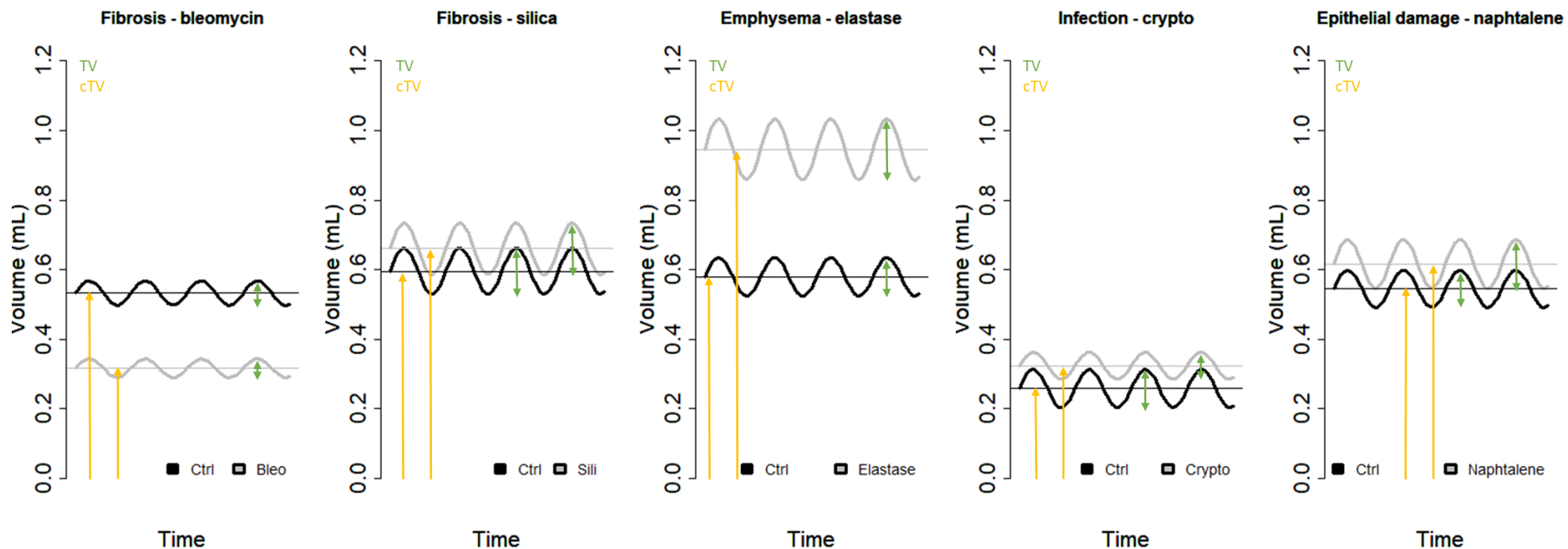
Figure 3: Tidal Volume and Centre of Tidal Volume for animal models of lung diseases.

For every animal model (bleomycin- and silica-induced pulmonary fibrosis, elastase-induced emphysema, Cryptococcus lung infection naphthalene-induced lung epithelial barrier damage as indicated above the figure), a sinusoidal wave is plotted to visualize the Tidal Volume (TV) and Centre of Tidal Volume (cTV) induced by the different modeled lung diseases versus healthy controls, both derived from non-invasively acquired µCT-derived data. The amplitude of this wave corresponds with the TV (indicated by the green arrows) and the oscillation level corresponds with cTV (indicated by a horizontal line and yellow arrows). cTV reflects both the functional residual capacity and tidal volume. Data presented is average derived from µCT scans right before experimental endpoint.

Figure 4: *in vivo* µCT-derived Tidal Volume and Centre of Tidal Volume upon lung pathology.
(A) Tidal Volume (TV) for control and diseased animals at the last experimental time point. (B) Centre of Tidal Volume (cTV) for control and diseased animals at endpoint. Data are presented as mean and individual values. For comparing control and diseased group, Mann-Whitney test was used. * p-value < 0.05; ** p-value < 0.01; *** p-value < 0.001.
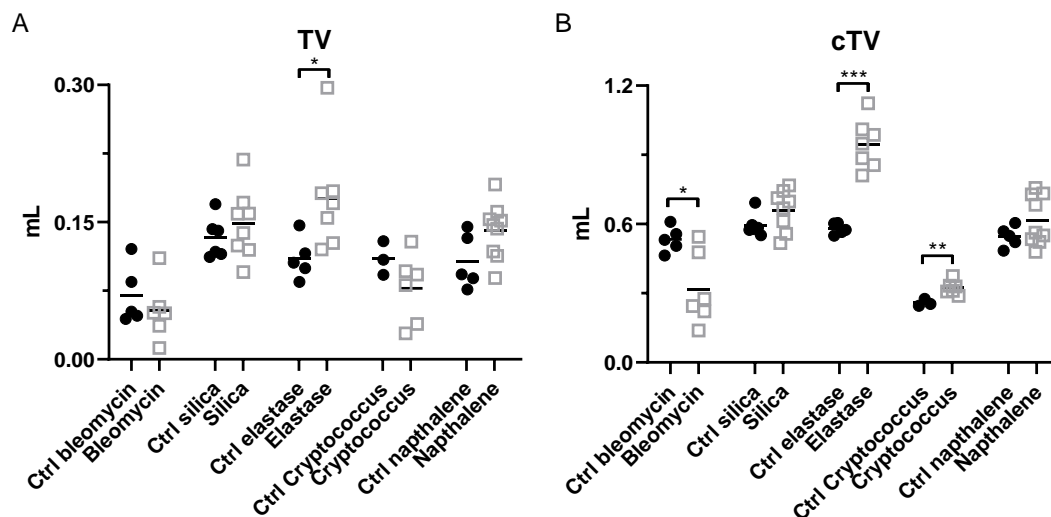
4D µCT enables longitudinal non-invasive functional evaluation of lung disease models

We next verified whether µCT allowed us to notice lung function changes early in the disease process. Therefore, we extracted longitudinal and non-invasive functional readouts over the entire course of every disease model. Every animal model was scanned at baseline and after disease induction with a time resolution to cover the course of disease development over relevant time frame (Figure 1).

In the bleomycin-induced fibrosis model, we found no differences in TV over the course of 4 weeks although inflammation and fibrosis are progressing [75] (Figure 5A). The cTV was already significantly lower 1 week after bleomycin administration, which remained stable afterwards, compared to the healthy controls (Figure 5B). The longitudinal follow-up of TV in the silica-induced fibrosis model, showed no differences (Figure 5C), while the cTV was significantly higher 2 weeks after silica administration and remained increased until week 9 (Figure 5D). In the elastase emphysema model, the TV remained the same as in the control group (Figure 5E), except for the last scanning point, where we found a significantly elevated TV in the elastase group. For the cTV, one week after elastase administration, it was significantly higher compared to the healthy controls and remained significantly increased for the following 4 weeks (Figure 5F). In the *cryptococcus* infection model (Figure 5G and H), no difference was found in both the TV and cTV readouts. This was also the case for the naphthalene-induced epithelial barrier model, which did not show any differences in TV and cTV between the treated and non-treated groups, although pathology was present in this model (Figure 5J and K).

113
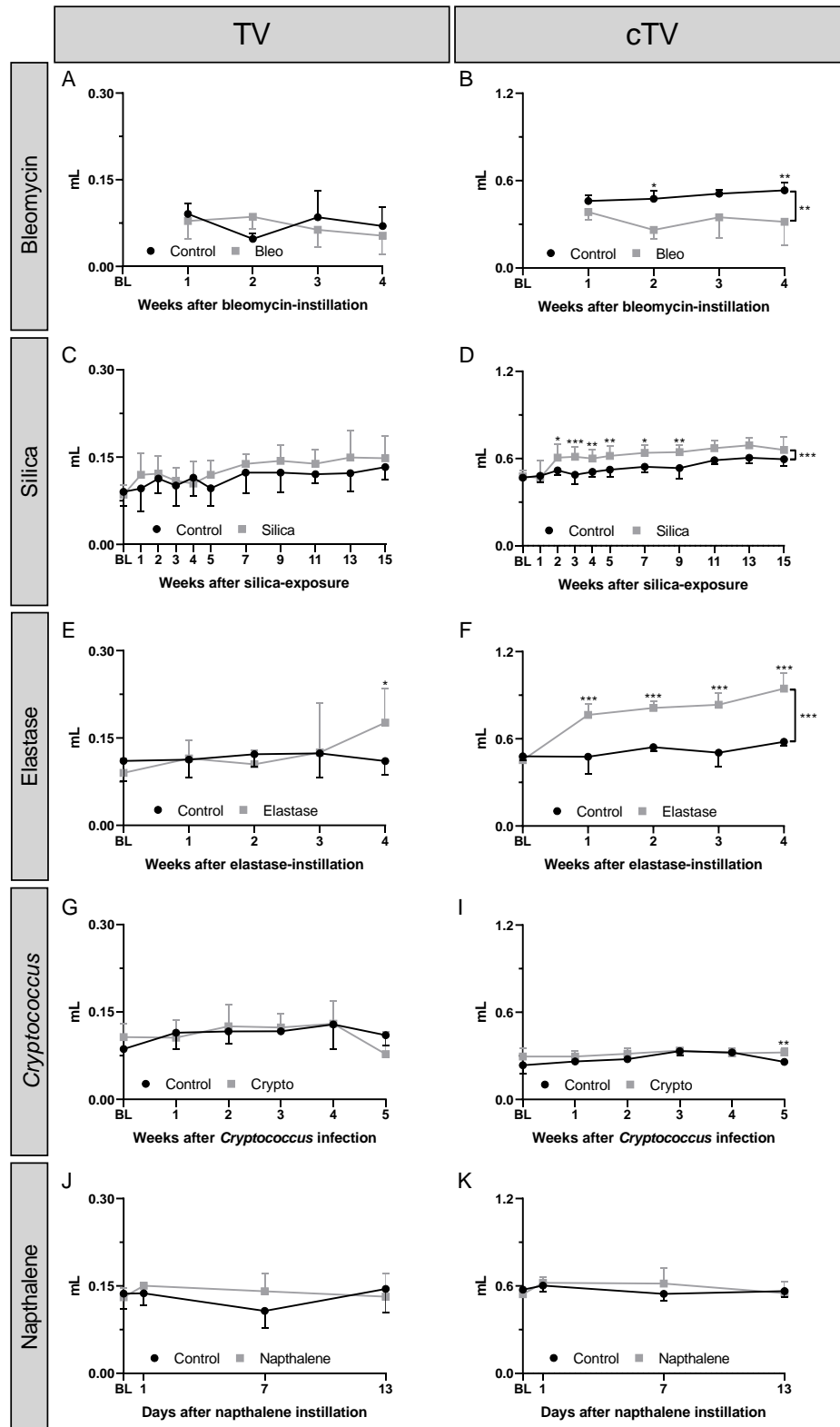
Figure 5: *in vivo* **µCT-derived lung function readouts can longitudinally evaluate lung function over the disease course.**
(A, C, E, G, J) Tidal Volume (TV) for control and diseased animals over the entire disease course. (B, D, F, I, K) Centre of Tidal Volume (cTV) for control and diseased animals over the entire disease course. Data are presented as mean ± SD. For comparing control and diseased group, mixed-effects model with Geisser-Greenhouse correction was used. For multiple comparison, Sidak's *post hoc* test was used. * p-value < 0.05; ** p-value < 0.01; *** p-value < 0.001.

Discussion

Here, we show for the very first time the feasibility to extract biomarkers of lung functional measurements from longitudinal µCT in preclinical animal models (bleomycin- and silica-induced pulmonary fibrosis, elastase-induced emphysema, *Cryptococcus* lung infection and naphthalene-induced lung epithelial barrier damage). Based on a 4D respiratory-gated µCT approach, we extracted and calculated four different readouts: the end-expiratory (EEV) and end-inspiratory aerated lung volume (EIV), the tidal volume (TV) and centre of tidal volume (cTV).

In this study, we focused on novel functional biomarkers, in addition to the morphological biomarkers that can also be derived from the µCT data as already established and previously described [75,189,203]. These morphological readouts (total lung volume, aerated and non-aerated lung volume) reflect the disease status and can identify disease progression in terms of burden of the pathology and reveal new aspects of the disease model, such as overall response of the lung anatomy in response to lung disease. To derive morphological biomarkers, a 3D expiration-weighted, end-expiratory µCT scan is sufficient. The data presented here is in-depth lung function analyses derived from µCT scans performed and published previously [75,189,203]. In these studies, we compared longitudinal µCT analysis with end-stage lung function measurements, performed with the flexiVent system. Here, we wanted to take a step further and investigate lung function biomarkers derived from non-invasive 4D µCT and evaluate how they perform in different disease models. Therefore, we describe novel biomarkers (TV and cTV) that can be derived from the µCT analysis, and which can contribute to longitudinal follow-up of disease progression. To acquire the µCT scans, animals are under light anaesthesia of isoflurane, but still freely breathing. Volatile anaesthesia are known to have an influence on the cardiopulmonary system, such as a decreased respiratory and heart rates [206]. Yet, Groeben *et al.* reported that there is no effect of isoflurane on tidal volume [207]. In our study, both the control as the diseased group were exposed to the same isoflurane conditions, making comparisons between imaging-derived lung function readouts possible and valid.

A whole body or a double chamber plethysmograph could potentially serve the same goal as they also allow longitudinal non-invasive lung function measurements. In these apparatuses, the mice are conscious and free breathing without any anaesthesia. Vanoirbeek *et al.* showed that in similar obstructive, restrictive and inflammatory models, very limited changes compared to healthy mice at a time-point of severe disease state [81]. Especially in severe emphysematous mice, the WBP did not detect differences in breathing volumes compared to healthy mice, which is in contrast to the findings of the current study [81]. Here we show that already one week after instillation of elastase, the TV is significantly increased at the final scanning moment. The WBP data from bleomycin-induced fibrosis mice showed

an increased time of inspiration, increased end-expiratory pause and an increased enhanced pause, while TV did not change compared to the healthy mice [81], which is the same as the unaltered change in TV derived from µCT scans as shown here.

The most innovative biomarker in this study is the centre of tidal volume (cTV). The cTV is the functional residual capacity plus half of the tidal volume (FRC+TV/2). This readout corresponds with the median volume around which the animal spontaneously breathes and depends on the EEV and TV. The non-invasive whole body or the double chamber plethysmograph and the invasive flexiVent do not have a parameter resembling the cTV. The Buxco forced manoeuvres apparatus is able to measure the forced residual capacity (FRC), which might result in similar data as the cTV. FRC is measured by stopping the forced ventilation at the end of expiration, with an immediate closure of a valve located proximally to the endotracheal tube. Next, spontaneous breathing maneuvers against a closed valve with consequent pressure changes at the mouth and in bodybox are used to record and calculate the FRC using Boyle's law [81,208]. Vanoirbeek *et al*. did not detect a decreased FRC in mice with bleomycin-induced fibrosis using the Buxco system, which is in contrast to our significantly decreased cTV in the bleomycin-induced lung fibrosis model and is in concordance with what to expect in a restrictive lung disease [81,209-211]. Our data show that already two weeks after instillation of bleomycin, we can detect a decrease in cTV, remaining stable over the following weeks. This proves that cTV might be a good biomarker for early restrictive lung disease. In contrast to the bleomycin-induced lung fibrosis and despite the confirmed presence of substantial lung fibrosis [166,189], the cTV is changed at the final scanning time in the silica-induced fibrosis model. On the contrary, it is even significantly increased from week 2 until week 9 compared to healthy controls, which is more indicative of an obstructive phenotype, rather than restrictive. In this silica model, we previously measured a decreased Tiffeneau index, also indicative for obstructive aspects in this model [189]. This is in contrast to what is expected for a fibrotic, restrictive lung disease model based on clinical phenotype and corresponds with an unaltered inspiratory capacity measured by flexiVent in the silica-induced fibrosis model [189]. It does not necessarily imply the model or the technique are not suitable and reliable. Without µCT, we would be missing this important information to fully understand what is happening and interpret the study results in an appropriate manner. In an elastase-induced emphysema model, Vanoirbeek *et al.* described a significantly increased FRC [81], which is confirmed by our data, showing a highly increased cTV. These findings are in line with the clinical features of airspace enlargement and an obstructive disease [81,210,211]. In the emphysema model, we could already find significant changes in cTV one week after instillation of elastase, suggesting that cTV could be a very good marker of early disease onset. In the *cryptococcus* infection model, we only found a significant, but rather limited difference in cTV at the final scan moment. This is remarkable in case of the *Cryptococcus* model, because the loss of air

spaces due to increasing infection burden and significantly decreased inspiratory capacity, as measured with the flexiVent (unpublished data), does not result in loss of FRC [89]. To interpret the *Cryptococcus* results correctly, µCT is an essential technique. From the µCT scans, we were able to see that both the non-aerated lung volume (reflecting disease burden) and the aerated lung volume (reflecting air and healthy tissue) significantly increased and thus also the total lung volume, thereby not resulting in a loss of FRC although disease burden was present [89]. We, and others, defined this as a compensation mechanism present in rodents and not in humans to overcome the increased disease burden [100,128,184,185,189]. In the naphthalene-induced epithelial damage model, we did not find any change in cTV. In this model, the epithelial damage is the most pronounced at day 7, as shown by Van Den Broucke *et al.* (2018), while at day 14; the lungs seem to be fully recovered. So here, we can conclude that the changes induced in the lungs by naphthalene are not influencing the TV, nor the cTV.

To extract these novel functional biomarkers (TV and cTV) from µCT scans, we applied a 4D respiratory-gated protocol that divides the breathing in four distinct cycles. This implies longer scanning times and increased radiation for the animals. However, we previously established this protocol as safe to use for murine scanning [195]. While 3D respiration-weighted µCT is faster and gives less radiation to the animals, it does not offer the possibility to extract functional readouts. The preferential protocol (3D vs 4D) depends on the animal model and the readouts preferably achieved.

In conclusion, we have calculated the TV and cTV from non-invasive µCT scans, resulting in novel observations and the identification of biomarkers of disease progression that should be considered for future preclinical lung research. The currently used preclinical invasive and non-invasive lung function measurements provide detailed information that we cannot (yet) extract from µCT. However, these invasive techniques have their own limitations. We showed that *in vivo* µCT is able to provide morphological as well as lung function date in a non-invasive manner, both essential for the correct interpretation of pathology in preclinical animal models. A combined approach of non-invasive lung function measurements (e.g. µCT) during the disease course and invasive, more detailed functional measurements at the end stage of disease gives complementary essential information of the animal model under investigation. This emphasizes again the usefulness of non-invasive µCT to identify early disease onset and longitudinal follow-up throughout the disease progress, thereby limiting the number of animals needed in preclinical research.

Acknowledgements

Conflict of interest

All authors declare no conflict of interest related to this work.

Chapter 7

General discussion

Section "Exploring the possibility of non-invasive longitudinal lung function biomarkers derived from µCT" partly based on

From Mouse to Man and Back: Closing the Correlation Gap between Imaging and Histopathology for Lung Diseases.

Tielemans B., Dekoster K., Verleden E., Sawall S., Leszczyński B., Laperre K., Vanstapel A., Verschakelen J., Kachelriess M., Verbeken E., Swoger J., Vande Velde G.

Summary of main findings

The general aim of this thesis was to improve information extraction from μCT that contributes to a better translatability of preclinical studies on pulmonary fibrosis, the relation with inflammation and potential treatment strategies. The following figure gives a schematic overview of the thesis (figure 1).
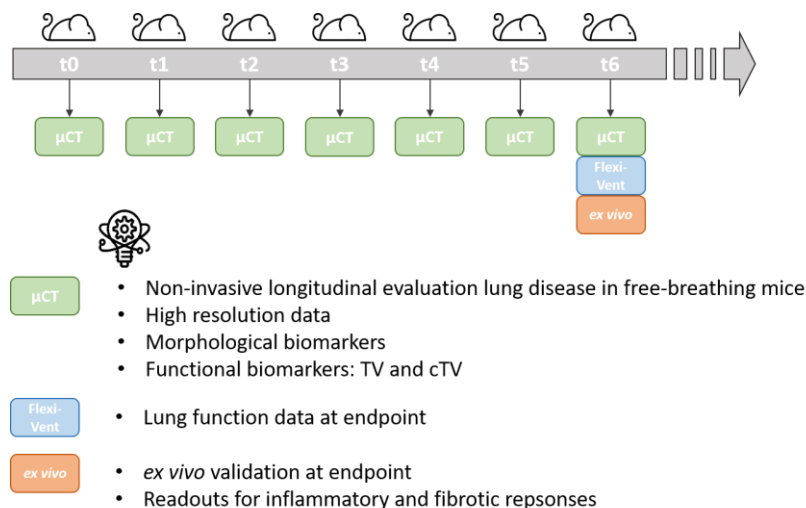
Figure 1: schematic overview of the general results of this thesis.

In the first study (**chapter 3**), we have determined the optimal dose and dose effect of *in vivo* μCT in healthy mice and lung disease models, because in these models often rapidly dividing cells are involved, that are quite radiation sensitive (cancer and immune cells in lung metastasis and pulmonary fibrosis mouse model). We found a disease-independent subclinical decrease in circulating blood platelets and lymphocytes after repeated respiratory-gated 4D μCT (dose of 540-699 mGy/scan). Consecutive scanning did not influence the general health of healthy mice nor did it alter the metastatic load in a lung metastasis mouse model. We could eliminate the disease-independent subclinical decrease in circulating blood platelets and lymphocytes by altering our imaging protocol to expiration-weighted 3D μCT thereby reducing the scanning dose to 180-233 mGy/scan. We are the first to establish an upper-safety limit (540-699 mGy/dose) on a cellular level for repetitive scanning and delivered radiosafe protocols for the lung as well as whole body.

In the second study (**chapter 4**), we developed a silica-induced lung fibrosis mouse model and longitudinally evaluated this model with μCT. We described for the first time an increase in non-aerated lung volume, at the moment of disease onset and progressive during the inflammatory and fibrotic stages of the disease. Our μCT-derived biomarkers were able to identify, quantify and longitudinally follow-up initiation and steady-state of lung inflammation, along with the onset and progression of pulmonary fibrosis for approximately 10 weeks. This model allows us to investigate both early anti-inflammatory as well as anti-fibrotic therapeutic testing.

In **chapter 5**, we evaluated the commercially available drug, Nintedanib, in an anti-inflammatory and anti-fibrosis treatment regime in a mouse model of silicosis-induced lung fibrosis, while using µCT as a longitudinal modality to assess treatment efficacy. Nintedanib only showed a subtle treatment effect, yet the silica dosing and resulting severity of the disease was less than in the model used in chapter 4 (due to a lower exposure to silica). Nevertheless, there was an agreement between *in vivo* µCT biomarkers and *ex vivo* readouts, thereby providing evidence for routine implementation of µCT for preclinical anti-fibrotic drug screening.

The last chapter of this thesis (**chapter 6**) investigated in-depth whether we could extract more advanced functional lung biomarkers from *in vivo* µCT. We describe for the very first time, two novel biomarkers from a 4D respiratory-gated scan of free breathing living animals: the tidal volume (TV) and the centre of tidal volume (cTV). These novel markers could clearly identify a different breathing pattern in obstructive and restrictive lung disease models. These data will contribute even more to longitudinal follow-up of lung function decline and possibly towards the future also improvement after therapy.

µCT and its relevance in preclinical lung research

Others and we have now repeatedly and convincingly proven the usefulness of µCT in preclinical (lung) research for e.g. pulmonary fibrosis, lung metastasis, lung infection and inflammation [75,91-94,99,100]. µCT has a high air-tissue contrast ideal for lung imaging, it is relatively cheap, the scanning times are short and it provides morphological and structural information of the lung and disease under investigation. Repetitive scanning allows follow-up of individual animals throughout the entire disease process, which has the important advantage of reducing the number of animals needed (3R legislation) and provides us with information of the disease process that is irreplaceable by endpoint measurements [90].

Consecutive scanning to follow-up the disease in a longitudinal manner results in cumulative radiation exposure, which potentially has negative effects on the animal and possibly influences the disease process under investigation. In the field of radiotherapy, with much higher administered doses (4 to 20 Gy) compared to the doses used in our µCT approach (often below 1 Gy), the effects of repeated radiation are thoroughly investigated, whereas studies on exposure effects in the context of µCT are lacking. Previous studies investigating the effect of consecutive µCT scanning exclusively on healthy animals and mostly included only macroscopic influences of x-rays (e.g. histology, fibrotic load and µCT-derived biomarkers of lung disease) [127,150]. We have taken this a step further, with the inclusion of murine disease models, with rapidly dividing lung cells, which are often very prone to radiation stress. We analysed both healthy and diseased DBA/2 and C57Bl/6 mice, commonly utilized

immunocompetent strains in preclinical pulmonary research. As we only used immunocompetent mice, we cannot expand our results to immunodeficient mice that are more sensitive to radiation damage. We think it is essential to establish safe μCT scanning protocols for animal models with an essential role of lung inflammation and remodelling. In the mouse model of lung metastasis, we could not find an adverse macroscopic health effect of consecutive 4D μCT scanning. Yet, when we diploid our 4D scanning protocol in the models of lung metastasis, fibrosis and even in healthy mice, we were able to detect in the circulating blood cells (a compartment of the body that is very sensitive to radiotoxicity [158,159]), a lower blood platelet and lymphocyte count. These results are indicative of a disease-independent effect of consecutive radiation exposure without an influence on the general health of these animals. It is important to note that we could eliminate this effect (if needed for the experiment), by using a 3D protocol which reduced the scanning time and hence the delivered dose. Nevertheless, for any other experimental setup with more frequent scan repetitions such as in daily scanning or longer scanning times, one should monitor the effects of cumulative radiation at a cellular level, e.g. in whole blood, with the inclusion of appropriate control groups, which are for example not scanned or undergo only limited scanning moments.

While we have shown that consecutive scanning did not influence the disease under investigation, nor did it have an effect on the general health of the animals, we did not show a possible effect on a genetic level. It would be interesting to assess the number of γ-H2AX foci, which is representative for double stranded DNA breaks and can be used as a biomarker for radiation damage and as an evaluation of the intrinsic repair capacity [212]. We also did not address the effects of low-dose radiation on the hematopoietic blood cell population in the bone marrow. In addition, we did not assess changes in specific lymphocyte subtypes or perform functional lymphocyte assays. Due to the low dose delivered and the time in between scans, we expect these effects to be rather small. However, we cannot formerly exclude them and even though they are potentially small, they can be of importance for certain studies.

Recently, we further optimised a protocol that reduces the dose even further to one third of the dose delivered with the 3D protocol (one third of 233 mGy equals 78 mGy). This reduced-dose protocol has the following settings: 50 kVp X-ray source voltage and 346 μA current combined with a composite X-ray filter of 1 mm aluminium, 150 ms exposure time per projection, acquiring projections with 0.9° increments over a total angle of 220°, 10 cm field of view covering the whole body producing reconstructed 3D data sets with 50 μm isotropic reconstructed voxel size. This is currently the protocol used for routine lung research when no information of the breathing cycle is required. Further efforts to reduce the dose to a minimum focussed mostly on system hardware and image reconstruction algorithms [213-216].

The imaging protocols used in this thesis are completely translatable to other lung disease models. Others and we have repeatedly and convincingly proven the usefulness of μCT in preclinical (lung) research for e.g. pulmonary fibrosis, lung metastasis, lung infection and inflammation [75,91-94,99,100]. Moreover, preliminary data also suggest a role for μCT evaluation in a cigarette smoke-induced emphysema mouse model (unpublished) and a murine neutrophilic asthma model where the aerated and non-aerated lung volume, respectively, increased as a marker of disease burden [217].

Silicosis mouse model, a stable pulmonary fibrosis model?

Identifying an ideal animal model to investigate a certain disease is almost impossible. For pulmonary fibrosis research, different animal models have been developed, but all of them were limited to one or a few feature of the disease as seen in the clinical situation [57]. Therefore, for the selection of an appropriate model, it is important to consider both the advantages as well as the limitations. IPF, for example, is a complex, heterogeneous and irreversible disease. It would therefore be desirable if the animal model also presented with a stable irreversible fibrotic phase.

Lately, a renewed attention for silica-induced fibrosis, silicosis, came. This form of fibrosis affects millions of people in India, China, Australia, Turkey and the USA, emphasizing the importance of proper characterization of silica-induced pulmonary fibrosis rodent models [168-170]. In chapter 4, we applied and characterized a silicosis mouse model using *in vivo* μCT and *ex vivo* endpoint measurements. To the best of our knowledge, this was the first study that implemented μCT for the longitudinal evaluation of a silicosis mouse model, using a single exposure to silica. Using μCT, we established novel elements of this model. We found an increase in presence of lung consolidations, as confirmed by the increased concentration of OH-proline, and an increased functional lung volume derived from μCT 2 weeks after silica instillation, which was not confirmed by invasive lung function measurements, as shown by an unaltered inspiratory capacity, FVC, FEV or elasticity. This is a remarkable contra-intuitive finding since often a reduced functional lung volume is interpreted as a sign of restrictive disease. Therefore, including exclusively lung function measurements as an endpoint, one would underestimate the presence of restrictive lung disease in this silicosis model. Implementing longitudinal μCT adds substantially to identify inflammatory and fibrotic processes in preclinical studies.

Not a single animal model fully recapitulates all aspects of IPF, nor other diseases related to pulmonary fibrosis. The fibrosis pathology in murine models is not fully aligned with the human fibrosis disease, probably due to the anatomical and immune-pathophysiological differences between mouse and human lungs [6,218]. Alternative animal models (e.g. rat, pig, ferret, sheep, horse) could possibly be better for anatomical/pathological reasons, but due to additional costs and limitation in possibilities for molecular research, are not considered better. Therefore, the American Thoracic Society recommends

using murine models as the first line animal model to study pulmonary fibrosis and its therapy options [6]. Nevertheless, it is important to evaluate animal models in an appropriate manner with the right technology to extract meaningful data from experiments and learn as much as possible from the model within its limitations when evaluating a tested therapeutic.

We used a silica-induced pulmonary fibrosis mouse model that is especially relevant for the disease silicosis and pulmonary fibrosis in general. This model has several advantages, such as clinically relevant fibrotic nodules, its low cost, it is easy-to-perform, has low inter-animal variability, zero mortality rate and a steady state of inflammatory and fibrotic processes ideal for therapy testing. This non-resolving fibrosis phase mimics better the human situation compared to the acute bleomycin model. The silicosis model outperforms the bleomycin model that comes at the cost of high variability and mortality and which is believed to resolve over time in a subset of mice [55,219]. The chronic bleomycin model with repeated induction could potentially serve the same goal of progressing fibrosis. In the repetitive model, bleomycin is administered repeatedly via endotracheal intubation or systemic intraperitoneal and intravenous injections [57]. With the administration of 0.04 U bleomycin every two weeks endotracheally (eight doses in total), fibrosis remains present up until 20-30 weeks after the final dose administration. When administering systemically 20 U/kg twice weekly for 8 weeks, fibrosis appears after 4 weeks and remains present up until 12 weeks. It is suggested that improvement and standardization of bleomycin administration via osmotic minipumps subcutaneously could result in a more consistent fibrosis model [220]. The major advantage of these chronic models is the persistent fibrosis and the therapeutic window for testing pharmacological compounds [58,220]. Yet, we achieved this therapeutic window with a single oropharyngeal instillation of 5 mg silica particles, which is less invasive and less expensive. In our opinion, multiple fibrosis models should be tested in pre-clinical studies, so the possible therapeutic effect is broadly investigated and not only evaluated in the most used acute bleomycin model.

Towards optimizing animal models to resemble the physiological situation as closely as possible, one could consider the relevance of route of exposure. In the human situation, silica particles are inhaled as dusts or fine dust. Thus, to mimic the clinical situation, it would be ideal to deliver the particles with the natural inhalation route. However, this comes with technical difficulties: specialized equipment is needed, it consumes a large number of particles, it is difficult to exactly monitor the delivered dose and a single exposure moment is probably not enough, resulting in repeated exposure protocols to induce pulmonary fibrosis [57,61,221]. Therefore, particles are often dissolved in a liquid carrier and intratracheal instilled after (light) anaesthesia [63]. This technique has the disadvantage of uneven distribution in left and right lung lobes, requires expertise and is not without risk for the animal [222]. In

our model, we used an oropharyngeal instillation technique to deliver the particles in a liquid solution to the lungs. Silica particles were dissolved in saline and administered by simultaneously holding the tongue and covering the nose as previously described by others [63,167]. Lakatos *et al.* compared directly intratracheal with oropharyngeal instillation and concluded that after oropharyngeal instillation, there was a more uniform distribution and better reproducibility compared to the intratracheal instillation [63]. Another option one could use is intranasal instillation. By instilling 50 µL intranasal, only ± 50% reaches the lower respiratory tract while the rest appeared in the gastrointestinal tract [223]. With oropharyngeal instillation, we expect this to be higher although a part also reaches the gastrointestinal tract instead of the lungs.

In chapter 4 and 5, two different concentrations of crystalline silica particles were used to initiate pulmonary fibrosis development. Reducing the concentration by half resulted in substantial less fibrotic lesions in the lungs (based on histology and collagen content). Clearly, a concentration-response is noticeable in our experiments; 2.5 mg in 40 µL silica particles is not sufficient to induce an unambiguously detectable amount of fibrosis, while inflammation is present. Mayeux *et al*. showed that both silica concentration and instillation volume are important to induce pulmonary fibrosis [224]. They evaluated several concentrations and instillation volumes and concluded that 5 mg dissolved in 50 µL were needed to induce significant alveolitis. A sufficient volume was needed to enhance a good distribution of particles over the several lobes to the periphery. We used 5 mg dissolved in 40 µL, showing a uniform distribution over the lobes with centrilobularly located silica particles. Towards future research, it would be interesting to optimize the model further and investigate whether a higher volume in combination with the lower concentration would lead to a more peripheral distribution of the particles. The optimisation of animal models will remain a continuous effort towards improving translatability of animal study results to the human situation.

Routine implementation of µCT in a preclinical drug-screening platform

Numerous anti-fibrotic compounds successfully evaluated in animal models failed when implemented in clinical trials [6,49]. In this regard, the American Thoracic Society published a manuscript in 2017, in which they discussed three major themes regarding the difficulties in animal research of pulmonary fibrosis and how to improve the translation from bench to bedside: choice of animal, practical considerations of fibrosis modelling and fibrotic endpoint for evaluation [6]. In short, the recommendations at the time were to use an intratracheal bleomycin mouse model with OH-proline assay and histology as endpoint measures. Yet, with our research contribution, we believe that these two endpoints provide a rather limited knowledge of what happens during the disease process and after therapeutic administration.

To evaluate the potential of μCT to detect the early onset of disease and to evaluate preclinical drug testing, we administered Nintedanib in two very distinct treatment regimens: 1/ in an anti-inflammatory and 2/ in an anti-fibrosis treatment regimen. We found that Nintedanib administration in both regimens resulted in a decreased presence of lung consolidations, while the functional and total lung volume increased after Nintedanib administration in the anti-fibrosis treatment regimen, which possibly indicates a functional improvement of the animals. Although the induction of fibrosis was rather minor in this, hence also the limited effect of Nintedanib, μCT was able to detect these minor changes. Moreover, the imaging results were in agreement with *ex vivo* readouts.

While we aimed for a less severe form of fibrosis to test the efficacy of Nintedanib in chapter 5, by using only half of the concentration of silica particles used in chapter 4, this left us with more less pronounced disease than expected, which limited the therapeutic effects that could be reached. Nevertheless, to evaluate therapy for pulmonary fibrosis, we propose to implement a preclinical workflow that consists of both *in vivo* longitudinal monitoring of the disease process and therapeutic effects by μCT and at selected timepoints the standard *ex vivo* measurements (OH-proline assay, histology, inflammatory evaluations and lung function). This will provide a more holistic approach in which several assets of the disease and therapeutic effects are evaluated.

Exploring the possibility of non-invasive longitudinal lung function biomarkers derived from μCT

Next to extracting biomarkers of lung disease, 4D or time-resolved μCT offers the additional capability to extract functional biomarkers reflecting lung volumes and function in small animals freely breathing, under anaesthesia. There are several options to acquire 4D-CT. Some μCT scanners, such as ours, allow the imaging of ventilated mice, controlled by directly connecting a scanner and a lung function measurement device (flexiVent 7, Scireq, EMKA Technologies) and using a perturbation called "breath-hold". With this perturbation, a known volume of air is placed into the lungs for a short period of time (seconds), which allows the μCT to take several projections. To image the complete lungs, this perturbation needs to be repeated multiple times to result in a high-resolution lung scan. Apart from this perturbation, lung function measures may include forced oscillation lung function measurements that will result in specific tissue and large airway related parameters, such as tissue elastance and airway resistance, which is currently mostly end-stage [82,166]. This setup would allow direct comparison of lung physiology with parameters derived from imaging but is invasive and reflects artificial ventilation instead of physiological breathing. On the other hand, we can use μCT as a method to derive functional lung biomarkers from free-breathing anesthetised mice. Using respiratory-gated protocols, μCT can deliver 4D data, meaning that several reconstructions cover different phases of the breathing cycle. This 4D μCT approach allows the extraction of biomarkers reflecting vital lung function, such as

aerated lung volume and tidal volume, from free-breathing, live mice, thereby complementing data from state-of-the-art lung function measurements [8].

In the last chapter of this thesis, we explored the second option of extracting functional biomarkers from free-breathing animals. It was within our potential to derive the tidal volume and centre of tidal volume of free-breathing animals of different lung pathologies (pulmonary fibrosis, emphysema, *Cryptococcus* infection, epithelial damage) from a non-invasive 4D µCT scan. This has two major advantages: we can evaluate the functional effects in an individual animal at several timepoints during the disease and it significantly reduces the number of animals needed for an experiment, an important aspect of the 3R's principle of animal ethics [90]. Together with the morphological information obtained from µCT, the functional biomarkers are essential for the correct interpretation of lung pathology. It should be noted that if a complete, detailed image of lung function is needed, we advise to use µCT and flexiVent (at endpoint) as they provide complementary information.

Our approach for obtaining functional data is easy and the only requirement is a 4D µCT scan. Other possibilities to extract functional data, requiring equipment and expertise that is more extensive, are available but less straightforward to implement. One option is a ventilation/perfusion single photon emission computed tomography, from which ventilation/perfusion mismatching can be derived [225]. Another option is deriving parameters such as elasticity or resistance of the lung but this is currently only implemented for high-resolution clinical datasets or *ex vivo* datasets [226-228]. It would be of great added value to derive such detailed structural and functional parameters from an in vivo µCT scan which sets out a direction for the continuing research of our team. At last, recently, Khan *et al.* established an X-ray based lung function technique (XLF) to detect lung function volumes [229]. They validated this technique in healthy animals by comparing the XLF-derived volumes with CT and WBP volumes, putting forward the XLF as a promising tool for preclinical longitudinal studies that uses less X-ray dose than CT does. The validation and sensitivity of this technique in disease models is still lacking.

Future perspectives

In the present study, we provide evidence for the implementation of routine µCT in preclinical evaluation of pulmonary fibrosis mouse models and therapy studies. One of the major challenges (µCT) imaging is facing, is the ability to distinguish inflammation from remodelling, hence fibrosis formation. Inflammation and fibrosis both result in hyperdense areas on CT making it difficult to separate them. Currently, there is no technique available to solve this issue, and therefore we need to rely on endpoint measurements to provide this type of information. Different imaging options can and have been explored: MRI, PET, optical imaging. To provide evidence for an imaging marker that visualises only

inflammation or only collagen, it would be interesting to test this in a fibrotic model where no inflammatory processes are present. For MRI, probes that visualise collagen deposition and fibrinogenesis process were explored and might provide options for future research, e.g. gadolinium-based, fibrin-specific probe EP-2104R and allysine-binding gadolinium chelate Gd-oxyamine [133,134]. Optical imaging is another option to explore, where probes specifically target collagen deposition or inflammatory cells, thereby allowing proper separation of both processes [140,144].

Another important added value for the field and our research lab would be the automatic analysis of µCT scans. Currently, the regions of interest of total lung volumes are manually delineated from the scans requiring multiple days to process one longitudinal experiments' dataset. New technology like artificial intelligence and deep learning pattern recognition could lead to a workflow where scans are automatically analysed reducing the subjectivity and improving time efficiency.

Conclusion

To conclude, with this work we have taken away all hurdles and provided compelling evidence to implement µCT as a routine tool in preclinical evaluation of pulmonary fibrosis. Better quantitative and dynamic assessment of animal models and the aspects of disease they exactly recapitulate further increases knowledge on the kinetics of pathophysiological processes at play. Both preclinical studies and clinical trials will benefit from the implementation of (µ)CT, as it will lead to a better understanding of what exactly happens during the entire disease course and (experimental) treatment. Discovering new biomarkers of disease and recovery could lead to improved preclinical outcomes of therapy studies and therefore improved translatability from bench to bedside, ultimately reducing unnecessary financial expenses and improving target selection for clinical trials.

References

1   Drake, R. L., Vogl, A. W. & Mitchell, A. W. M. *Gray's Anatomy for Students*. 2nd edn, (Churchill Livingstone Elsevier, 2010).

2   National Cancer Institute SEER Training Modules. *Bronchi, Bronchial Tree, & Lungs*, <https://training.seer.cancer.gov/anatomy/respiratory/passages/bronchi.html> (2022).

3   Richeldi, L., Collard, H. R. & Jones, M. G. Idiopathic pulmonary fibrosis. *The Lancet* **389**, 1941-1952, doi:10.1016/S0140-6736(17)30866-8 (2017).

4   Rosas, I. O. *et al.* Interstitial lung disease: NHLBI Workshop on the Primary Prevention of Chronic Lung Diseases. *Annals of the American Thoracic Society* **11**, S169-S177, doi:10.1513/AnnalsATS.201312-429LD (2014).

5   Lederer, D. J. & Martinez, F. J. Idiopathic Pulmonary Fibrosis. *The New England Journal of Medicine* **378**, 1811-1823, doi:10.1056/NEJMra1705751 (2018).

6   Jenkins, R. G. *et al.* An Official American Thoracic Society Workshop Report: Use of Animal Models for the Preclinical Assessment of Potential Therapies for Pulmonary Fibrosis. *American journal of respiratory cell and molecular biology* **56**, 667-679, doi:10.1165/rcmb.2017-0096ST (2017).

7   Daniels, C. E. *et al.* Imatinib treatment for idiopathic pulmonary fibrosis: Randomized placebo-controlled trial results. *American Journal of Respiratory and Critical Care Medicine* **181**, 604-610, doi:10.1164/rccm.200906-0964OC (2010).

8   Tielemans, B. *et al.* From Mouse to Man and Back: Closing the Correlation Gap between Imaging and Histopathology for Lung Diseases. *Diagnostics (Basel)* **10**, 636, doi:10.3390/diagnostics10090636 (2020).

9   Fischer, A. & du Bois, R. Interstitial lung disease in connective tissue disorders. *Lancet* **380**, 689-698, doi:10.1016/S0140-6736(12)61079-4 (2012).

10 Kalchiem-Dekel, O., Galvin, J., Burke, A., Atamas, S. & Todd, N. Interstitial Lung Disease and Pulmonary Fibrosis: A Practical Approach for General Medicine Physicians with Focus on the Medical History. *J Clin Med* **7**, 476, doi:10.3390/jcm7120476 (2018).

11 Hutchinson, J., Fogarty, A., Hubbard, R. & McKeever, T. Global incidence and mortality of idiopathic pulmonary fibrosis: a systematic review. *Eur Respir J* **46**, 795-806, doi:10.1183/09031936.00185114 (2015).

12 Raghu, G. *et al.* An official ATS/ERS/JRS/ALAT statement: idiopathic pulmonary fibrosis: evidence-based guidelines for diagnosis and management. *Am J Respir Crit Care Med* **183**, 788-824, doi:10.1164/rccm.2009-040gl (2011).

13 Raghu, G., Weycker, D., Edelsberg, J., Bradford, W. Z. & Oster, G. Incidence and Prevalence of Idiopathic Pulmonary Fibrosis. *Am J Respir Crit Care Med* **174**, 810-816, doi:10.1164/rccm.200602-163oc (2006).

14 Raghu, G. *et al.* Idiopathic pulmonary fibrosis in US Medicare beneficiaries aged 65 years and older: incidence, prevalence, and survival, 2001–11. *The Lancet Respiratory Medicine* **2**, doi:10.1016/S2213-2600(14)70101-8 (2014).

15 Ley, B. *et al.* Pirfenidone reduces respiratory-related hospitalizations in idiopathic pulmonary fibrosis. *Am J Respir Crit Care Med* **196**, 756-761, doi:10.1164/rccm.201701-0091oc (2017).

16 Costabel, U. *et al.* Efficacy of nintedanib in idiopathic pulmonary fibrosis across prespecified subgroups in INPULSIS. *Am J Respir Crit Care Med* **193**, 178-185, doi:10.1164/rccm.201503-0562oc (2016).

17 Solomon, J. J. & Fischer, A. Connective Tissue Disease-Associated Interstitial Lung Disease: A Focused Review. *J Intensive Care Med* **30**, 392-400, doi:10.1177/0885066613516579 (2015).

18 Fischer, A. *et al.* An official European Respiratory Society/American Thoracic Society research statement: Interstitial pneumonia with autoimmune features. *European Respiratory Journal* **46**, 976-987, doi:10.1183/13993003.00150-2015 (2015).

19 Perelas, A., Silver, R. M., Arrossi, A. V. & Highland, K. B. Systemic sclerosis-associated interstitial lung disease. *Lancet Respir Med* **8**, 304-320, doi:10.1016/S2213-2600(19)30480-1 (2020).

20 Koduri, G. *et al.* Interstitial lung disease has a poor prognosis in rheumatoid arthritis: results from an inception cohort. *Rheumatology (Oxford)* **49**, 1483-1489, doi:10.1093/rheumatology/keq035 (2010).

21 Iqbal, K. & Kelly, C. Treatment of rheumatoid arthritis-associated interstitial lung disease: a perspective review. *Ther Adv Musculoskelet Dis* **7**, 247-267, doi:10.1177/1759720x15612250 (2015).

22 Cottin, V. *et al.* Fibrosing interstitial lung diseases: knowns and unknowns. *Eur Respir Rev* **28**, 180100, doi:10.1183/16000617.0100-2018 (2019).

23 Vasakova, M., Morell, F., Walsh, S., Leslie, K. & Raghu, G. Hypersensitivity Pneumonitis: Perspectives in Diagnosis and Management. *Am J Respir Crit Care Med* **196**, 680-689, doi:10.1164/rccm.201611-2201pp (2017).

24 Cottin, V. *et al.* Presentation, diagnosis and clinical course of the spectrum of progressive-fibrosing interstitial lung diseases. *European Respiratory Review* **27**, doi:10.1183/16000617.0076-2018 (2018).

25 Kamp, D. W. Asbestos-induced lung diseases: an update. *Transl Res* **153**, 143-152, doi:10.1016/j.trsl.2009.01.004 (2009).

26 Wuyts, W. A. *et al.* The pathogenesis of pulmonary fibrosis: a moving target. *Eur Respir J* **41**, 1207-1218, doi:10.1183/09031936.00073012 (2013).

27 Yanagihara, T., Sato, S., Upagupta, C. & Kolb, M. What have we learned from basic science studies on idiopathic pulmonary fibrosis? *Eur Respir Rev* **28**, 190029, doi:10.1183/16000617.0029-2019 (2019).

28 Wynn, T. A. Integrating mechanisms of pulmonary fibrosis. *J Exp Med* **208**, 1339-1350, doi:10.1084/jem.20110551 (2011).

29 Bagnato, G. & Harari, S. Cellular interactions in the pathogenesis of interstitial lung diseases. *Eur Respir Rev* **24**, 102-114, doi:10.1183/09059180.00003214 (2015).

30   Wells, A. U. & Denton, C. P. Interstitial lung disease in connective tissue disease - Mechanisms and management. *Nat Rev Rheumatol* **10**, 728-739, doi:10.1038/nrrheum.2014.149 (2014).

31   Parimon, T., Yao, C., Stripp, B. R., Noble, P. W. & Chen, P. Alveolar Epithelial Type II Cells as Drivers of Lung Fibrosis in Idiopathic Pulmonary Fibrosis. *Int J Mol Sci* **21**, 2269, doi:10.3390/ijms21072269 (2020).

32   Willis, B. C. & Borok, Z. TGF-b-induced EMT: mechanisms and implications for fibrotic lung disease. *Am J Physiol Lung Cell Mol Physiol* **293**, L525-L534, doi:10.1152/ajplung.00163.2007 (2007).

33   Sisson, T. H. *et al.* Targeted Injury of type II alveolar epithelial cells induces pulmonary fibrosis. *Am J Respir Crit Care Med* **181**, 254-263, doi:10.1164/rccm.200810-1615oc (2010).

34   Scotton, C. J. & Chambers, R. C. Molecular targets in pulmonary fibrosis: the myofibroblast in focus. *Chest* **132**, 1311 (2007).

35   Phillips, R. J. *et al.* Circulating fibrocytes traffic to the lungs in response to CXCL12 and mediate fibrosis. *J Clin Invest* **114**, 438-446, doi:10.1172/jci200420997 (2004).

36   Piera-Velazquez, S., Li, Z. & Jimenez, S. A. Role of Endothelial-Mesenchymal Transition (EndoMT) in the Pathogenesis of Fibrotic Disorders. *Am J Pathol* **179**, 1074-1080, doi:10.1016/j.ajpath.2011.06.001 (2011).

37   Good, R. B. *et al.* Endothelial to Mesenchymal Transition Contributes to Endothelial Dysfunction in Pulmonary Arterial Hypertension. *Am J Pathol* **185**, 1850-1858, doi:10.1016/j.ajpath.2015.03.019 (2015).

38   Nataraj, D., Ernst, A. & Kalluri, R. Idiopathic pulmonary fibrosis is associated with endothelial to mesenchymal transition. *Am J Respir Cell Mol Biol* **43**, 129-130, doi:10.1165/rcmb.2010-0044ED (2010).

39   Jia, W., Wang, Z., Gao, C., Wu, J. & Wu, Q. Trajectory modeling of endothelial-to-mesenchymal transition reveals galectin-3 as a mediator in pulmonary fibrosis. *Cell Death Dis* **12**, 327-327, doi:10.1038/s41419-021-03603-0 (2021).

40   Moore, B. B. *et al.* CCR2-mediated recruitment of fibrocytes to the alveolar space after fibrotic injury. *Am J Pathol* **166**, 675-684, doi:10.1016/s0002-9440(10)62289-4 (2005).

41   Heukels, P., Moor, C. C., von der Thüsen, J. H., Wijsenbeek, M. S. & Kool, M. Inflammation and immunity in IPF pathogenesis and treatment. *Respir Med* **147**, 79-91, doi:10.1016/j.rmed.2018.12.015 (2019).

42   Suga, T., Sugiyama, Y. & Kitamura, S. Elevated Interleukin-8 in the Bronchoalveolar Lavage Fluid of Patients with Idiopathic Pulmonary Fibrosis. *J. Jpn. Soc. Respir. Endoscopy* **20**, 552-557, doi:10.18907/jjsre.20.7_552 (1998).

43   Mayadas, T. N., Cullere, X. & Lowell, C. A. The multifaceted functions of neutrophils. *Annu Rev Pathol* **9**, 181-218, doi:10.1146/annurev-pathol-020712-164023 (2014).

44   Gregory, A. D. *et al.* Neutrophil elastase promotes myofibroblast differentiation in lung fibrosis. *J Leukoc Biol* **98**, 143-152, doi:10.1189/jlb.3HI1014-493R (2015).

45   O'Dwyer, D. N., Ashley, S. L. & Moore, B. B. Influences of innate immunity, autophagy, and fibroblast activation in the pathogenesis of lung fibrosis. *Am J Physiol Lung Cell Mol Physiol* **311**, L590-L601, doi:10.1152/ajplung.00221.2016 (2016).

46   Gordon, S. & Martinez, F. O. Alternative Activation of Macrophages: Mechanism and Functions. *Immunity* **32**, 593-604, doi:10.1016/j.immuni.2010.05.007 (2010).

47   Ando, M. *et al.* Significance of Serum Vascular Endothelial Growth Factor Level in Patients with Idiopathic Pulmonary Fibrosis. *Lung* **188**, 247-252, doi:10.1007/s00408-009-9223-x (2010).

48   Schupp, J. C. *et al.* Macrophage activation in acute exacerbation of idiopathic pulmonary fibrosis. *PLoS One* **10**, e0116775-e0116775, doi:10.1371/journal.pone.0116775 (2015).

49   Somogyi, V. *et al.* The therapy of idiopathic pulmonary fibrosis: What is next? *Eur Respir Rev* **28**, 190021, doi:10.1183/16000617.0021-2019 (2019).

50   Richeldi, L. *et al.* Efficacy and Safety of Nintedanib in Idiopathic Pulmonary Fibrosis. *The New England Journal of Medicine* **370**, 2071-2082, doi:10.1056/NEJMoa1402584 (2014).

51   Wollin, L. *et al.* Mode of action of nintedanib in the treatment of idiopathic pulmonary fibrosis. *Eur Respir J* **45**, 1434-1445, doi:10.1183/09031936.00174914 (2015).

52   Ruwanpura, S. M., Thomas, B. J. & Bardin, P. G. Pirfenidone: Molecular mechanisms and potential clinical applications in lung disease. *Am J Respir Cell Mol Biol* **62**, 413-422, doi:10.1165/rcmb.2019-0328TR (2020).

53   Moore, B. B. & Hogaboam, C. M. Murine models of pulmonary fibrosis. *Am J Physiol Lung Cell Mol Physiol* **294**, L152-160, doi:10.1152/ajplung.00313.2007 (2008).

54   Liu, T., De Los Santos, F. G. & Phan, S. H. The bleomycin model of pulmonary fibrosis. *Methods in molecular biology (Clifton, N.J.)* **1627**, 27-42, doi:10.1007/978-1-4939-7113-8_2 (2017).

55   Moeller, A., Ask, K., Warburton, D., Gauldie, J. & Kolb, M. The bleomycin animal model: A useful tool to investigate treatment options for idiopathic pulmonary fibrosis? *The International Journal of Biochemistry & Cell Biology* **40**, 362-382, doi:10.1016/j.biocel.2007.08.011 (2008).

56   Gharaee-Kermani, M., Hatano, K., Nozaki, Y. & Phan, S. H. Gender-based differences in bleomycin-induced pulmonary fibrosis. *The American Journal of Pathology* **166**, 1593-1606, doi:10.1016/S0002-9440(10)62470-4 (2005).

57   Moore, B. B. *et al.* Animal models of fibrotic lung disease. *American Journal of Respiratory Cell and Molecular Biology* **49**, 167-179, doi:10.1165/rcmb.2013-0094TR (2013).

58   Degryse, A. L. *et al.* Repetitive intratracheal bleomycin models several features of idiopathic pulmonary fibrosis. *Am J Physiol Lung Cell Mol Physiol* **299**, L442-L452, doi:10.1152/ajplung.00026.2010 (2010).

59   Huaux, F. New developments in the understanding of immunology in silicosis. *Curr Opin Allergy Clin Immunol* **7**, 168-173, doi:10.1097/ACI.0b013e32802bf8a5 (2007).

60   Leung, C. C., Yu, I. T. S. & Chen, W. Silicosis. *The Lancet* **379**, 2008-2018, doi:10.1016/S0140-6736(12)60235-9 (2012).

61   Kawasaki, H. A mechanistic review of silica-induced inhalation toxicity. *Inhalation toxicology* **27**, 363-377, doi:10.3109/08958378.2015.1066905 (2015).

62   Pollard, K. M. Silica, silicosis, and autoimmunity. *Frontiers in Immunology* **7**, 1-7, doi:10.3389/fimmu.2016.00097 (2016).

63   Lakatos, H. F. *et al.* Oropharyngeal aspiration of a silica suspension produces a superior model of silicosis in the mouse when compared to intratracheal instillation. *Experimental lung research* **32**, 181-199, doi:10.1080/01902140600817465 (2006).

64   Hamilton, R. F., Thakur, S. A. & Holian, A. Silica binding and toxicity in alveolar macrophages. *Free Radical Biology and Medicine* **44**, 1246-1258, doi:10.1016/j.freeradbiomed.2007.12.027 (2008).

65   Carrington, R., Jordan, S., Pitchford, S. C. & Page, C. P. Use of animal models in IPF research. *Pulmonary Pharmacology & Therapeutics* **51**, 73-78, doi:10.1016/j.pupt.2018.07.002 (2018).

66   Cyphert, J. M. *et al.* Long-term response of rats to single intratracheal exposure of Libby amphibole or amosite. *J Toxicol Environ Health A* **75**, 183-200, doi:10.1080/15287394.2012.641203 (2012).

67   Tashiro, J. *et al.* Exploring Animal Models That Resemble Idiopathic Pulmonary Fibrosis. *Front. Med.* **4**, doi:10.3389/fmed.2017.00118 (2017).

68   Padilla-Carlin, D. J. *et al.* Pulmonary inflammatory and fibrotic responses in Fischer 344 rats after intratracheal instillation exposure to Libby amphibole. *J Toxicol Environ Health A* **74**, 1111-1132, doi:10.1080/15287394.2011.586940 (2011).

69   Bozelka, B. A. *et al.* A Murine Model of Asbestosis. **83**, 9-10, doi:10.1378/chest.83.5.9S (1983).

70   McDonald, S. *et al.* Pulmonary changes induced by combined mouse β-interferon (rMuIFN-β) and irradiation in normal mice — toxic versus protective effects. *Radiotherapy and Oncology* **26**, 212-218, doi:10.1016/0167-8140(93)90262-7 (1993).

71   Anuranjani & Bala, M. Concerted action of Nrf2-ARE pathway, MRN complex, HMGB1 and inflammatory cytokines - implication in modification of radiation damage. *Redox Biol* **2**, 832-846, doi:10.1016/j.redox.2014.02.008 (2014).

72   Douki, T. *et al.* Genotoxicity of combined exposure to polycyclic aromatic hydrocarbons and UVA--a mechanistic study. *Photochem Photobiol* **84**, 1133-1140, doi:10.1111/j.1751-1097.2008.00361.x (2008).

73   Campa, J. S., McAnulty, R. J. & Laurent, G. J. Application of high-pressure liquid chromatography to studies of collagen production by isolated cells in culture. *Anal Biochem* **186**, 257-263, doi:10.1016/0003-2697(90)90076-L (1990).

74   Kliment, C. R., Englert, J. M., Crum, L. P. & Oury, T. D. A novel method for accurate collagen and biochemical assessment of pulmonary tissue utilizing one animal. *Int J Clin Exp Pathol* **4**, 349-355 (2011).

75   De Langhe, E. *et al.* Quantification of lung fibrosis and emphysema in mice using automated micro-computed tomography. *PLoS One* **7**, e43123, doi:10.1371/journal.pone.0043123 (2012).

76   Ashcroft, T., Simpson, J. M. & Timbrell, V. Simple method of estimating severity of pulmonary fibrosis on a numerical scale. *Journal of Clinical Pathology* **41**, 467, doi:10.1136/jcp.41.4.467 (1988).

77   Cai, Y. & Kimura, S. Secretoglobin 3A2 exhibits anti-fibrotic activity in bleomycin-induced pulmonary fibrosis model mice. *PLoS One* **10**, e0142497, doi:10.1371/journal.pone.0142497 (2015).

78   McDonald, L. T., Johnson, S. D., Russell, D. L., Young, M. R. I. & LaRue, A. C. Role of a novel immune modulating DDR2-expressing population in silica-induced pulmonary fibrosis. *PLoS One* **12**, 1-14, doi:10.1371/journal.pone.0180724 (2017).

79   Hoymann, H. G. Invasive and noninvasive lung function measurements in rodents. *Journal of Pharmacological and Toxicological Methods* **55**, 16-26, doi:10.1016/j.vascn.2006.04.006 (2007).

80   Lomask, M. Further exploration of the Penh parameter. *Experimental and Toxicologic Pathology* **57**, 13-20, doi:10.1016/j.etp.2006.02.014 (2006).

81   Vanoirbeek, J. A. J. *et al.* Noninvasive and invasive pulmonary function in mouse models of obstructive and restrictive respiratory diseases. *American journal of respiratory cell and molecular biology* **42**, 96-104, doi:10.1165/rcmb.2008-0487OC (2010).

82   De Vleeschauwer, S. I. *et al.* Repeated invasive lung function measurements in intubated mice: an approach for longitudinal lung research. *Lab Anim* **45**, 81-89, doi:10.1258/la.2010.010111 (2011).

83   Bates Jason, H. & Irvin Charles, G. Measuring the lung function in the mouse: the challenge of size. *Respiratory Research* **4**, 4, doi:10.1186/rr199 (2003).

84   Hoymann, H.-G. New developments in lung function measurements in rodents. *Experimental and Toxicologic Pathology* **57**, 5-11, doi:10.1016/j.etp.2006.02.011 (2006).

85   Manali, E. D. *et al.* Static and dynamic mechanics of the murine lung after intratracheal bleomycin. *BMC Pulm Med* **11**, 33-33, doi:10.1186/1471-2466-11-33 (2011).

86   Shimbori, C., Shiota, N. & Okunishi, H. Involvement of leukotrienes in the pathogenesis of silica-induced pulmonary fibrosis in mice. *Experimental lung research* **36**, 292-301, doi:10.3109/01902140903585517 (2010).

87   Jarman, E. R. *et al.* A translational preclinical model of interstitial pulmonary fibrosis and pulmonary hypertension: mechanistic pathways driving disease pathophysiology. *Physiol Rep* **2**, e12133-n/a, doi:10.14814/phy2.12133 (2014).

88   Zhou, Y. *et al.* Noninvasive imaging of experimental lung fibrosis. *American Journal of Respiratory Cell and Molecular Biology* **53**, 8-13, doi:10.1165/rcmb.2015-0032TR (2015).

89   Vande Velde, G. *et al.* Longitudinal micro-CT provides biomarkers of lung disease and therapy in preclinical models, thereby revealing compensatory changes in lung volume. *Disease models & mechanisms* **9**, 91-98, doi:10.1242/dmm.020321 (2016).

90   Beckmann, N. & Maier, P.   47-57 (Berlin, Heidelberg: Springer Berlin Heidelberg, 2011).

91   Bell, R., Rudmann, C., Wood, R., Schwarz, E. & Rahimi, H. Longitudinal micro-CT as an outcome measure of interstitial lung disease in TNF-transgenic mice. *PLoS One* **13**, e0190678, doi:10.1371/journal.pone.0190678 (2018).

92   Kusaka, T. *et al.* Effect of silica particle size on macrophage inflammatory responses. *PLoS One* **9**, 1-9, doi:10.1371/journal.pone.0092634 (2014).

93   Choi, E. J. *et al.* Serial micro-CT assessment of the therapeutic effects of rosiglitazone in a bleomycin-induced lung fibrosis mouse model. *Korean Journal of Radiology* **15**, 448-455, doi:10.3348/kjr.2014.15.4.448 (2014).

94   Artaechevarria, X., Blanco, D., Pérez-martín, D., Torres, J. P. D. & Zulueta, J. J. Longitudinal study of a mouse model of chronic pulmonary inflammation using breath hold gated micro-CT. *European radiology* **20**, 2600-2608, doi:10.1007/s00330-010-1853-0 (2010).

95   Ruscitti, F. *et al.* Longitudinal assessment of bleomycin-induced lung fibrosis by micro-CT correlates with histological evaluation in mice. *Multidisciplinary Respiratory Medicine* **12**, 1-10, doi:10.1186/s40248-017-0089-0 (2017).

96   Haidekker, M. A. *Medical imaging technology*. 1st ed. 2013. edn, (New York, NY : Springer New York : Imprint Springer, 2013).

97   He, T., Qian, X., Zhai, R. & Yang, Z. Computed Tomography Number Measurement Consistency Under Different Beam Hardening Conditions: Comparison Between Dual-Energy Spectral Computed Tomography and Conventional Computed Tomography Imaging in Phantom Experiment. *J Comput Assist Tomogr* **39**, 981-985, doi:10.1097/RCT.0000000000000287 (2015).

98   Singh, H. & Neutze, J. A. *Radiology fundamentals*. Fourth Edition edn, 25-29 (New York, NY: Springer New York, 2012).

99   Poelmans, J. *et al.* Longitudinal, in vivo assessment of invasive pulmonary aspergillosis in mice by computed tomography and magnetic resonance imaging. *Laboratory investigation* **96**, 692-704, doi:10.1038/labinvest.2016.45 (2016).

100   Marien, E., Hillen, A., Vanderhoydonc, F., Swinnen, J. V. & Vande Velde, G. Longitudinal microcomputed tomography-derived biomarkers for lung metastasis detection in a syngeneic mouse model: added value to bioluminescence imaging. *Laboratory Investigation* **97**, 24-33, doi:10.1038/labinvest.2016.114 (2017).

101   Sasaki, M. *et al.* Evaluation of cigarette smoke- induced emphysema in mice using quantitative micro-computed tomography. *American journal of physiology. Lung cellular and molecular physiology* **308**, L1039, doi:10.1152/ajplung.00366.2014 (2015).

102   Lederlin, M. *et al.* In vivo micro-CT assessment of airway remodeling in a flexible OVA-sensitized murine model of asthma. *PLoS One* **7**, e48493, doi:10.1371/journal.pone.0048493 (2012).

103   Vande Velde, G. *et al.* Longitudinal micro-CT provides biomarkers of lung disease that can be used to assess the effect of therapy in preclinical mouse models, and reveal compensatory changes in lung volume. *Disease models & mechanisms* **9**, 91-98, doi:10.1242/dmm.020321 (2016).

104   Poelmans, J. *et al.* Longitudinal, in vivo assessment of invasive pulmonary aspergillosis in mice by computed tomography and magnetic resonance imaging. *Lab Invest* **96**, 692-704, doi:10.1038/labinvest.2016.45 (2016).

105   Vanherp, L. *et al.* The Added Value of Longitudinal Imaging for Preclinical In Vivo Efficacy Testing of Therapeutic Compounds against Cerebral Cryptococcosis. *Antimicrob Agents Chemother* **64**, doi:10.1128/AAC.00070-20 (2020).

106   Vanherp, L. *et al.* Sensitive bioluminescence imaging of fungal dissemination to the brain in mouse models of cryptococcosis. *Disease models & mechanisms* **12**, doi:10.1242/dmm.039123 (2019).

107   Salaets, T. *et al.* Local pulmonary drug delivery in the preterm rabbit: feasibility and efficacy of daily intratracheal injections. *American journal of physiology. Lung cellular and molecular physiology* **316**, L589-L597, doi:10.1152/ajplung.00255.2018 (2019).

108   Tsui, H. C. *et al.* Cobalt exposure via skin alters lung immune cells and enhances pulmonary responses to cobalt in mice. *American journal of physiology. Lung cellular and molecular physiology*, doi:10.1152/ajplung.00265.2020 (2020).

109   Van Den Broucke, S. *et al.* Irritant-induced asthma to hypochlorite in mice due to impairment of the airway barrier. *Arch Toxicol* **92**, 1551-1561, doi:10.1007/s00204-018-2161-8 (2018).

110   Cavanaugh, D. *et al.* Quantification of bleomycin-induced murine lung damage in vivo with micro-computed tomography. *Acad Radiol* **13**, 1505-1512, doi:10.1016/j.acra.2006.08.011 (2006).

111   Rodt, T. *et al.* Micro-computed tomography of pulmonary fibrosis in mice induced by adenoviral gene transfer of biologically active transforming growth factor-[beta]1. *Respiratory Research* **11**, 181, doi:10.1186/1465-9921-11-181 (2010).

112   Persson, I. M. *et al.* Imaging Biomarkers and Pathobiological Profiling in a Rat Model of Drug-Induced Interstitial Lung Disease Induced by Bleomycin. *Frontiers in Physiology* **11**, doi:10.3389/fphys.2020.00584 (2020).

113   Sensen, C. W. a. B. H. *Advanced Imaging in Biology and Medicine*. (Springer, 2008).

114   Brouwers, J. E. M., Lambers, F. M., Rietbergen, v. B. & Huiskes, R. No effects of in vivo micro-CT radiation on structural parameters and bone marrow cells in proximal tibia in Wistar rats detected after eight weekly scans. *J Orthop Res* **25**, 1325-1332, doi:10.1002/jor.20439 (2007).

115   Cavanaugh, D. *et al.* In Vivo Respiratory-Gated Micro-CT Imaging in Small-Animal Oncology Models. *Molecular Imaging* **3**, doi:10.1162/15353500200403184 (2004).

116   Erin, B. W. Improved method of in vivo respiratory-gated micro-ct imaging. *Physics in Medicine and Biology* **49**, 4163-4172, doi:10.1088/0031-9155/49/17/023 (2004).

117   Brown, R. H., Walters, D. M., Greenberg, R. S. & Mitzner, W. A method of endotracheal intubation and pulmonary functional assessment for repeated studies in mice. *Journal of applied physiology (Bethesda, Md. : 1985)* **87**, 2362-2365, doi:10.1152/jappl.1999.87.6.2362 (1999).

118   Namati, E. *et al.* In vivo micro-CT lung imaging via a computer-controlled intermittent iso-pressure breath hold (IIBH) technique. *Physics in medicine and biology* **51**, 6061-6075, doi:10.1088/0031-9155/51/23/008 (2006).

119   Artaechevarria, X. *et al.* Longitudinal study of a mouse model of chronic pulmonary inflammation using breath hold gated micro-CT. *European radiology* **20**, 2600-2608, doi:10.1007/s00330-010-1853-0 (2010).

120   Kuntz, J. *et al.* Fully automated intrinsic respiratory and cardiac gating for small animal ct. *Physics in Medicine and Biology* **55**, 2069-2085, doi:10.1088/0031-9155/55/7/018 (2010).

121   Marenzana, M. & Vande Velde, G. Refine, reduce, replace: Imaging of fibrosis and arthritis in animal models. *Best Practice and Research: Clinical Rheumatology* **29**, 715-740, doi:10.1016/j.berh.2016.02.001 (2015).

122   Saito, S. & Murase, K. Detection and early phase assessment of radiation-induced lung injury in mice using micro-CT. *PLoS One* **7**, e45960, doi:10.1371/journal.pone.0045960 (2012).

123   Iwakawa, M. N., S.; Ohta, T.; Oohira, C.; Tanaka, H.; Tsuji, A.; Ishikawa, A.; Imai, T. Strain dependent differences in a histological study of CD44 and collagen fibers with an expression analysis of inflammatory response-related genes in irradiated murine lung. *J Radiat Res* **45**, 423-433 (2004).

124   Plathow, C. *et al.* Computed tomography monitoring of radiation-induced lung fibrosis in mice. *Investigative radiology* **39**, 600-609, doi:10.1097/01.rli.0000138134.89050.a5 (2004).

125   Granton, P. V. *et al.* A longitudinal evaluation of partial lung irradiation in mice by using a dedicated image-guided small animal irradiator. *International Journal of Radiation Oncology, Biology, Physics* **90**, 696-704, doi:10.1016/j.ijrobp.2014.07.004 (2014).

126   Brenner, D. J. & Hall, E. J. Computed tomography--an increasing source of radiation exposure. *N Engl J Med* **357**, 2277-2284, doi:10.1056/nejmra072149 (2007).

127   Vande Velde, G. *et al.* Longitudinal in vivo microcomputed tomography of mouse lungs: No evidence for radiotoxicity. *American Journal of Physiology-Lung Cellular and Molecular Physiology* **309**, L271-279, doi:10.1152/ajplung.00098.2015 (2015).

128   Vande Velde, G. *et al.* Magnetic resonance imaging for noninvasive assessment of lung fibrosis onset and progression: cross-validation and comparison of different magnetic resonance imaging protocols with micro-computed tomography and histology in the bleomycin-induced mouse model. *Investigative radiology* **49**, 691-698, doi:10.1097/RLI.0000000000000071 (2014).

129   Jacob, R. E., Amidan, B. G., Soelberg, J. & Minard, K. R. In vivo MRI of altered proton signal intensity and T2 relaxation in a bleomycin model of pulmonary inflammation and fibrosis. *J Magn Reson Imaging* **31**, 1091-1099, doi:10.1002/jmri.22166 (2010).

130   Cutillo, A. G. *et al.* Characterization of bleomycin lung injury by nuclear magnetic resonance: Correlation between NMR relaxation times and lung water and collagen content. *Magnetic Resonance in Medicine* **47**, 246-256, doi:10.1002/mrm.10082 (2002).

131   Kersjes, W. *et al.* Differentiation of Alveolitis and Pulmonary Fibrosis in Rabbits With Magnetic Resonance Imaging After Intrabronchial Administration of Bleomycin. *Invest Radiol* **34**, 13-21, doi:10.1097/00004424-199901000-00003 (1999).

132   Egger, C. *et al.* Administration of bleomycin via the oropharyngeal aspiration route leads to sustained lung fibrosis in mice and rats as quantified by UTE-MRI and histology. *PLoS One* **8**, e63432-e63432, doi:10.1371/journal.pone.0063432 (2013).

133   Shea, B. S. *et al.* Uncoupling of the profibrotic and hemostatic effects of thrombin in lung fibrosis. *JCI Insight* **2**, doi:10.1172/jci.insight.86608 (2017).

134   Waghorn, P. A. *et al.* Molecular Magnetic Resonance Imaging of Lung Fibrogenesis with an Oxyamine-Based Probe. *Angewandte Chemie (International ed.)* **56**, 9825-9828, doi:10.1002/anie.201704773 (2017).

135   Désogère, P., Montesi, S. B. & Caravan, P. Molecular Probes for Imaging Fibrosis and Fibrogenesis. *Chemistry* **25**, 1128-1141, doi:10.1002/chem.201801578 (2019).

136   Désogère, P. *et al.* Type I collagen-targeted PET probe for pulmonary fibrosis detection and staging in preclinical models. *Sci Transl Med* **9**, eaaf4696, doi:10.1126/scitranslmed.aaf4696 (2017).

137   Wester, H.-J. *et al.* Preclinical evaluation of 4-[18F]fluoroprolines: diastereomeric effect on metabolism and uptake in mice. *Nucl Med Biol* **26**, 259-265, doi:10.1016/S0969-8051(98)00107-3 (1999).

138   Wallace, W. E. *et al.* Cis-4-[(18)F]fluoro-L-proline PET imaging of pulmonary fibrosis in a rabbit model. *J Nucl Med* **43**, 413 (2002).

139   Jones, H. A. *et al.* Positron emission tomography in the quantification of cellular and biochemical responses to intrapulmonary particulates. *Toxicol Appl Pharmacol* **207**, 230-236, doi:10.1016/j.taap.2005.02.027 (2005).

140   Withana, N. P. *et al.* Non-invasive Imaging of Idiopathic Pulmonary Fibrosis Using Cathepsin Protease Probes. *Sci Rep* **6**, 19755, doi:10.1038/srep19755 (2016).

141   Ciarrocchi, E. & Belcari, N. Cerenkov luminescence imaging: physics principles and potential applications in biomedical sciences. *EJNMMI Phys* **4**, 1-31, doi:10.1186/s40658-017-0181-8 (2017).
142   Sato, A., Klaunberg, B. & Tolwani, R. In Vivo Bioluminescence Imaging. *Comparative Medicine* **54**, 631-634 (2004).
143   Gammon, S. T. *et al.* Preclinical anatomical, molecular, and functional imaging of the lung with multiple modalities. *Am J Physiol Lung Cell Mol Physiol* **306**, L897-L914, doi:10.1152/ajplung.00007.2014 (2014).
144   Stellari, F. F. *et al.* Heterologous Matrix Metalloproteinase Gene Promoter Activity Allows In Vivo Real-time Imaging of Bleomycin-Induced Lung Fibrosis in Transiently Transgenized Mice. **8**, doi:10.3389/fimmu.2017.00199 (2017).
145   Sasaki, M. *et al.* Evaluation of cigarette smoke- induced emphysema in mice using quantitative micro- computed tomography. *American journal of physiology. Lung cellular and molecular physiology* **308**, L1039, doi:10.1152/ajplung.00366.2014 (2015).
146   Ruscitti, F. *et al.* Longitudinal assessment of bleomycin-induced lung fibrosis by micro-CT correlates with histological evaluation in mice.(Report). *Multidisciplinary Respiratory Medicine* **12**, doi:10.1186/s40248-017-0089-0 (2017).
147   Blandinières, A. *et al.* Endothelial Colony-Forming Cells Do Not Participate to Fibrogenesis in a Bleomycin-Induced Pulmonary Fibrosis Model in Nude Mice. **14**, 812-822, doi:10.1007/s12015-018-9846-5 (2018).
148   Bell, R. D., Rudmann, C., Wood, R. W., Schwarz, E. M. & Rahimi, H. Longitudinal micro-CT as an outcome measure of interstitial lung disease in TNF-transgenic mice. *PloS one* **13**, e0190678-e0190678, doi:10.1371/journal.pone.0190678 (2018).
149   Plathow, C. L., M.; Gong, P.; Zieher, H.; Kiessling, F.; Peschke, P.; Kauczor, HU.; & Abdollahi, A. H., PE. Computed tomography monitoring of radiation-induced lung fibrosis in mice. . *Invest Radiol* **39**, 600-609 (2004).
150   Detombe, S. D.-B., J.; Petrov, IE.; Drangova, M. X-ray dose delivered during a longitudinal micro-CT study has no adverse effect on cardiac and pulmonary tissue in C57BL/6 mice. *Acta Radiol* **54**, 435-441 (2013).
151   Graves, P. R., Siddiqui, F., Anscher, M. S. & Movsas, B. Radiation pulmonary toxicity: from mechanisms to management. *Semin Radiat Oncol* **20**, 201-207, doi:10.1016/j.semradonc.2010.01.010 (2010).
152   Vande Velde, G. D. L., E.; Poelmans, J.; Dresselaers, T.; Lories, R. J.; Himmelreich, U. . Magnetic resonance imaging for noninvasive assessment of lung fibrosis onset and progression: cross-validation and comparison of different magnetic resonance imaging protocols with micro-computed tomography and histology in the bleomycin-induced mouse model. *Invest Radiol* **49**, 691-698 (2014).
153   Commission., I. E. Medical diagnostic X-ray equipment-radiation conditions for use in the determination of characteristics. *IEC 61267* (2005).
154   Woessner, J. F. The determination of hydroxyproline in tissue and protein samples containing small proportions of this imino acid. *Archives of Biochemistry and Biophysics* **93**, 440-447, doi:10.1016/0003-9861(61)90291-0 (1961).
155   E., C. S. R. S. J. A. P. M. Physics in Nuclear Medicine. *Elsevier Science, Pennsylvania*, 264 (2003).
156   Rose, A. *Vision : human and electronic*. (New York (N.Y.) : Plenum, 1973).
157   Walkin, L. *et al.* The role of mouse strain differences in the susceptibility to fibrosis: a systematic review. *Fibrogenesis & tissue repair* **6**, 18-18, doi:10.1186/1755-1536-6-18 (2013).
158   Trowell, O. A. The sensitivity of lymphocytes to ionising radiation. *J Pathol Bacteriol* **64**, 687-704 (1952).
159   Imai, Y. & Nakao, I. In vivo radiosensitivity and recovery pattern of the hematopoietic precursor cells and stem cells in mouse bone marrow. *Exp Hematol.* **15**, 5 (1987).
160   Morowski, M. *et al.* Only severe thrombocytopenia results in bleeding and defective thrombus formation in mice. *Blood* **121**, 4938, doi:10.1182/blood-2012-10-461459 (2013).
161   O'Connell, K. E. *et al.* Practical murine hematopathology: a comparative review and implications for research. *Comparative medicine* **65**, 96-113 (2015).
162   Laperre, K. *et al.* Development of micro-CT protocols for in vivo follow-up of mouse bone architecture without major radiation side effects. *Bone* **49**, 613-622, doi:https://doi.org/10.1016/j.bone.2011.06.031 (2011).
163   Miyahara, N. *et al.* Evaluation of X-ray doses and their corresponding biological effects on experimental animals in cone-beam micro-CT scans (R-mCT2). *Radiol Phys Technol* **9**, 60-68, doi:10.1007/s12194-015-0334-1 (2016).
164   Seibold, J. R. *et al.* Randomized, prospective, placebo-controlled trial of bosentan in interstitial lung disease secondary to systemic sclerosis. *Arthritis and Rheumatism* **62**, 2101-2108, doi:10.1002/art.27466 (2010).
165   Chua, F., Gauldie, J. & Laurent, G. Pulmonary Fibrosis: Searching for Model Answers. *American Journal of Respiratory Cell and Molecular Biology* **33**, 9-13 (2005).
166   Devos, F. C. *et al.* Forced expiration measurements in mouse models of obstructive and restrictive lung diseases. *Respiratory Research* **18**, 1-14, doi:10.1186/s12931-017-0610-1 (2017).
167   De Vooght, V. *et al.* Oropharyngeal aspiration: an alternative route for challenging in a mouse model of chemical-induced asthma. *Toxicology* **259**, 84-89, doi:10.1016/j.tox.2009.02.007 (2009).
168   Riley, L. & Urbine, D. Chronic Silicosis with Progressive Massive Fibrosis. *The New England Journal of Medicine* **380**, 2256, doi:10.1056/NEJMicm1809675 (2019).
169   Cavalin, C. *et al.* Beyond silicosis, is the world failing on silica hazards? *The Lancet Respiratory Medicine* **7**, 649-650, doi:10.1016/S2213-2600(19)30174-2 (2019).
170   The Lancet Respiratory, M. The world is failing on silicosis. *The Lancet Respiratory Medicine* **7**, doi:10.1016/S2213-2600(19)30078-5 (2019).
171   Johnston, C. J., Wright, T., Rubin, P. & Finkelstein, J. Alterations in the expression of chemokine mRNA levels in fibrosis-resistant and -sensitive mice after thoracic irradiation. *Experimental Lung Research* **24**, 321-337 (1998).

172   Davis, G., Leslie, K. & Hemenway, D. Silicosis in mice: effects of dose, time, and genetic strain. *Journal of Environmental Pathology, Toxicology and Oncology* **17**, 17 (1998).

173   Barbarin, V. *et al.* The role of pro- and anti-inflammatory responses in silica-induced lung fibrosis. *Respiratory research* **6**, 112-112, doi:10.1186/1465-9921-6-112 (2005).

174   Du, S. *et al.* Dioscin alleviates crystalline silica-induced pulmonary inflammation and fibrosis through promoting alveolar macrophage autophagy. *Theranostics* **9**, 1878-1892, doi:10.7150/thno.29682 (2019).

175   Liu, H. *et al.* BBC3 in macrophages promoted pulmonary fibrosis development through inducing autophagy during silicosis. *Cell Death and Disease* **8**, e2657-e2657, doi:10.1038/cddis.2017.78 (2017).

176   Ferreira, T. P. T. *et al.* IL-13 immunotoxin accelerates resolution of lung pathological changes triggered by silica particles in mice. *Journal of Immunology*, doi:10.4049/jimmunol.1203551 (2013).

177   Trentin, P. G. *et al.* Annexin A1 mimetic peptide controls the inflammatory and fibrotic effects of silica particles in mice. *British Journal of Pharmacology* **172**, 3058-3071, doi:10.1111/bph.13109 (2015).

178   Liu, S. *et al.* Silica particles mediate phenotypic and functional alteration of dendritic cells and induce Th2 cell polarization. *Frontiers in immunology* **10**, 787, doi:10.3389/fimmu.2019.00787 (2019).

179   Allahverdian, S., Harada, N., Singhera, G. K., Knight, D. A. & Dorscheid, D. R. Secretion of IL-13 by airway epithelial cells enhances epithelial repair via HB-EGF. *American journal of respiratory cell and molecular biology* **38**, 153-160, doi:10.1165/rcmb.2007-0173OC (2008).

180   Mi, S. *et al.* Blocking IL-17A promotes the resolution of pulmonary inflammation and fibrosis via TGF-beta1-dependent and -independent mechanisms. *Journal of immunology* **187**, 3003, doi:10.4049/jimmunol.1004081 (2011).

181   Bridges, J. P. *et al.* Pulmonary surfactant proteins A and D are potent endogenous inhibitors of lipid peroxidation and oxidative cellular injury. *The Journal of biological chemistry* **275**, 38848-38855, doi:10.1074/jbc.M005322200 (2000).

182   Davis, G. S. The Pathogenesis of Silicosis: State of the Art. *Chest Journal* **89**, 166S-169S, doi:10.1378/chest.89.3_Supplement.166S (1986).

183   Barbayianni, I., Ninou, I., Tzouvelekis, A. & Aidinis, V. Bleomycin revisited: a direct comparison of the intratracheal micro-spraying and the oropharyngeal aspiration routes of bleomycin administration in mice. *Frontiers in Medicine* **5**, doi:10.3389/fmed.2018.00269 (2018).

184   Vanherp, L. *et al.* Sensitive bioluminescence imaging of fungal dissemination to the brain in mouse models of cryptococcosis. *Disease models & mechanisms* **12**, doi:10.1242/dmm.039123 (2019).

185   Egger, C. *et al.* Lung volume quantified by MRI reflects extracellular-matrix deposition and altered pulmonary function in bleomycin models of fibrosis: effects of SOM230. *American Journal of Physiology* **306**, L1064, doi:10.1152/ajplung.00027.2014 (2014).

186   Wollin, L., Maillet, I., Quesniaux, V., Holweg, A. & Ryffel, B. Antifibrotic and Anti-inflammatory Activity of the Tyrosine Kinase Inhibitor Nintedanib in Experimental Models of Lung Fibrosis. *Journal of Pharmacology and Experimental Therapeutics* **349**, 209-220, doi:10.1124/jpet.113.208223 (2014).

187   Huang, J. *et al.* Nintedanib inhibits macrophage activation and ameliorates vascular and fibrotic manifestations in the Fra2 mouse model of systemic sclerosis. *Annals of the Rheumatic Diseases* **76**, 1941-1948, doi:10.1136/annrheumdis-2016-210823 (2017).

188   Ackermann, M. *et al.* Effects of nintedanib on the microvascular architecture in a lung fibrosis model. *Angiogenesis* **20**, 359-372, doi:10.1007/s10456-017-9543-z (2017).

189   Dekoster, K. *et al.* Longitudinal micro-computed tomography-derived biomarkers quantify non-resolving fibrosis in a silicosis mouse model. *Scientific Reports* (2020).

190   Azmoonfar, R. *et al.* Metformin Protects against Radiation-Induced Pneumonitis and Fibrosis and Attenuates Upregulation of Dual Oxidase Genes Expression. *Advanced pharmaceutical bulletin* **8**, 697-704, doi:10.15171/apb.2018.078 (2018).

191   Urushiyama, H. *et al.* Naftopidil reduced the proliferation of lung fibroblasts and bleomycin-induced lung fibrosis in mice. *J Cell Mol Med* **23**, 3563-3571, doi:10.1111/jcmm.14255 (2019).

192   Ruscitti, F. *et al.* Quantification of Lung Fibrosis in IPF-Like Mouse Model and Pharmacological Response to Treatment by Micro-Computed Tomography. *Frontiers in pharmacology* **11**, doi:10.3389/fphar.2020.01117 (2020).

193   Bickelhaupt, S. *et al.* Effects of CTGF Blockade on Attenuation and Reversal of Radiation-Induced Pulmonary Fibrosis. *J Natl Cancer Inst* **109**, djw339, doi:10.1093/jnci/djw339 (2017).

194   De Ruysscher, D. *et al.* Nintedanib reduces radiation-induced microscopic lung fibrosis but this cannot be monitored by CT imaging: A preclinical study with a high precision image-guided irradiator. *Radiother Oncol* **124**, 482-487, doi:10.1016/j.radonc.2017.07.014 (2017).

195   Berghen, N. *et al.* Radiosafe micro-computed tomography for longitudinal evaluation of murine disease models. *Scientific reports* **9**, 17598-17598, doi:10.1038/s41598-019-53876-x (2019).

196   Zosky, G. & Sly, P. D. in *Clin. Exp. Allergy* Vol. 37   973-988 (2007).

197   Dawkins, P. A. & Stockley, R. in *Thorax* Vol. 56   972-977 (2001).

198   Glaab, T., Taube, C., Braun, A. & Mitzner, W. Invasive and noninvasive methods for studying pulmonary function in mice. *Respiratory research* **8**, 63-63 (2007).

199   Bates, J. & Irvin, C. G. Measuring lung function in mice: the phenotyping uncertainty principle. *J. Appl. Physiol.* **94**, 1297-1306, doi:10.1152/japplphysiol.00706.2002 (2003).

200   Lederlin, M. *et al.* Airway remodeling in a mouse asthma model assessed by in-vivo respiratory-gated micro-computed tomography. *European Radiology* **20**, 128-137, doi:10.1007/s00330-009-1541-0 (2010).

201   Tsui, H.-C. *et al.* Cobalt exposure via skin alters lung immune cells and enhances pulmonary responses to cobalt in mice. *American journal of physiology. Lung cellular and molecular physiology* **319**, L641-L651, doi:10.1152/AJPLUNG.00265.2020 (2020).

202   Chavarrías, C. *et al.* Extraction of the respiratory signal from small-animal ct projections for a retrospective gating method. *Physics in Medicine and Biology* **53**, 4683-4695, doi:10.1088/0031-9155/53/17/015 (2008).

203   Van Den Broucke, S. *et al.* Irritant-induced asthma to hypochlorite in mice due to impairment of the airway barrier. *Archives of Toxicology* **92**, 1551-1561, doi:10.1007/s00204-018-2161-8 (2018).

204   Voelz, K., Johnston, S. A., Rutherford, J. C. & May, R. C. Automated analysis of cryptococcal macrophage parasitism using GFP-tagged cryptococci. *PloS one* **5**, e15968, doi:10.1371/journal.pone.0015968 (2010).

205   Bates Jason, H. *Lung Mechanics An Inverse Modeling Approach*. (Cambridge University Press, 2009).

206   Constantinides, C., Mean, R. & Janssen, B. J. Effects of Isoflurane Anesthesia on the Cardiovascular Function of the C57BL/6 Mouse. *ILAR J* **52**, e21-31 (2011).

207   Groeben, H., Meier, S., Tankersley, C. G., Mitzner, W. & Brown, R. H. Influence of volatile anaesthetics on hypercapnoeic ventilatory responses in mice with blunted respiratory drive. *Br J Anaesth* **92**, 697-703, doi:10.1093/bja/aeh124 (2004).

208   Heulens, N. *et al.* Vitamin D deficiency exacerbates COPD-like characteristics in the lungs of cigarette smoke-exposed mice. *Respir Res* **16**, 110-110, doi:10.1186/s12931-015-0271-x (2015).

209   Chetta, A., Marangio, E. & Olivieri, D. Pulmonary Function Testing in Interstitial Lung Diseases. *Respiration* **71**, 209-213, doi:10.1159/000077416 (2004).

210   Barreiro, T. J. & Perillo, I. An approach to interpreting spirometry. *Am Fam Physician* **69**, 1107 (2004).

211   Pierce, R. Spirometry: an essential clinical measurement. *Aust Fam Physician* **34**, 535-539, doi:10.2267/0300-8495.34.7.1824 (2005).

212   Kuo, L. J. Y., L. X. Gamma-H2AX - a novel biomarker for DNA double-strand breaks. *In Vivo* **22**, 305-309 (2008).

213   Brehm, M., Sawall, S., Maier, J., Sauppe, S. & Kachelrieß, M. Cardiorespiratory motion- compensated micro- CT image reconstruction using an artifact model- based motion estimation. *Medical Physics* **42**, 1948-1958, doi:10.1118/1.4916083 (2015).

214   Maier, J., Sawall, S. & Kachelrieß, M. Assessment of dedicated low-dose cardiac micro-CT reconstruction algorithms using the left ventricular volume of small rodents as a performance measure. *Med Phys* **41**, 051908-n/a, doi:10.1118/1.4870983 (2014).

215   Ritschl, L., Sawall, S., Knaup, M., Hess, A. & Kachelrieß, M. Iterative 4D cardiac micro-CT image reconstruction using an adaptive spatio-temporal sparsity prior. *Phys. Med. Biol* **57**, 1517-1525, doi:10.1088/0031-9155/57/6/1517 (2012).

216   Sawall, S. *et al.* Low-dose cardio-respiratory phase-correlated cone-beam micro-CT of small animals. *Med Phys* **38**, 1416-1424, doi:10.1118/1.3551993 (2011).

217   Jonckheere, A.-C. *et al.* Innate lymphoid cells contribute to induction of airway hyperreactivity in a murine neutrophilic astma model [accepted]. *Frontiers Immunology* (2022).

218   Rackley, C. R. & Stripp, B. R. Building and maintaining the epithelium of the lung. *J Clin Invest* **122**, 2724-2730, doi:10.1172/JCI60519 (2012).

219   Izbicki, G., Segel, M. J., Christensen, T. G., Conner, M. W. & Breuer, R. Time course of bleomycin-induced lung fibrosis. *Int J Exp Pathol* **83**, 111-119, doi:10.1046/j.1365-2613.2002.00220.x (2002).

220   Ravanetti, F. *et al.* Modeling pulmonary fibrosis through bleomycin delivered by osmotic minipump: A new histomorphometric method of evaluation. *Am J Physiol Lung Cell Mol Physiol* **318**, L376-L385, doi:10.1152/AJPLUNG.00311.2019 (2020).

221   Wong, B. A. Inhalation Exposure Systems: Design, Methods and Operation. *Toxicol Pathol* **35**, 3-14, doi:10.1080/01926230601060017 (2007).

222   Driscoll, K. E. *et al.* Intratracheal Instillation as an Exposure Technique for the Evaluation of Respiratory Tract Toxicity: Uses and Limitations. *Toxicol. Sci* **55**, 24-35, doi:10.1093/toxsci/55.1.24 (2000).

223   Southam, D. S., Dolovich, M., O'Byrne, P. M. & Inman, M. D. Distribution of intranasal instillations in mice: effects of volume, time, body position, and anesthesia. *American Journal of Physiology - Lung Cellular and Molecular Physiology* **282**, L833-L839, doi:10.1152/ajplung.00173.2001 (2002).

224   Mayeux, J. M., Kono, D. H. & Pollard, K. M. Development of experimental silicosis in inbred and outbred mice depends on instillation volume. *Sci Rep* **9**, 14190-14110, doi:10.1038/s41598-019-50725-9 (2019).

225   Jobse, B. N., Rhem, R. G., McCurry, C. A. J. R., Wang, I. Q. & Labiris, N. R. Imaging lung function in mice using SPECT/CT and per-voxel analysis. *PLoS One* **7**, e42187-e42187, doi:10.1371/journal.pone.0042187 (2012).

226   Young, H. M., Eddy, R. L. & Parraga, G. MRI and CT lung biomarkers: Towards an in vivo understanding of lung biomechanics. *Clin Biomech (Bristol, Avon)* **66**, 107-122, doi:10.1016/j.clinbiomech.2017.09.016 (2019).

227   Werner, R., Ehrhardt, J., Schmidt, R. & Handels, H. Patient-specific finite element modeling of respiratory lung motion using 4D CT image data. *Med Phys* **36**, 1500-1511, doi:10.1118/1.3101820 (2009).

228   Hasse, K. *et al.* Feasibility of deriving a novel imaging biomarker based on patient-specific lung elasticity for characterizing the degree of COPD in lung SBRT patients. *Br J Radiol* **92**, 20180296-20180296, doi:10.1259/bjr.20180296 (2019).

229   Khan, A. *et al.* Simple low dose radiography allows precise lung volume assessment in mice. *Sci Rep* **11**, 4163-4163, doi:10.1038/s41598-021-83319-5 (2021)**.**

Summary

Pulmonary fibrosis is the replacement of healthy tissue by an excessive deposition of extracellular matrix components leading to an irreversible destruction of the lung architecture. It is a devastating condition resulting in a decreased lung compliance, disrupted gas exchange and respiratory failure. Currently, there are two therapeutics on the market that slow down the progression of pulmonary fibrosis. Regardless many efforts made in the past, there is still no curative treatment available. As such, pulmonary fibrosis remains a life-threatening condition. Therefore, in this thesis, in order to improve state-of-the-art approaches in preclinical pulmonary fibrosis research towards new therapies and targets, we aimed to (1) implement safe and repeated low-dose μCT, (2) optimize an image-compatible, stable and non-resolving pulmonary fibrosis mouse model, (3) evaluate the relevance of μCT in preclinical therapy studies and (4) extract lung function biomarkers from longitudinal μCT data of free-breathing mice with different lung pathologies.

By weekly scanning murine models of lung metastasis, inflammation and fibrosis with μCT and comparing 5-times weekly scanned animals with unscanned controls, we found no influence of μCT on lung metastasis load nor on healthy mice. We saw a disease-independent reduction in circulating blood platelets and lymphocytes when using a 4D μCT protocol, which we could eliminate by altering our protocol to 3D μCT thereby reducing the delivered dose by two-thirds. We established that consecutive scanning with μCT was safe to use in different murine models.

Next, we established a silicosis mouse model of pulmonary fibrosis by oropharyngeal instillation of silica particles in mice. After instillation, these animals were monitored by *in vivo* μCT. Our μCT-derived morphological biomarkers were able to monitor the early onset of inflammatory and long-term non-resolving pulmonary fibrosis in this silicosis mouse model.

Additionally, we used a commercially available therapeutic, Nintedanib, to validate μCT for preclinical therapy testing. Nintedanib treatment slightly decreased the non-aerated lung volume in both treatment regimes, while it increased the aerated and total lung volume as assessed by μCT. Although Nintedanib only showed a small treatment effect and the severity of the mouse model was only minor, there was a good agreement between *in vivo* μCT biomarkers and *ex vivo* readouts (e.g. flexiVent, histology and inflammatory markers).

At last, we explored novel functional biomarkers derived from an in vivo 4D μCT scan: the tidal volume and centre of tidal volume. These biomarkers allow non-invasive follow-up of lung function in mice and are complementary to other invasive endpoint methods. This last part further emphasized the need of μCT to evaluate preclinical lung disease models.

To conclude, with this thesis, we provided substantial evidence to implement μCT to the routine workflow for preclinical lung fibrosis research, thereby improving preclinical assessment of therapeutics and solving the gap between bench and bedside translatability.

Scientific acknowledgement, personal contributions and conflict of interest statement

Scientific acknowledgements

I would like to thank Jorien Derycke for her help with the animal experiments during her master thesis. I would also like to thank Nathalie Berghen for her help with the hydroxyproline assays and histology of chapter 4. At last, I would like to thank Tatjana Decaesteker and Anne-Charlotte Jonckheere for their help with the inflammatory and permeability evaluations of chapter 4.

Personal contribution

Chapter 1, 2 and 7: Kaat Dekoster drafted the chapters.

Chapter 3: Dr. Eyra Marien performed "experiment 1". Dr. Nathalie Berghen performed "experiment 2" with the help of Jasmine Deferme, Thibault Vosselman, Eline Tiest, Marleen Lox and Prof. Ellen De Langhe. Prof. Greetje Vande Velde performed "experiment 3 and 5" with the help of Amy Hillen, Jens Wouters and Kaat Dekoster. Kaat Dekoster performed "experiment 4" with the help of Jens Wouters. Dr. Jeremie Dabin performed the dosimetry experiments and analysis. Kaat Dekoster analyzed μCT data of "experiment 1-5". Kaat Dekoster and Dr. Nathalie Berghen analyzed blood cell count data of "experiment 1-5". Kaat Dekoster and Dr. Nathalie Berghen drafted the manuscript together.

Chapter 4: Kaat Dekoster performed all experiments and analyzed all data. Prof. Erik Verbeken provided the histology. Lung function measurements were performed with the assistance of Prof. Jeroen Vanoirbeek, Dr. Sofie Van den Broucke and Dr. Tatjana Decaesteker. Kaat Dekoster drafted the manuscript.

Chapter 5: Kaat Dekoster and Jorien Derycke performed the *in vivo* experiments. Kaat Dekoster performed the *ex vivo* experiments. Prof. Erik Verbeken provided histology. Lung function measurements were performed with the assistance of Prof. Jeroen Vanoirbeek and Dr. Anne-Charlotte Jonckheere. Jorien Derycke analyzed the μCT scans. Kaat Dekoster analyzed the data and drafted the manuscript.

Chapter 6: Kaat Dekoster analyzed all μCT data and drafted the manuscript.

Conflict of interest

List of publications

International peer-reviewed publications

Berghen N.*, **Dekoster K.***, Marien E., Dabin J., Hillen A., Wouters J., Deferme J., Vosselman T., Tiest E., Lox M., Vanoirbeek J., De Langhe E., Bogaerts R., Hoylaerts M., Lories R., Vande Velde G. Radiosafe micro-computed tomography for longitudinal evaluation of murine disease models. Scientific Reports 9 (2019). *equal contribution

Dekoster K., Decaesteker T., Berghen N., Van den Broucke S., Jonckheere A., Wouters J., Krouglov A., Lories R., Hoet P., Verbeken E., Vanoirbeek J., Vande Velde G. Longitudinal µCT-derived biomarkers quantify non-resolving fibrosis in a silicosis model. Scientific Reports 10 (2020).

Voordeckers K., Colding C., Grasso L., Pardo B., Hoes L., Kominek J., Gielens K., **Dekoster K.**, Gordon J., Van der Zande E., Swings T., Michiels J., Van Loo P., Nuyts S., Pasero P., Lisby M., Verstrepen K.J. Ethanol exposure increases mutation rate through error-prone polymerases. Nature Communications 11 (2020).

Tielemans B., **Dekoster K.**, Verleden E., Sawall S., Leszczyński B., Laperre K., Vanstapel A., Verschakelen J., Kachelriess M., Verbeken E., Swoger J., Vande Velde G. From Mouse to Man and Back: Closing the Correlation Gap between Imaging and Histopathology for Lung Diseases. Diagnostics 10 (2020).

Malengier-Devlies B., Decaesteker T., **Dekoster K.**, Vanstapel A., Ahmadzadeh K., Poosti F., Mitera T., Seldeslachts L., Verbeken E., Wouters C., Vande Velde G., Vanoirbeek J., Matthys P. Lung functioning and inflammation in a mouse model of systemic juvenile idiopathic arthritis. Frontiers in Immunology 12 (2021).

Jonckheere A., Seys S., Decaesteker T., **Dekoster K.**, Cremer J., Dilissen E., Schols D., Iwakura Y., Vande Velde G., Breynaert C., Schrijvers R., Steelant B., Vanoirbeek J., Ceuppens J., Dupont L., Bullens D. Innate lymphoid cells contribute to the induction of airway hyperreactivity in a murine neutrophilic asthma model. Frontiers in Immunology (2022).

Dekoster K., De Langhe E., Van den Broucke S., Hoet P., Lories R., Vanoirbeek J., Vande Velde G. The Centre of Tidal Volume, a novel µCT-derived functional lung biomarker for preclinical research. In preparation.

Abstracts presented at conferences

International conferences

Fraunhofer seminar "Models of Lung Disease" 2018, Application of *in vivo* microCT to identify novel imaging derived biomarkers in a mouse model of silica-induced pulmonary fibrosis. Poster presentation, 18-19 January 2018, Hannover, Germany.

European Molecular Imaging Meeting (EMIM) 2018, Novel microCT-derived biomarkers for longitudinal evaluation of silica-induced pulmonary fibrosis in a mouse model. Poster presentation, 20-23 March 2018, San Sebastian, Spain.

European Respiratory Society (ERS) Lung Science Conference 2019, Longitudinal in vivo micro-CT for characterization of acute exacerbations in a pulmonary fibrosis mouse model. Poster presentation, 7-10 March 2019, Estoril, Portugal.

European Respiratory Society (ERS) International Congress 2019, Longitudinal micro-CT-derived biomarkers: the new standard readouts for preclinical evaluation of pulmonary fibrosis and therapy. Poster discussion, 28 September – 2 October 2019, Madrid, Spain.

National conferences

Bruker microCT user meeting 2018, Using in vivo microCT for longitudinal evaluation of silica-induced pulmonary fibrosis in mouse lungs. Oral presentation, 16-19 April 2018, Ghent.

GSK awards in pulmonology 2018, Longitudinal characterization of silica-induced pulmonary fibrosis in mice by in vivo µCT. Oral presentation, 30 May 2018, Brussels.

BMIC meets industry event @ UCB, Longitudinal in vivo micro-CT for high-power preclinical screening of anti-fibrotic compounds in mouse model of lung fibrosis. Oral presentation, 28 November 2018, Brain-l'alleud.

Short curriculum vitae

Kaat Dekoster was born on December 7th 1994 in Leuven, Belgium. After graduating from secondary school at the Paridaensinstituut, Leuven in 2012, she started her training in Bioscience Engineering at the KU Leuven. In 2017, she graduated magna cum laude as Master of Science, Bioscience Engineering, specialized in Cell and Gene Technology. In 2017, she started her PhD at KU Leuven in the Biomedical MRI under supervision of Prof. Greetje Vande Velde and Prof. Jeroen Vanoirbeek.